STARS

University of Central Florida
STARS

Electronic Theses and Dissertations, 2020-

2020

Evaluation of Convective Heat Transfer Numerical Methods on Rough Surfaces from Additive Manufacturing

Jose Urcia
University of Central Florida

Part of the Aerodynamics and Fluid Mechanics Commons

Find similar works at: https://stars.library.ucf.edu/etd2020

University of Central Florida Libraries http://library.ucf.edu

This Masters Thesis (Open Access) is brought to you for free and open access by STARS. It has been accepted for inclusion in Electronic Theses and Dissertations, 2020- by an authorized administrator of STARS. For more information, please contact STARS@ucf.edu.

STARS Citation

Urcia, Jose, "Evaluation of Convective Heat Transfer Numerical Methods on Rough Surfaces from Additive Manufacturing" (2020). *Electronic Theses and Dissertations, 2020-*. 307.
https://stars.library.ucf.edu/etd2020/307

EVALUATION OF CONVECTIVE HEAT TRANSFER NUMERICAL METHODS ON
ROUGH SURFACES FROM ADDITIVE MANUFACTURING

by

JOSE URCIA
B.S. Aerospace Engineering University of Central Florida, 2018

A thesis submitted in partial fulfilment of the requirements
for the degree of Master of Science in Aerospace Engineering
in the Department of Mechanical and Aerospace Engineering
in the College of Engineering and Computer Science
at the University of Central Florida
Orlando, Florida

Summer Term
2020

ABSTRACT

The high versatility of additive manufacturing have led to an increase of use in a number of different fields. It has proven to be more reliable and precise than the traditional subtractive manufacturing when compared to producing complex geometrical parts. However, additive manufacturing inherently comes with flaws. Surface roughness is then one flaw that comes as a natural consequence of additive manufacturing which interferes with a smooth wall assumption such as those found in gas turbine blades. Nonetheless, under the correct conditions these roughen surfaces may improve drag and heat transfer within a turbulent regime. As such, a method capable of accurately measuring these thermo-fluid characteristics is analyzed in this report.

The Discrete Element Roughness Method (DERM) has been used to improve convective heat transfer predictions on surface roughness. This work aims to validate the core momentum and heat transfer correlation of DERM through an evaluation of Computational Fluid Dynamics (CFD)-based solution of the flow around individual roughness elements with the goal of improving the correlations. More specifically, the matrix of scenarios evaluated includes four different roughness elements at three different pressure drops and five different flow rates for case validations. Specific boundary conditions where chosen to simulate an environment of thousands of elements of which only one was to be explicitly modeled at a time. Results from these studies are to be used to validate and improve correlations used to approximate roughness in DERM. For each element, a steady and unsteady case are conducted and analyzed. The momentum and heat loss results obtained from the CFD are then compared to the DERM-based predictions from the same roughness elements in search of any discrepancies.

It is observed the momentum DERM-based correlation deviates from the CFD prediction with increasing element height as was expected. Furthermore, from the various cases it was found DERM

became a geometric dependent solution rather than flow-dependent. The DERM literature-based Reynolds number and coefficient of drag were also inspected. It was found that neither dimensionless number were able to maintain accurate results. An attempt at improving the momentum prediction by improving the Reynolds number and Coefficient of drag was made. It was found that improved correlations saw a slight decrease in error. These predictions are found to deviate up to a factor of five relative to the DERM-correlation terms depending on the roughness element being inspected.

ACKNOWLEDGMENTS

TABLE OF CONTENTS

LIST OF FIGURES

LIST OF TABLES

CHAPTER 1: INTRODUCTION

The motivation of this research was provided by the need to better understand the physics of a rapidly evolving engineering tool. With a complete understanding of surface roughness, its manipulation in current engineering problems for improvement becomes attainable. This chapter begins with an introduction to additive manufacturing and its relationship to surface roughness. This is followed by an account of past and current research of surface roughness and its connection to heat transfer and fluid mechanics within the aerospace industry and among others.

1.1 Surface Roughness

Over the past decade, the engineering industry has seen an increase in use of additive manufacturing (AM) due to its extensive usage. It has become an engineering marvel capable of highly complex applications where traditional, or also known as subtractive manufacturing, may have drawbacks or simply be impossible. It has been suggested that even though traditional manufacturing is still more cost effective, additive manufacturing is superior at its ability to handle complex designs [39].

Additive manufacturing utilization is not a perfect tool however, as some of its features come with natural defects. One of the most prominent features of AM is the unavoidable surface roughness that is naturally produced in its process of manufacturing. As it stands, plenty of techniques have been developed in order to finish off this roughness for an improvement on surface quality [27, 15]. While some of these techniques may prove to be efficient they are nevertheless expensive and time consuming due to the added steps needed, deterrents of manufacturing. Even further, finalizing surface quality of the finishing techniques requires an extensive process such as described in the

work of Razvan, Majeed and a Swedish team [32, 52, 47]. Naturally the objective of removing a blockage, or roughness, would be to improve upon the products functionality. However depending on the products purpose, roughness may become advantageous and the techniques described before would be unfavorable. Such a purpose is found where surface roughness occurs naturally such as in nature where its been found to improve its function. In regards to nature, shark scales have similar geometrical characteristics to that of roughness, and within turbulent flow it is capable of reducing drag rather than increasing it [10]. Even in terms of flight, birds use natural roughness within their wings to increase glide performance [8]. In terms of the hydro- and aerodynamic effects these rough surfaces have other dynamics are also in effect that contribute to drag reduction other than roughness itself, such as the movement of scales to manipulate the boundary layer [28, 11]. Nevertheless, having a better understanding on the coupled dynamics surface roughness has within a turbulent system would inspire improved physics models.

In light of this natural phenomenon, roughness produced from AM is still not fully understood. Studies are conducted to better comprehend the effects of different surface roughness, such as Garcia's work [13]. Furthermore according to a study conducted on the utilization of the Laser-Powered Bed Fusion (L-BPF), concluded that one AM procedure often used for metallic and alloy materials found roughness's parameters changing depending on the process in implementing the L-PBF method [12]. With surface roughness characteristics changing depending on the AM method used, it becomes taxing developing a numerical method for each individual AM technique and process. With this mind the ability to conclusively develop a method for the purpose of roughness modeling regardless of the technique used, becomes ideal.

1.2 Engineering Application

Within the aerospace industry, AM has steadily changed from being an alternative method to a more commonly used application for precision tool manufacturing. As it stands, the use of AM within the the field has increased significantly and has been incorporated through the use of various internal components [40, 26]. With its versatility and ease of use, AM is beginning to be integrated to more complex and larger designs as such cooling channels and airfoils within rocket and turbine engines [22, 20]. Given AM current applications, it becomes reasonable to pursue a complete understanding of surface roughness.

Current research of surface roughness spans a wide variety of applications. In the context of thermodynamic-fluid mechanic study, assuming the surfaces to be smooth as traditionally done will lead to unacceptable approximations for analysis methods including computational fluid dynamics (CFD). In terms of aerodynamics, roughness has shown to have great effect in its coefficients [9, 4, 3]. As an example within higher viscous fluids, the study done by Kandlikar shows what the effects of roughness does to pressure drop within a channel [24]. In the study conducted by Tummer [51], the relation between the Nusselt and Rayleigh numbers deviated within a roughness turbulent flow. MacDonald [31] also preformed a study similar to Tummer where it was found that in turbulent flows with roughness, heat transfer will never enter what is known as the ultimate regime effecting the heat transfer process. Lastly, Ortiz-Perez [38] discovered that in immersed tubes the heat transfer is consequently dependent on the size of the roughness particle so as to averagely increase heat transfer by forty percent when compared to a smooth surface reference. Furthermore, other previous studies have shown when comparing different roughness configurations to that of a smooth reference, the friction drag and heat transfer coefficients drastically change [44, 1, 20]. The main issue lies in the principle that the temperature of the surface affects the temperature of the flow, which then affects the temperature of the surface. All of which is also affected by the

3
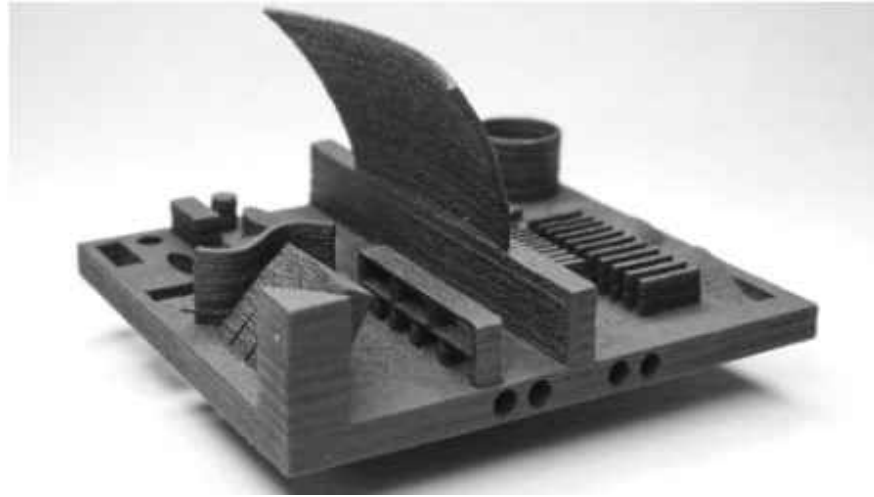
Figure 1.1: Example of Surface Roughness from Additive Manufacturing Adapted from [7]

current state of the flow (i.e laminar, transitional, turbulent) which is effected, again, by the surface. This becomes an iterative solution that requires an approach that can accurately depict the convection process involving an interaction between a rough surface and the external flow. Surface roughness itself presents issues when attempting to account for it during analysis. Roughness may consist of inconsistent sizes, shapes, and patterns proving to be extremely complex to model numerically like the one shown in Fig. 1.1. Within the context of CFD, modeling such a complicated geometry becomes highly unfeasible due to both the demand of more knowledge of the roughness characteristics and extensive increase of computational time. Often times to capture the roughness characteristics, one must scan the roughness regime such as done in Hanson [16] and Stimpson [48] which contributes to time and equipment required. Therefore, it is then ideal to model roughness with a known symmetrical three-dimensional array of roughness elements. The Discrete Element Roughness Method (DERM) is then such a method, capable of characterizing complex surface roughness into simplified elements of an array. Within the context of aerodynamics, modeling roughness has traditionally used the turbulence model [18, 17, 20] to approximate roughness with an equivalent sand-grain roughness (SGR) approach. Such an approach is a relatively easy addition

to CFD codes, and hence, has been the typical approach. By utilizing DERM in conjunction of the SGR model, it will allow us to determine the effectiveness of DERM in calculating convective heat transfer as it has been previously shown to effectively model conjugate heat transfer on large-scale roughness [18, 17, 35, 1, 20]. This large-scale roughness is the ideal condition when referring to surface roughness from additive manufacturing.

CHAPTER 2: BACKGROUND

Within the context of numerical engineering, the Discrete Element Method (DEM) was the original name for DERM due to its numerical methods at solving for small particles. DEM became the traditional name for any numerical problem involving Lagrangian particles in granular, porous, or discontinuous mediums. Hence, to avoid confusion and maintain consistency with previous work, this work refers to DEM as DERM within the context of roughness.

2.1 Discrete Element Roughness Method

The concept that drive DERM were first developed as early as 1936 by Schlichting [42]. Since, it has been applied by several investigators to the problems found in turbine blades from surface roughness [35]. Extensive work in DERM has been performed by a handful of investigators including: Lewis [29], Taylor [49, 50], McClain [36] and Aupoix [5, 6] among others as well. Aupoix [5] is responsible for deriving the DERM boundary-layer formulations from a volumetric average approach rather than a the traditional control volume engineering approach. Taylor on the other hand completed his work to include the blockage effects and other forms of drag not yet considered [50]. More recently, it has been explored for ice roughness [18, 17, 21, 16] as well as for cooling channels that are additively manufactured [20]. Surface roughness has even been explored in regimes of microfluidics such the work conducted by Jing [41], Jia [23], and Schneider [43].

DERM was designed as an alternative approach to the equivalent SGR model by considering the physical characteristics of the roughness elements and improving on the heat transfer predictions [35, 21, 29]. The principle of DERM is a decomposition of the wall friction drag and heat transfer components due to the presence of roughness and any smooth flat surface (i.e subsurface)

between these roughness elements [18, 36]. This allows for the approach, briefly mentioned above, of replacing a real complex unknown and unpredictable surface roughness with that of known discrete symmetrical elements. Thus, reducing computational time and and increasing the accuracy of the convective heat transfer results. These results are calculated through empirical correlations of DERM as functions of the known roughness element geometry and local condition of the flow. The momentum and heat transfer correlations which make up part of these empirical correlations are then in need of closer inspection for validation purposes.

Some of the underlying correlations specifically aim to provide closure for the drag coefficient, $C_d = F_D/(1/2\rho V^2 d)$, and the Reynolds number, $Re = \rho V d/\mu$. These parameters are critical to determine the momentum losses from roughness which then also effect the heat transfer effects.

2.2 Source Terms

It is important to provide an overview of DERM and how it incorporates the previously mentioned parameters. The essence of DERM involves the simplification of complex roughness geometry with discrete symmetrical elements, which is then approximated using volumetric source terms in the same region that would mimic the effects of the physical roughness element. Fig. 2.1, shows an illustration of a real complex roughness (left) being physically replaced by discrete elements.

2D Slice View of Real Roughness

Simplified Roughness Elements
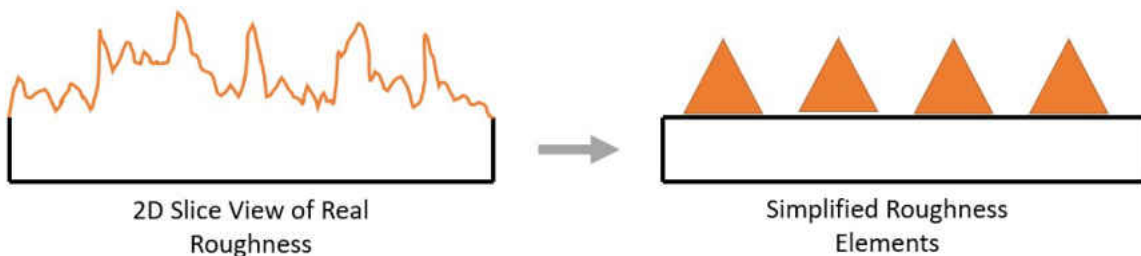
Figure 2.1: Simplification of Complex Roughness Geometry with Discrete Symmetrical Elements

From Fig. 2.1, DERM then models the surface roughness (right) using source terms in conjunction with the mass, momentum, and energy conservation equations for thermo-fluid problems and is replaced by a DERM region as shown in Fig. 2.2. With this goal in mind, DERM is capable of modeling roughness without the need to explicitly model the physical surface roughness.
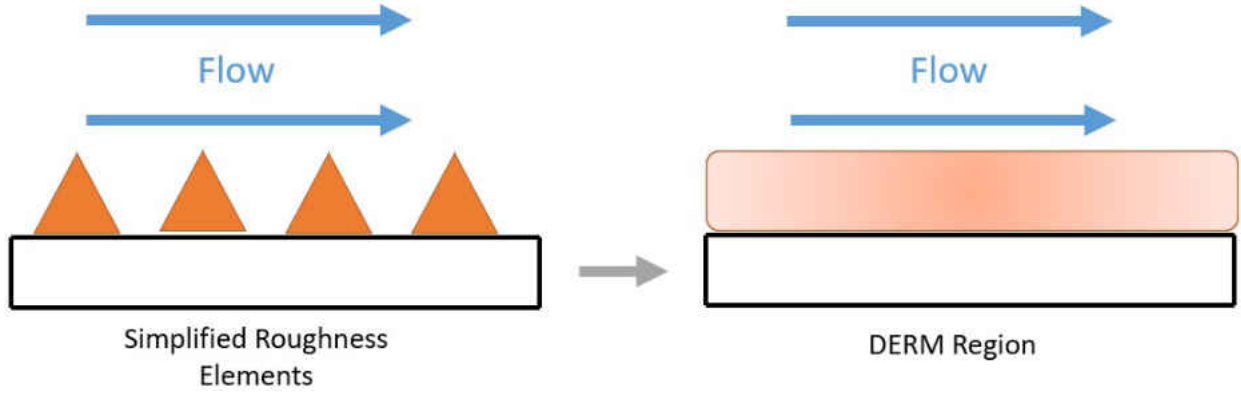
Figure 2.2: Discrete Symmetrical Elements to DERM

A complete derivation of the DERM source equations is provided in Appendix A via a volume-averaging approach. Within these source terms, the correlations (to be validated in this work) are effort terms that are foundational to DERM. These correlations used as an application of DERM, are considered to be a natural way to incorporate as many of the geometric characteristics of the real roughness as necessary to fully describe the roughness element properties from its interaction with any fluid [16]. The DERM flow equations with source terms representing roughness are presented below (in index notation) for:

Conservation of Mass:

$$\frac{\partial \rho}{\partial t} + \frac{\partial \rho u_i}{\partial x_i} = -\frac{1}{\beta}\rho u \frac{\partial \beta}{\partial x_i} \tag{2.1}$$

Conservation of Momentum:

$$
\frac{\partial(\rho u_i)}{\partial t} + \frac{\partial}{\partial x_j}(\rho u_i u_j + P\delta_{ij} + \frac{2}{3}\rho k\delta_{ij} - 2(\mu + \mu_t)\delta_{ij} + \frac{2}{3}(\mu + \mu_t)\frac{\partial u_k}{\partial x_k}\delta_{ij}) =
$$
$$
\frac{1}{\beta}f_i^p - \frac{1}{\beta}(\rho u_i u_j + P\delta_{ij} + \frac{2}{3}\rho k\delta_{ij} - 2(\mu + \mu_t)\delta_{ij} + \frac{2}{3}(\mu + \mu_t)\frac{\partial u_k}{\partial x_k}\delta_{ij})\frac{\partial\beta}{\partial x_j} \tag{2.2}
$$

Conservation of Energy:

$$
\frac{\partial \rho e_o}{\partial t} + \frac{\partial}{\partial x_j}(\rho u_j h + (\mu + \frac{\mu}{\sigma_k})\frac{\partial k}{\partial x_j} - (\frac{c_p\mu}{Pr} + \frac{\mu_t c_p}{Pr_t})\frac{\partial T}{\partial x_j} - 2u_i(\mu + \mu_t)S_{ij}
$$
$$
+ \frac{2}{3}(\mu + \mu_t)u_j\frac{\partial u_k}{\partial x_k} + \frac{2}{3}u_j\rho k) = \frac{1}{\beta}f_i^p u_i + \frac{1}{\beta}f_i^q - \frac{1}{\beta}(\rho u_j h + (\mu + \frac{\mu}{\sigma_k})\frac{\partial k}{\partial x_j} \tag{2.3}
$$
$$
- (\frac{c_p\mu}{Pr} + \frac{\mu_t c_p}{Pr_t})\frac{\partial T}{\partial x_j} - 2u_i(\mu + \mu_t)S_{ij} + \frac{2}{3}(\mu + \mu_t)u_j\frac{\partial u_k}{\partial x_k} + \frac{2}{3}u_j\rho k)\frac{\partial\beta}{\partial x_j}
$$

The left-hand side (LHS) of Eqs. (2.1-2.3) represent the standard mass, momentum, and energy laws, respectively, of which form the bases of most CFD frameworks. These equations include: spatial and temporal variables such as distance, velocity, and time; fluid variable properties being viscosity, density, and viscous stress tensor; Thermal-fluid properties such as thermal conductivity, Prandtls number, specific heat, temperature and energy. The right-hand side (RHS), however, includes the corrections that represent the source terms relevant to DERM. These corrections are made up of the previously discussed fundamental variables in addition to void fraction, drag effort term, and heat transfer effort term.
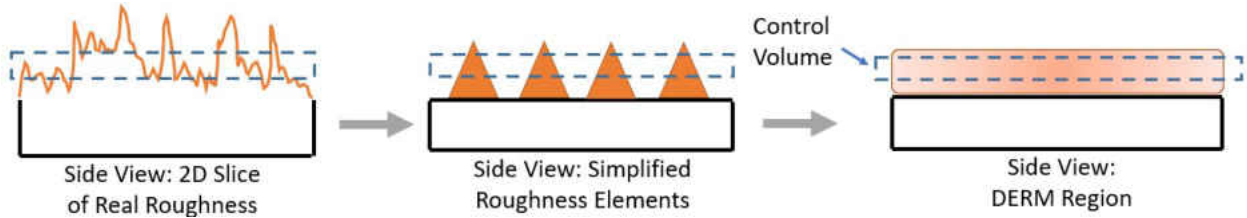
Figure 2.3: Control Volume Application of DERM Source Terms.

As a description of the application of the source terms previously described, refer to Fig. 2.3. In this figure, the dotted blue lines are a representation of one control volume being taken of the surface roughness. These control volumes are applied in intervals through out the height of the elements where DERM region (right) becomes an approximate replica of the original (left) control volumes.
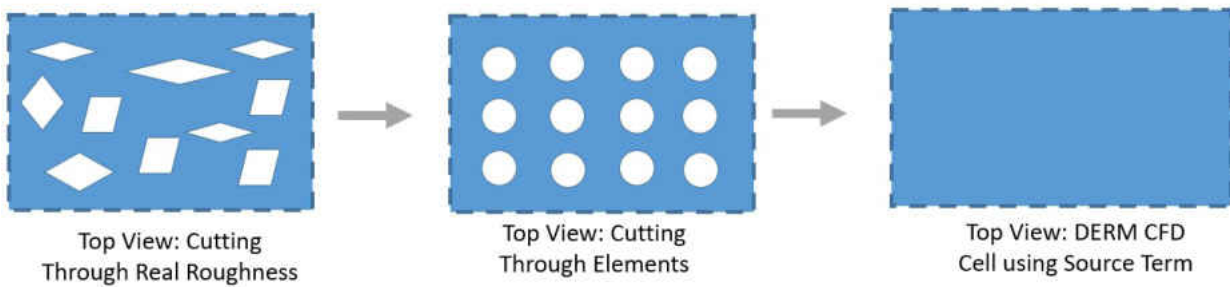
Figure 2.4: View of Control Volume From Fig. 2.3

The control volumes, which can be seen by Fig. 2.4 can be thought of an exact measurement of the roughness (left), where your Navier-Stokes equations (see by the LHS of Eqs. (2.1-2.3)) can be applied. Followed by a simplification and approximation through simplified elements (middle) where then the correction terms in the RHS of Eqs. (2.1-2.3) are applied to mimic the effects of the simplified elements but without the physical requirement of them such as in a CFD cell (right). The purpose of the simplification of the elements, can be seen by a further inspection of Eqs. (2.2-

2.3). Within these source terms which are implemented in the DERM region (right), includes effort terms f_i^p and f_i^q which are vital and need of evaluation.

In addition, it is also mentioned that Eqs. (2.1-2.3) are in non-conservative form. This is due to involving the void fraction β, in which allows for the application of a CFD solver without added steps in-between. Through this approach, these correlations can be measured away from the roughness element where β is zero, down to the sub-surface where it is at maximum. The consequences of the use of a non-conservative evaluation is not considered and beyond the scope of the current application of DERM.

2.3 Effort Terms

The "effort" terms found in the DERM conservation equations, f_i^p and f_i^q, represent the drag and convective heat transfer (CHT), respectively [18]. Consider the middle of image of Fig. 2.3, these terms are representative of a single computational cell such as the control volume, which may complicate their computations but their volumetric values may be approximated via empirical correlations given previous experimental data. These terms take a geometrical approximation approach taken from a control volume; where if the computation cells within the CFD can be considered short and wide then they may be represented by simple cylinders.
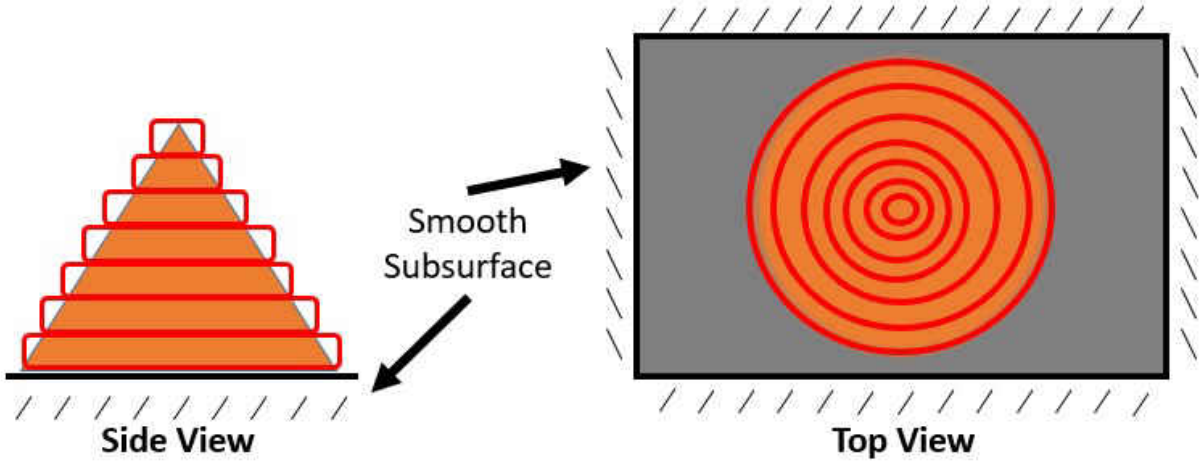
Figure 2.5: Approximation of Cone-based Roughness Element (Orange) Using Stacked Cylinders (Red)

The illustration shown by fig. 2.5 represents an example of the DERM cylindrical stacking geometric approximation within its source terms derived from multiple control volumes. It is from this illustration that it gives reason for the investigation of the correlation-effort terms. Near the subsurface DERM can approximate the cone with great accuracy, but visually this accuracy appears to decrease as it cannot maintain similar geometric features as it reaches the top of the element. From this it can then be theorize that depending on the roughness element, the inaccuracy given from the cylindrical approximation may increase.

The volumetric integral of these effort terms are then given below:

$$\iiint_V f_i^p \, dV = 2u_i \frac{\mu}{\pi a^2} \beta (1-\beta) Re_a C_d \tag{2.4}$$

$$\iiint_V f_i^q \, dV = 4 \frac{k_f}{a^2} \beta (1-\beta)(T_r - T_f) Nu_d \tag{2.5}$$

12

Where C_d is the drag coefficient and Nu_d is the Nusselt number for each element roughness. To stay consistent with previous DERM literature, the correlations for given by Eqs. 2.6 and 2.7 are to be use to solve for C_d and Nu_d of which are the most common given by McClain [36].

$$C_d = \begin{cases} (\frac{Re_a}{1000})^{-0.125} & \text{if } Re_a < 6x10^4, \\ 0.6 & \text{Otherwise.} \end{cases} \qquad (2.6)$$

$$Nu_d = \begin{cases} 1.7Re_a^{0.49}Pr^{0.4} & \text{if } Re_a < 137764, \\ 0.0605Re_a^{0.84}Pr^{0.4} & \text{Otherwise.} \end{cases} \qquad (2.7)$$

The roughness Reynolds number used is defined as a function of local roughness diameter and local flow speed, $Re_a = \frac{\rho Va}{\mu}$. In the context of DERM, variable a is the local roughness parameter and will be referred to as local a within this paper. A description on the methodology used to evaluate local a is explain in section 3.1.2.

These correlations can then be applied and validated in terms of the roughness element height through its void fraction β. The methodology behind the validation of these effort terms is explained in detailed in section 3.

2.4 Overview of Approach

In this study the f_i^p and the f_i^q terms are to be studied for validation along with the C_d (drag coefficient), Re (Reynolds number), and Nu_d (Nusslet number) given by the literature. These correlations in DERM contain a handful of assumptions of which will be accounted for.

The main assumption within DERM is that its flow must travel parallel to the subsurface and normal to the vertical axes of the element. Due to DERM being applicable within the boundary

layer, these are reasonable assumptions. This assumption does break down at stagnation points anywhere in the DERM region. Also, DERM makes the assumption of an ideal incompressible flow. This is not a consequence of utilizing DERM, rather the empirical correlations for C_d and Nu_d are only valid under low-mach number subsonic regimes; where compressibility effects may be ignored. Taking into account roughness within supersonic regimes using DERM is beyond the scope of this paper

In this approach, a sub-grid scale model of the roughness is used in order to characterize the flow and its heat transfer properties. In order to correctly scale the roughness, the only component needed is an equivalent SGR height parameter of the roughness since its shape and pattern may be simplified to a known geometry adapted from an AM technique used [18, 12].

In this paper, four separate three-dimensional geometries are used as equivalent surface roughness shape to better understand the mechanics of the flow respective to its convective heat transfer. These elements consist of known geometries such as a cone, hemisphere, concave-cone, and a partial-sphere. By defining the empirical correlations with source terms, the effort terms respective to momentum and energy will become available for validation. These effort terms can then be approximated which avoids the requirement to define a complex geometry from a real surface roughness. The geometric properties needed will be extrapolated from an experimental study additionally to being evaluated from the same study to be further use as validation of the CFD model used and avoid the need to experimentally extract the data [34]. Using STAR-CCM+ CFD as the solver, case studies of three different pressure drops in both steady and unsteady models are preformed. Furthermore, validating cases of two roughness elements will be constructed to compare to Mart's experimental data utilizing a steady state model and two unsteady state models. These cases consist of five free stream velocities for each element which can be further broken down to two categories; a drag study and heat transfer coefficient (HTC) study. Note only a steady state model is used to for the HTC validation study. The breakdown of cases can be shown in Tab. 2.1.

Table 2.1: Number of Cases Per Model

Elements	Pressure Drop	Drag Validated	HTC Validated	Total
Cone	3	5	5	13
Hemisphere	3	5	5	13
Concave	3	0	0	3
Sphere	3	0	0	3
Total	12	10	10	32

Thus, data from these twenty-four pressure drop cases, thirty velocity-drag measuring cases, and ten velocity-heat transfer measuring validated cases will be extracted from the CFD solutions and implemented to the correlations. A breakdown between roughness element to model utilized is constructed in section (3.2.4). The predictions given from the correlations will then be compared to that of its respective CFD solution for validation.

CHAPTER 3: METHODOLOGY

This chapter aims to provide a detailed explanation of the techniques used for the validation of this work. The chapter begins with a description of how this thesis came to arrive at choosing the roughness elements studied. A section entirely dedicated to the computational fluid dynamic (CFD) modeling is given to provide insight to the models chosen. Followed by a section on the grid-sizing practice used and its importance. The chapter ends with the elucidation of data extraction for implementation to the terms in question.

3.1 Roughness Elements

3.1.1 Characterization of Element Geometry

The main objective of this paper is to provide a validation study depicting of the discrepancies given from the drag (momentum) effort term. With this in mind, a roughness geometry would be needed to begin deriving the roughness parameter to solve for the SGR. Normally, obtaining the parameters required would involve optical measurements of the surface. However, to develop such a process would require extensive approaches such as solved by Hanson [20] and Adams [2]; which is beyond the scope of this paper. Therefore, the roughness height can be extrapolated from published data where the SGR has already been defined from such a process.

The surface roughness will be defined using Mart [34] data as a single cell roughness element. These single cell elements are composed of four different geometries being a cone, hemisphere, a cone with side walls concave in (referred in this paper as concave) and a partial-sphere (referred as sphere) where one-eighth of its diameter rests below the subsurface. Note the most recent work done on the DERM correlations only applied hemispheres as a roughness element [53]. The previ-

16

ous work can then considered preliminary results of this paper on the hemisphere element and this paper is then an improvement of the methodology and results of the previous work.
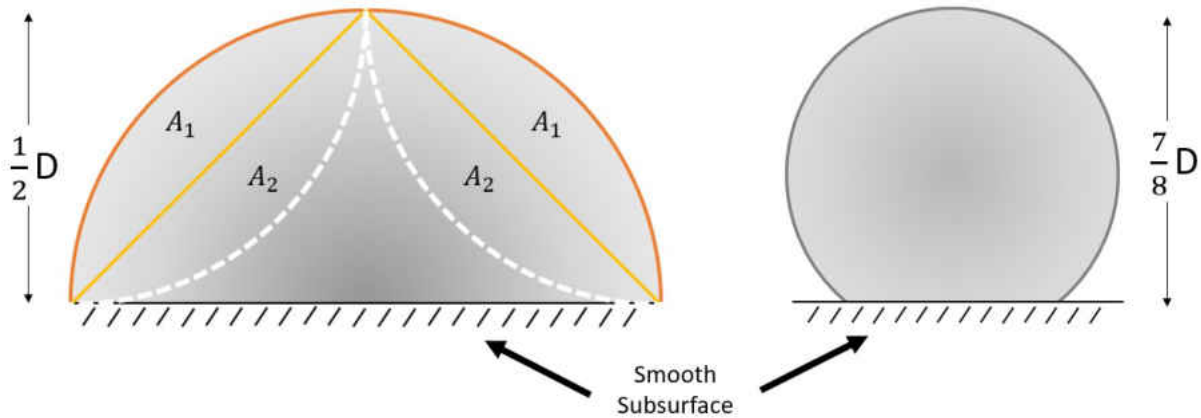
Figure 3.1: Roughness Elements: Cone, Hemisphere, Concave, and Sphere (Not Drawn to Scale)

The cone element was chosen due to one being one of the main elements in Mart's work which can be used to be validated with Mart's experimental data [34]. The hemisphere and concave elements were chosen as being derivatives of the cone, such that they are additive and subtractive areas of the cone. This idea can be seen as an illustration of the elements by Fig. 3.1; where $A_1 = A_2 = A$ so as the cone being the base element, and can become a hemisphere or concave if you were to add or subtract area 2A, respectively. This is done to add some consistency to the elements in regards to the inconsistency of real roughness. Additionally the hemisphere was also included in Mart's experimental work and thus will also be validated. The sphere element was added in as a case study of how typical real roughness may be shaped as. The unique factor of this element in comparison to that of the other elements, is of the increasing diameter followed by a decrease, an important parameter discussed in greater detail in the following subsection.

This work intends to maintain consistency between the data extracted from Mart and the previous

17

work on the hemisphere, however the importance of the element dimensions must be addressed. Due to relationship between the cone, hemisphere and concave it becomes relatively easy to define the maximum height as halve of the maximum diameter for each element such that they are all equal in height to one another. In terms of numerical modeling where the sphere element dimensions must be defined, it cannot share the same dimensions as the cone, hemisphere, nor concave elements. This is due to the geometrical law of spheres where the height is the maximum diameter and so if $\frac{7}{8}$ of the diameter where to be above the subsurface then it would be $\frac{3}{8}$ taller than the rest of elements. Vice-versa, if we were to maintain equal height to the other elements by reducing the the maximum diameter of only the sphere then modeling wise, we arrive at a disproportionate local diameter in comparison to the other elements. Given the importance of the parameter local a, further discussed below, it was decided that the maximum diameter should remain consistent with the other elements and the height to be adjusted by other means further explained in section 3.4.2.

3.1.2 Roughness Local Diameter

The local a roughness diameter is one of the key prominent parameters within this paper. Its involvement remains in the effort term, Reynolds number and coefficient of drag; two parameters found within the effort term f_i^p. Given local a changes with height, it can be interchangeable with Δa. Readjusting Eq. 2.4 to Eq. 3.1

$$\iiint_V f_i^p \, dV = Drag = 2u_i \frac{\mu}{\pi \Delta a^2} \beta (1-\beta) Re_a C_d \tag{3.1}$$

Where Δa can be considered the spacing distance within a computation cell. As such, f_i^p can be considered a second order function of Δa where it reaches its minimum at the subsurface and maximum height; this idea is to be expanded on in section. This is discussed to highlight the

18

importance of local a.

Given the local a being critical to the evaluation of the drag term, functions were developed to obtain an accurate local a. These functions and each elements respective maximum diameter are shown in Tab. 3.1.

Table 3.1: Roughness Element Local Diameter

Roughness Element	Max Height (mm)	Local Diameter a (mm)
Cone	4.765	$2(R-y)$
Hemisphere	4.765	$2\sqrt{R^2-y^2}$
Concave	4.765	$2(R-\sqrt{R^2-(R-y)^2})$
Sphere	8.339	$2\sqrt{R^2-(z-y)^2}$

The functions given in Tab. 3.1 use new variables: R, z, and y not yet defined. If we define R to be the radius of the maximum diameter given the relation introduced in section 3.1.1, then R = max height. Variable z is specific to only the sphere given its unique dimensions relative to the other elements. z is then defined as the height of the subsurface to the center point of the sphere being $z = \frac{3}{8}D$, where D is the maximum diameter. Finally, variable y is the height measured from the subsurface chosen by the author at each point where the effort term is to be evaluated.

These single cell elements are then implemented in a CFD under boundary conditions replicating that of the Mart data. Further geometric parameters that been used by previous studies utilizing DERM such as rugosity, space distancing between elements, and surface areas [18] are considered negligible in this study due the boundary conditions of the CFD. More details will be given in the

subsequent section.

3.2 Computational Fluid Dynamic Modeling

3.2.1 Description of General Solver

The present work utilized the commercial software STAR-CCM+ as the CFD software used to compute the flow around the roughness elements. STAR-CCM+ has a copious of flow solvers, temporal spacings, coupling methods and more, however only the models and methods used are described in this paper. As such for case study, two distinct flow solver models were used: the RANS and LES models both to be expanded upon in sections 3.2.2 - 3.2.3 in conjunction with the general thermo-fluid solver described below.
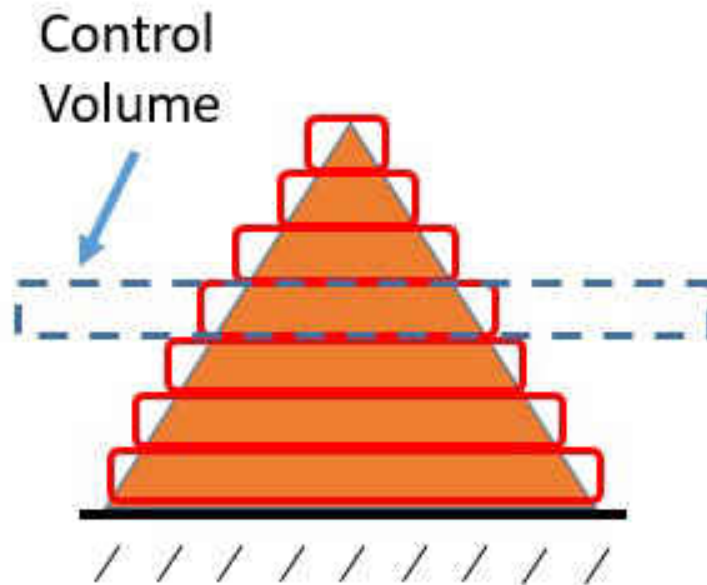
Figure 3.2: Single Cell Roughness Element

Principally, DERM is used within a CFD such as STAR-CCM+ by utilizing the DERM Eqs. 2.1-2.3 as source terms to evaluate the predictive physics of roughness. This papers focus is on the errors of these source equations which stem from the effort terms. Rather than the DERM equations previously described being input as the source terms creating what is known as the DERM Region in Fig. 2.2, the roughness is directly resolved for illustrated in Fig. 2.2 as Simplified Elements. Consider Fig. 3.2, where the cone element is illustratively broken up by DERM's method of cylindrical stacking. This paper then will then use a CFD to resolve for the cone element (orange) while DERM resolves for each cylinder (red). Hence, the core CFD model solves the governing fluid dynamics equations using numerical solutions with a segregated solver. These equations appear in the form of conservation of mass Eq. 3.2, conservation of momentum Eq. 3.3, and conservation of energy Eq. 3.5 in three-dimensional space:

$$\frac{\partial}{\partial t}(\rho) + \Delta \cdot (\rho V) = 0 \tag{3.2}$$

where ρ and V, represent density and vector velocity, respectively.

$$\frac{\partial}{\partial t}(\rho V) + \Delta \cdot (\rho V \otimes V) = -\Delta \cdot (PI) + F_b + \Delta \tau \tag{3.3}$$

If we define $\sigma = -PI + \tau$. Where the right-hand side of Eq. 3.3 becomes Eq. 3.4.

$$\frac{\partial}{\partial t}(\rho V) + \Delta \cdot (\rho V \otimes V) = \Delta \cdot \sigma + F_b \tag{3.4}$$

Then in consideration of the conservation of angular momentum such as in resolving for eddies,

$$\sigma = \sigma^T.$$

$$\frac{\partial}{\partial t}(\rho E) + \Delta \cdot (\rho E V) = F_b \cdot V + \Delta \cdot (V \cdot \sigma) - \Delta \cdot q + S_E \tag{3.5}$$

Where E is total energy, q is heat flux, and S_E is an energy source per unit volume.

The viscous-stress tensor is notated by τ given by:

$$\tau = 2\mu D - \frac{2}{3}\mu(\Delta \cdot V)I \tag{3.6}$$

Where D is known as the rate of deformation tensor shown by Eq. 3.7.

$$D = \frac{1}{2}(\Delta V + (\Delta V)^T) \tag{3.7}$$

The viscous-stress tensor in terms of DERM given a parrallel flow assumption can be expressed as:

$$\tau_{ij} = \alpha_q[\mu_m(\frac{\partial V_i}{\partial x_j} + \frac{\partial V_j}{\partial x_i}) + (\lambda_q - \frac{2}{3}\mu_m)\frac{\partial V_i}{\partial x_i}\delta_{ij}] \tag{3.8}$$

where μ_m is the modeled viscosity. The modeled viscosity is represented as

$$\mu_m = \mu_{lam} + \mu_{turb} \tag{3.9}$$

Here, μ_{lam} is the laminar fluid viscosity and μ_{turb} is the turbulent viscosity, which is a modeled "eddy viscosity" that approximates sub-grid-scale, turbulent fluctuations further elaborated in sec-

tion 3.2.2.

$$P = \frac{\rho}{RT} \tag{3.10}$$

The ideal gas law (shown in Eq. 3.10) was chosen as the relation between energy and momentum laws, where $R = \frac{R_u}{M}$ and M is the molecular weight of the gas and R_u being the universal gas constant. Due to the Mach number of the flow not surpassing 0.3 in either flow solver model, then compressibility effects can be neglected. While STAR-CCM+ has the capability of solving for more complex real gas models such as Peng-Robinson, Van der Waals, or Redlich-Kwong, these models are used under particular conditions which are not explored in this paper.

3.2.2 Reynolds-Averaged Navier-Stokes (RANS) Model

As the steady-state case the author selected the Reynolds-Averaged Navier Stokes or RANS model as the flow solver. This is due to the large number of turbulence models made available with great results. As such in order to obtain the RANS equations of state each solution variable is notated as ϕ, being Navier-Stokes Eq. 3.3 which is decomposed into is averaged value $\overline{\phi}$ and a fluctuating component ϕ':

$$\phi = \overline{\phi} + \phi' \tag{3.11}$$

From these solution variables we then arrive at Navier-Stokes in terms of mean quantities.

$$\frac{\partial}{\partial t}(\rho\overline{V}) + \Delta \cdot (\rho\overline{V} \otimes \overline{V}) = -\Delta \cdot (\overline{PI}) + F_b + \Delta(\overline{\tau} + \tau_{RANS}) \tag{3.12}$$

$$\frac{\partial}{\partial t}(\rho\overline{E}) + \Delta \cdot (\rho\overline{EV}) = F_b \cdot \overline{V} - \Delta \cdot \overline{PV} - \Delta \cdot \overline{q} + \Delta(\overline{\tau} + \tau_{RANS})\overline{V} \tag{3.13}$$

These new equations are practically the same with respect to the Navier-Stokes with the exception of the added term τ_{RANS}. Then the new term is define as:

$$\tau_{RANS} = -\rho \begin{bmatrix} \overline{u'u'} & \overline{u'v'} & \overline{u'w'} \\ \overline{u'v'} & \overline{v'v'} & \overline{v'u'} \\ \overline{w'u'} & \overline{v'w'} & \overline{w'w'} \end{bmatrix} + \frac{2}{3}\rho kI \tag{3.14}$$

Where k is the turbulent kinetic energy. In this model form, the RANS viscous-stress tensor show by Eq. 3.14 is not yet able to be solved. STAR-CCM+ then allows different approaches to provide closer to the governing RANS equations above. Given the problem attempting to be model through Eq. 3.14, the eddy-viscosity model makes it possible to model a stress tensor with mean quantities.The construction of a turbulent eddy viscosity μ_t is the key relation to solve Eq. 3.14. So then the viscous-stress tensor can also be related through Eq. 3.15

$$\tau_{RANS} = 2\mu_t S - \frac{2}{3}(\mu_t \Delta \cdot \overline{V})I \tag{3.15}$$

where S is the mean strain rate tensor given by:

$$S = \frac{1}{2}(\Delta \overline{V} + \Delta \overline{V}^T) \tag{3.16}$$

In order to close of the energy relation which resolves for the heat conjugation the mean heat flux $\overline{q}$ must be defined; as it controls the RANS turbulent heat transfer preformed briefly in this work.

The mean heat flux is assumed to be proportional to the turbulent eddy viscosity as:

$$\overline{q} = -(k + \frac{\mu_t C_p}{Pr_t})\Delta \overline{T} \tag{3.17}$$

Where μ_t is the turbulent eddy viscosity. Eq. 3.17 has been proven to fail when the buoyancy forces are dominant such as near wall locations. This approximation is replaced by model Eq. 3.18 in such cases.

$$\overline{q} = -k\Delta \overline{T} - \rho C_p \overline{v\theta} \tag{3.18}$$

The turbulent heat flux $\overline{v\theta}$ can be algebraically defined as:

$$\overline{v\theta} = -C_{tu_0}\frac{k}{\varepsilon}(C_{tu_1}R\Delta\overline{T} + C_{tu2}\Delta\overline{v}\cdot\overline{v\theta} + C_{tu_3}\beta\overline{\theta^2}g) + C_{tu_4}A\cdot\overline{v\theta} \tag{3.19}$$

The unknown variables $C_{tu_0}, C_{tu_1}, C_{tu_2}, C_{tu_3}, C_{tu_4}$ are model coefficients are system dependent. The temperature variance $\overline{\theta^2}$ is computed solving an additional transport equation by Eq. 3.20

$$\frac{\partial}{\partial t}(\rho\overline{\theta^2}) + \Delta\cdot(\rho\overline{\theta^2}\overline{v}) = \Delta\cdot[(\mu + \frac{\mu_t}{\sigma_{\theta^2}})\Delta\overline{\theta^2}] + G_\theta - \rho\varepsilon_\theta \tag{3.20}$$

The model then will be subjected to a turbulence model for consistency as previous works have implemented a turbulence model [18, 17, 44, 34, 21, 53]. The governing equations of RANS (Eq. 3.12-3.14) along with the eddy viscosity model (Eq. 3.15), implement the turbulence model Spalart Allmaras [45]. Note the relations given above may be used for both steady and unsteady RANS models. In either case, each solution would be averaged however in the steady case the time

component would cancel out.

3.2.3 Eddy-Resolving Simulations (LES)

Large Eddy Simulation or LES is a transient-exclusive method in which the large length-scales of turbulence are directly solved for within the domain. As it stands, there has yet to be a study of the momentum term with an unsteady state model. Due to the turbulent flow and the expected eddies to be formed, a Large Eddy Simulation (LES) model deems to be the more appropriate model for complex geometries and conjugate heat transfer [37, 30]. Opposite to RANS where an average approach is taken, LES is solved for by the solution variable σ imposed being spatial filtered. Implementing a decomposed solution variable to the Navier-Stokes equations, we arrive at an identical form of the RANS conservation equations (Eq. 3.12-3.13). However, the stress tensor given by τ_{RANS} becomes τ_{SGS} where $\tilde{V}$ is the filtered velocity.

$$\tau_{SGS} = 2\mu_t S - \frac{2}{3}(\mu_t \Delta \cdot \tilde{V})I \qquad (3.21)$$

Although an LES model is known for its increased computational time, it is usually used for models aiming to identify high complexity turbulence structure or where RANS models do not accurately capture turbulent flow. Therefore an approach capable of using both models becomes the best fit for both computationally efficient and accuracy. A model competent of such a feat is the Detached Eddy Simulation (DES) [46]. The DES model is capable of switching between the RANS and LES models depending on the flow on region. It is setup such that if the region contains irrotational flow then a base RANS model is used. However if the grid-size within the area is refine enough, then the LES numerics would take over. The method of which the DES model defines a refined enough grid is through the measurement of a length scale, depended even further on turbulent model.

As done for the steady-state model in section 3.2.2, the Spalart-Allmaras will also be the turbulence model implemented along with LES. Solved for naturally by STAR-CCM+ within Spalart-Allmars modeling, the following transitional function solves for the turbulent length scale.

$$l_{lengthscale} = \frac{1}{2}(1 - f_{v2})\sqrt{\tau \frac{\mu_t}{\rho C_\mu}} \tag{3.22}$$

With the introduction of time, unlike the previous RANS model, a turbulent time scale t is also accounted for by:

$$t_{timescale} = (1 - f_{v2})min(\frac{2}{\tilde{S}}, \frac{\rho k d^2}{\mu_t}) \tag{3.23}$$

Where f_{v2} is a damping function model variant native to Spalart-Allmars. Here f_{v2} may be defined as

$$1 - \frac{\chi}{1 + \chi f_{v1}} \tag{3.24}$$

Where $\chi = \frac{\tilde{V}}{V}r$ and f_{v1} is also another model variant seen in Eq. 3.25.

$$\frac{\chi^3}{\chi^3 + C_{v1}^3} \tag{3.25}$$

Therefore, an LES model would be used only where using a RANS model would not be favorable proving DES to be the best fit. Note, throughout this paper this method is referred to LES because its LES turbulent modeling that introduces the difference between DES and RANS. Additionally, an important note to further distinct RANS, LES, and the hybrid RANS/LES (DES) is that within the boundary layer regardless of mesh or lengthscale the RANS model is normally used for the hybrid (DES). This model also offers a turbulent heat transfer relations, however this study does not conduct a heat transfer study beyond a steady-state RANS.

3.2.4 Boundary Conditions

In conjunction with the modeling techniques described earlier, the boundary conditions prescribed in STAR-CCM+ is another key aspect to running a functioning model. Similarly to the experiments ran by Mart where arrays of roughness elements were constructed to reach a developed flow, this paper attempts the same approach through a CFD.

The typical approach in a CFD to replicate experimental data, is to replicate the the experiment itself by constructing it via a CAD modeler and adapting it to the CFD similar to Hanson's work [18]. Constructing a CAD model of different roughness elements like the ones chosen for this study is trivial and can be done so with ease. However, the advantages of solving for the flow computationally allows us to create a near infinite amount of arrays or a number proportional to Marts experiment, to reach a fully-developed flow without worrying about the physical requirements. In either case, it becomes computationally expensive giving the mesh requirements in order to run the physics model (section 3.2.2-3.2.3) for an extensive amount of roughness elements.

As such, utilizing STAR-CCM+ fully-developed interface condition between the inlet and outlet of the domain becomes ideal. Instead of explicitly modeling numerous elements, the fully-developed condition allows for the solution of a single element as if it were within an array similar to Mart's [34]. This boundary condition only allows for the construction of a single array. In order to construct a model following Mart's experimental set-up, a symmetry plane with a periodic boundary condition is constructed on the side walls. Fig 3.3 illustrates the idea described above.
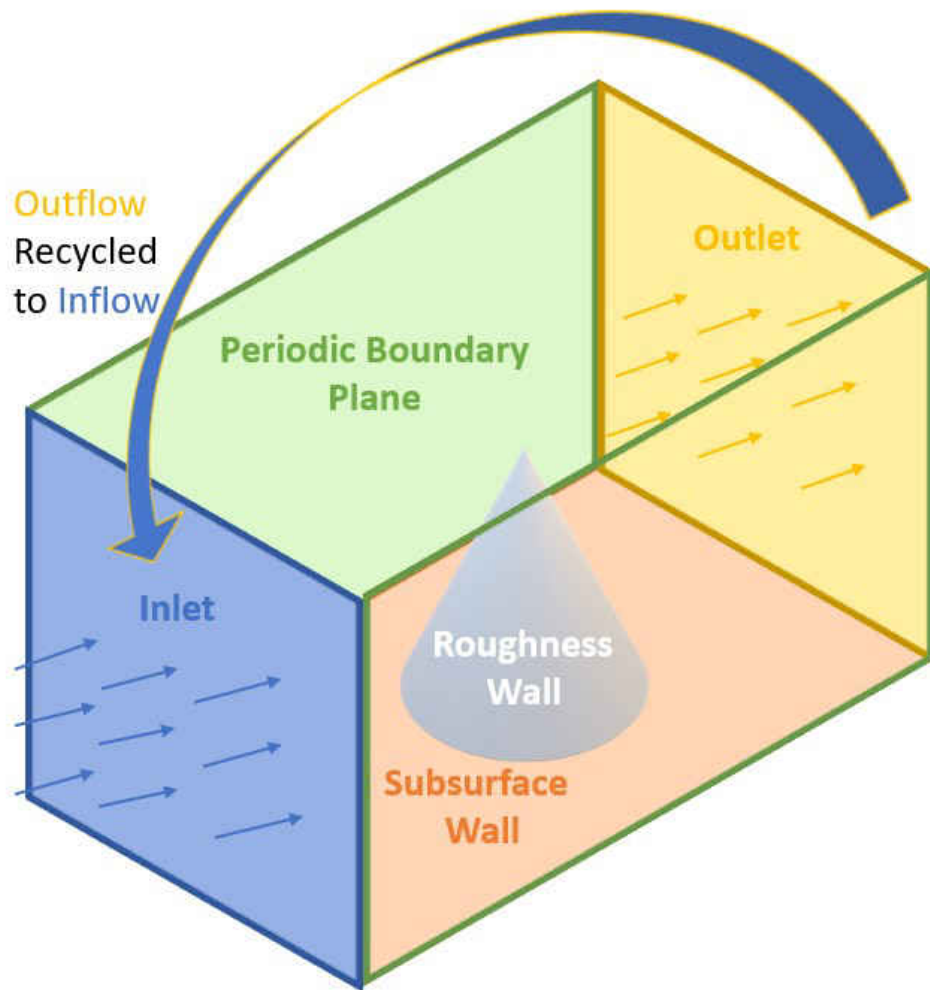
Figure 3.3: Boundary Condition for Single Cell Roughness

In the Fig. 3.3, the box can be considered the domain. Where the blue and yellow planes represent the inlet and outlet boundary conditions, respectively. STAR-CCM+ fully-developed interface conditions is then implemented by creating an interface model within the model region between the inlet and outlet conditions. This new interface then allows for a recycled flow between the boundaries meaning, flow from the outlet is then reinserted into the inlet and done so iteratively until a fully-developed flow is met (flow profiles no longer change). This condition is met by prescribing

the pressure drop allowed between the planes, permitting for different cases to be studied. Similarly the green planes, adjacent to the inlet and outlet boundaries, represent the symmetry planes with a periodic boundary conditions. These symmetry planes then mimic the effects of the flow within the domain (the box) as if there were an exact replica of this box (domain) conjoined to the symmetry plane. Note the fully-developed conditions allows the use of mass flow as an alternative to a pressure drop condition. The mass flow condition is used to specify the free-stream velocity for the validation cases. This difference of conditions in a fully-developed condition is briefly analyzed when comparing the twenty-four cases (pressure drop conditioned) to the ten velocity-drag measuring cases experimentally validated (mass flow conditioned) but is not the main aspect of this paper.
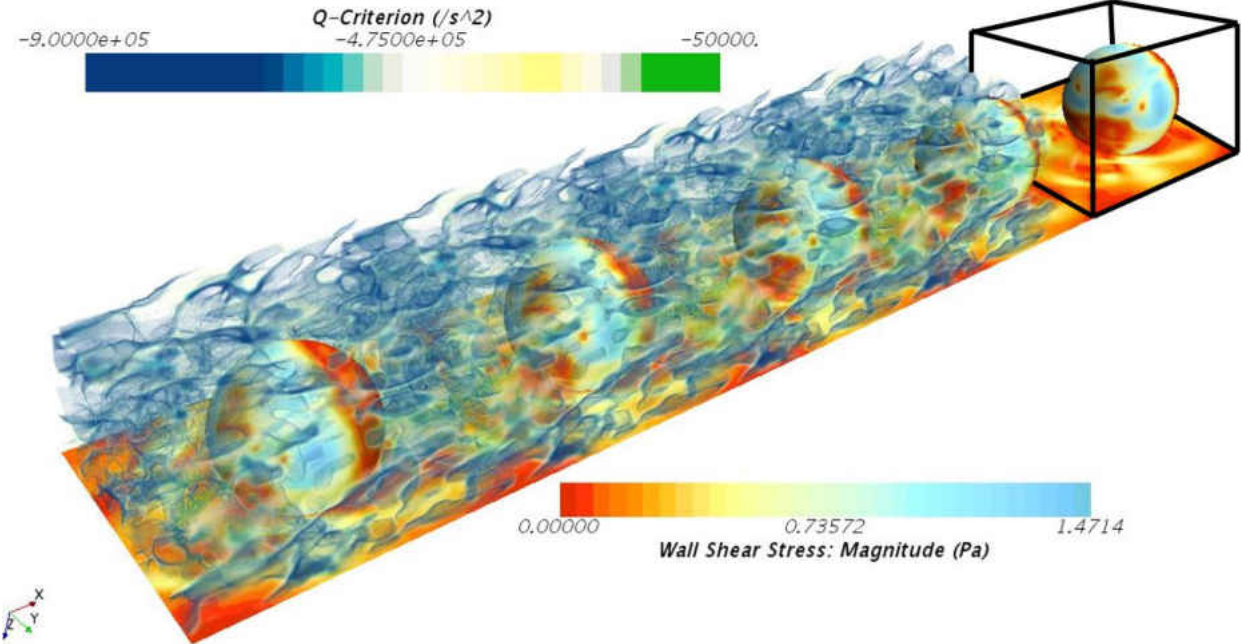

Figure 3.4: Fully-Developed Interface Condition

Finally, in order for certain parameters such as rugosity, space distancing between elements, and surface areas to be considered negligible, the model had to implement the coupled boundary condi-

tions that will allow for such an assumption. A fully developed flow with periodic boundary conditions allow for the model to be in a condition where its presumed to be modeling within thousands of other elements, without explicitly modeling other elements as described earlier. Fig. 3.4 shows an illustration of what was previously described for visualization of the CFD-solved turbulence with the interface and boundary conditions. The element within the black outlined is the single and only element prescribed to the boundary conditions shown in Fig 3.3 and explicitly solved for.

In terms of the conjugate heat transfer study also preformed, a fixed temperature was prescribed at the interface between the fluid and solid boundary domains. This would essentially keep the roughness element (solid domain) at a single constant temperature while solving for the fluid temperature and thermal boundary layer. These heat transfer boundary conditions are in accordance to Mart's experimental set up. The CFD would then solve for the heat transfer coefficient (HTC) for comparison to the experimental values found by Mart's.

Table 3.2: STAR-CCM+ Modeling

Case Type	Steady-RANS	Unsteady-RANS	Unsteady-LES
Pressure Drop	Yes	No	Yes
Drag Validated	Yes	Yes	Yes
HTC Validated	Yes	No	No

Within STAR-CCM+ this box is constructed via the CAD modeler, imposed the physics models described in sections (3.2.1-3.2.3) and outline in Tab. 3.2, and prescribed the boundary conditions followed by a mesh development.

3.3 Mesh Techniques

3.3.1 Mesh Models

While the physics and boundary conditions are what defines this study of roughness elements, the mesh techniques used determines the accuracy and convergence of the solution found from the model described above. Gives reason to leave a description of the mesh modeling used as its own individual section. The following is a description of the trimmer and polyhedral mesh techniques explored with reasoning for their respective application.

Overall the each mesh technique utilized a base cell mesh size of $1e^{-3}m$ throughout the whole domain. With further refinement by a specification of cell size within a certain volume, this volume would consist of much more densely packed cells and would be within the areas of interest where the flow matters most. This is found immediately above the max height of the element, streamwise and spanwise of the domain.

The trimmer mesh was first chosen due to its simplicity and capability of handling a multitude of scenarios. However, this mesh was especially complicated at capturing the corners and edges of the cone and concave elements. This is due to the trimmer mesh nature of being a tetrahedral (box-like shape) being less capable to completely define curve features. A solution provided for this dilemma was implementing a further refinement of a more specific volume around the tip, as displayed by Fig 3.5 where if small enough, a trimmer can capture edges with accuracy.

The polyhedral mesh was considered for use as it was the best-known practice for conjugate heat transfer. In comparison to the trimmer mesh, it was superior at defining the sharp corners and edges from the cone and concave elements without the need to create another volumetric mesh for further refinement. From this stand alone point, the polyhedral mesh deemed to be the best choice.

(a) CONCAVE ELEMENT VIEW OF TIP
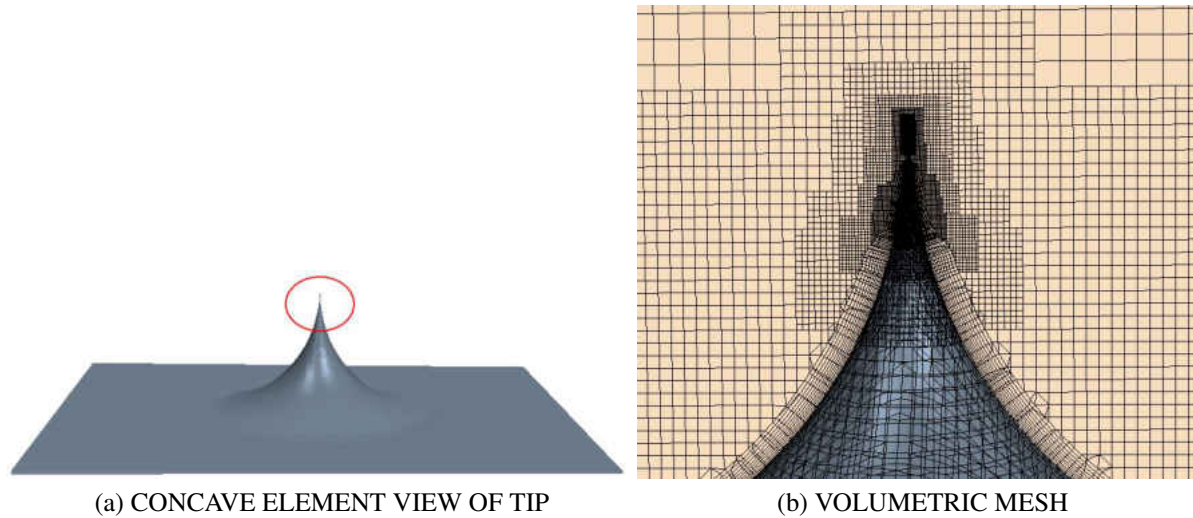
(b) VOLUMETRIC MESH

Figure 3.5: Close-up View of Tip Refinement

Upon refining the specified volume mesh to $1e^{-4}$ as part of a mesh convergence study, it was found that both the polyhedral and the trimmer mesh needed equally mesh refinement volumes in order to reach a converging solution. Upon which the trimmer mesh would be able to capture the problematic areas that could not before, essentially turning the additional refinement (displayed earlier by Fig.3.5) as redundant and obsolete. As such was the circumstance, it was taken into consideration that the trimmer mesh technique required less computational memory for the same amount of cells to that of polyhedral; per 1 million cells 1 GB of memory is required for a polyhedral mesh as opposed to a trimmer only requiring half of that amount [14]. Furthermore, a study preformed by Karakas [25] concluded a trimmer based mesh would give similar results to an aerodynamic problem as that of a polyhedral mesh.

This study has focus on experimental validated computations as well as other cases constructed. As an emphasis in studying the momentum aspect of DERM was given to twenty-four cases, it was not deemed necessary to increase computational time for negligible differences in results thus reducing computational time where possible. In terms of the other ten cases being used as validation towards

33

the model, the polyhedral mesh was used. This was due to the inclusion of a heat conjugate study not found in the other twenty-four cases. The difference in results in the momentum equations between the different mesh techniques are considered negligible. Utilizing a trimmer with the addition of a solid domain would increase the mesh cell count beyond the polyhedral to the point where the benefits no longer exist. Therefore a trimmer is beneficial for a momentum only study, however with an addition of energy the polyhedral mesh is superior. An extended explanation along with a full description of the mesh convergence study is given by section (3.5.1). The same mesh size was used as described above with further refinement of the prism-layer mesh which is expanded on in section (3.3.2).

3.3.2 Wall Y^+

The Wall Y^+ has become the standard of evaluating the mesh techniques used in its capability to capture the boundary layer, heat transfer, and other near-wall dynamics. The correct usage of the wall Y+ is depended on viscous forces and mesh at the near wall. Generally Y^+ can be calculated through Eq. 3.26 however its value should generally be kept at $Y^+ < 1$ for an accurate capture of the viscous sublayer and at $Y^+ < 0.1$ for heat transfer development [33].

$$Y^+ = \frac{y \rho u_*}{\mu} \tag{3.26}$$

As such, the implementation of a prism-layer technique is to ensure development of a low wall Y^+ value. Its values are as follows:

The momentum domain which modeled the twenty-four cases utilized a prism-layer thickness of 0.08 mm with 13 prism-layers in total and a stretching factor of 1.3. This allowed for wall Y^+ value along the streamwise direction of below 1. This can be seen through a compilation of data

34

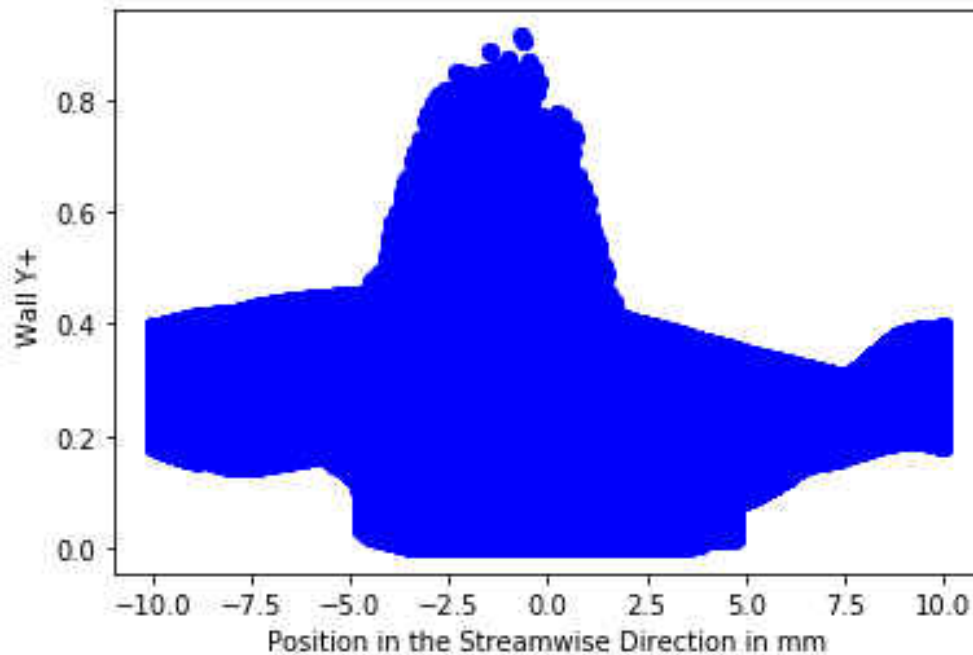points from each roughness element by Fig. 3.6 represented below.

Figure 3.6: Wall Y^+ in the Streamwise Direction of Momentum Study Cases.

For the remaining ten cases which consist of the hemisphere and cone elements used for model validation, a more refine near-wall mesh was used. The prism-layers was increased to 18 and stretching factor reduced to 1.2. This refinement was due to the inclusion of a heat transfer model. As before Fig. 3.7 represents a compilation of all elements within this study, in this case being the hemisphere and cone elements. It is important to note the difference in Wall Y^+ values between the twenty-four cases and the experimentally validated cases in which both resolve for drag. Prior to conducting the HTC cases with the Wall Y^+ as shown in Fig. 3.7, a separate simulation was conducted resolving for only momentum leaving out energy with a Wall Y^+ similar to the ones shown in Fig. 3.6. The difference in drag computations between the two domains were negligible, but ultimately the data was extracted and presented is from the refined Wall Y^+.
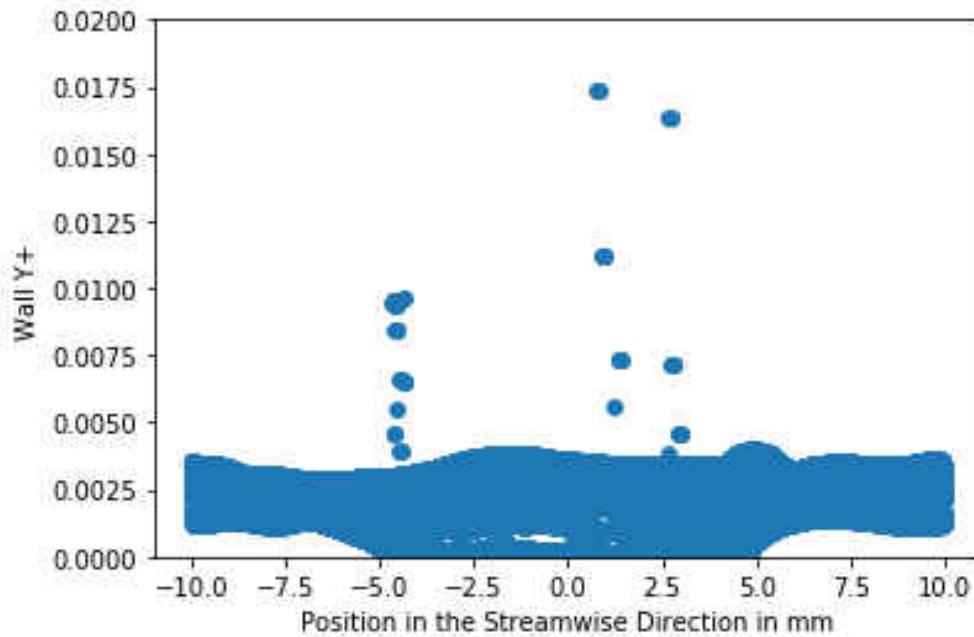
35

Figure 3.7: Wall Y^{+} in the Streamwise Direction of Validation Study Cases.

3.4 Evaluation of Terms

In this thesis, two different values are being resolved for and compared. One value being the direct solution provided by the CFD and the other being evaluated by the DERM effort-terms. Four different roughness elements being evaluated for each respective model at three pressure drop cases and the five free-stream velocity cases which measure and validate drag and heat transfer experimental data. For each of these cases the CFD and DERM are evaluated at forty-eight different elevations beginning from the subsurface up to maximum height of the elements. At each of those heights data is extracted and studied. While each case outputs a different value, its significance and necessity are to show if there is a trend to the divergence of the correlations compared to the CFD based on height. The difference in values between the RANS and LES models will also be analyzed similar to that of work done by Hanson [19, 16]. From the models built, the physics

described in sections (3.2.1-3.2.3) would be solved for and output for retrieval. However, while the information exists within the CFD, it is not necessarily a straight forward simplified command in order to retrieve it, therefore the following subsections described the methods at extracting the data required.

3.4.1 Direct CFD Term Evaluation

In all cases and models previously described, the CFD computed would natively solve for drag and heat transfer for comparison to the DERM effort-terms.

In order to retrieve the CFD prediction of drag, two one-dimensional line probes are incorporated within the CFD to extract the total pressure values. As the domain consists of a fully-developed condition, the accuracy of the probes will change depending on its location. Initially it was assumed the best placement would be the inlet and outlet boundary conditions. However because of the interface between the inlet and outlet, illustrated in Fig. 3.3, the total pressure at the outlet would technically be equivalent to the total pressure at the inlet. Due to this when the values were extracted at this position the difference would be less than 1×10^{-5} or what can constitute as a residual. As that was the case it was realized the best values would then appeared immediately in front and behind the roughness element as the inlet total pressure and outlet total pressure respectively. These probes were placed at forty-eight different heights at increments of Δy as show by Fig. 3.8, and the pressure values would be extracted and exported to an Excel file. Keep in mind in the figure below only six line probes are shown as demonstration, ninety-six line probes were used in total.
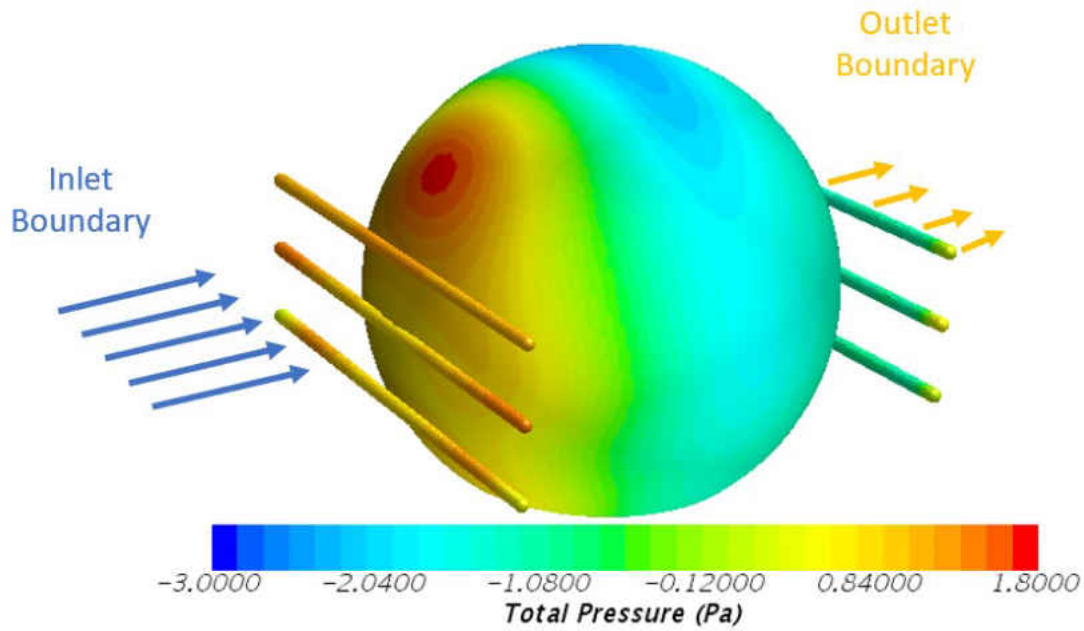
Figure 3.8: Line Probe Extraction

$$Drag_{cfd}(y) = Drag_{in}(y) - Drag_{out}(y) \qquad (3.27)$$

These extracted values would give the total pressure at a different placements, spanwise of the domain and perpendicular to the define height value y (refer back to section 3.1.2). With the use of Eq. 3.27, where $Drag_{in}$ and $Drag_{out}$ are total pressure at the inlet and total pressure at the outlet respectively, we are able to obtain the drag at each height y. However, due to the line probes extracting values at different location along a single line and not a single scalar value to be easily computed via Eq. 3.27 another method is needed to evaluate the probes. These probes would then be solved by a line integral method at varying heights equal to that of the velocity profile two-dimensional plane, explained further in the following section. Given the data consists of pressure values at their respective x-y-z coordinates, a typical line integral of a curve approach would not

38

be suited. Therefore the use of a summation of points as displayed by Eq. 3.28 is preferred.

$$\int_c f(x,y)ds = \lim_{n\to\infty} \sum_{i=1}^{n} f(x_i^*, y_i^*)\Delta s_i \qquad (3.28)$$

Here $f(x_i^*, y_i^*)$ is the pressure value at the x and y coordinates, and Δs_i is the distance between those coordinates. In the context of this work, the line probe extracts values such as P(x,y) where P function is pressure and $P(x,y) = f(x_i^*, y_i^*)$. So as a result, upon implementing the Eq. 3.28 on the data extracted at inlet and out boundaries for each height y, then we are able to use Eq. 3.27.

Contrary to the drag method previously described, the extraction for the convective heat transfer resolved CFD was not as complex. In the context of a CFD, each individual cell would inherently retain a different value of its adjacent value at the surface of the roughness element. DERM resolves for the total convective heat transfer of the approximated cylindrical cell as single value. In comparison to its CFD directly evaluated element, this same area the cylinder would fill, would contain millions if not thousands of mesh cells depending on the mesh size. As such was the case in order to effectively compare the values, a summation of all cells heat transfer resolved values was conducted at each height y. The data of these cells were extracted through a two-dimensional ring-like probe.
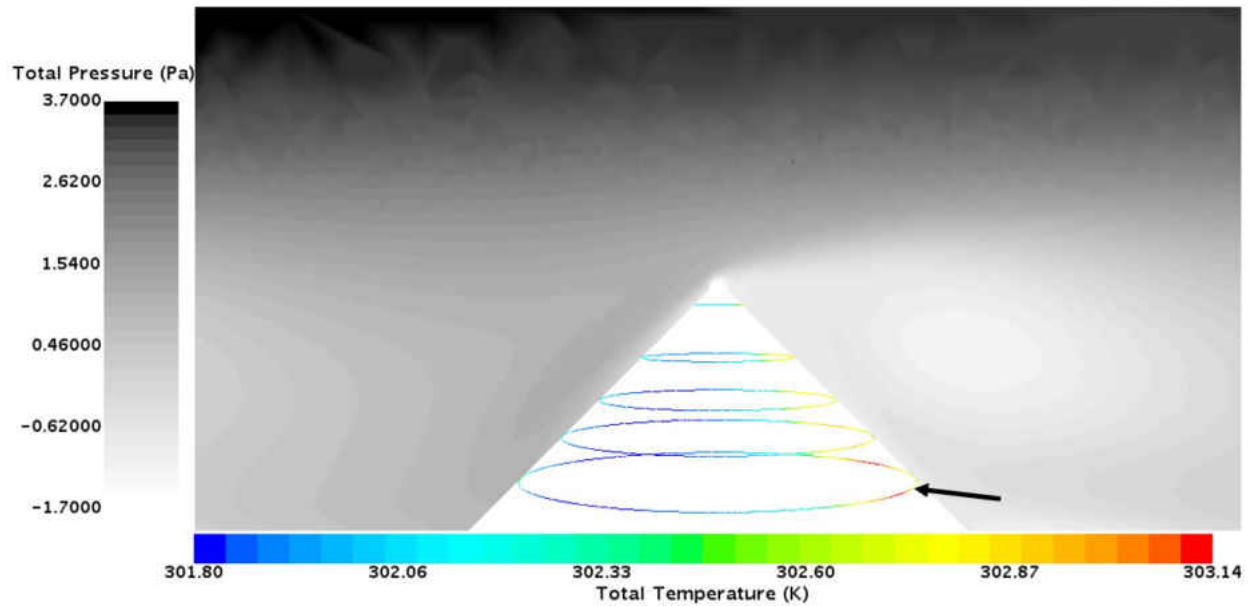
Figure 3.9: Ring-Probe Temperature Extraction

Fig. 3.9 illustrates the idea previously described as the ring-like probe(black arrow). These ring probes were also taken at forty-eight different heights equivalent to those take measuring the total pressure.

While not needed to resolve for the CFD predicted drag, the void fraction β is resolved via the explicit CAD model set up within the CFD. The void fraction is a function of two major components, the area of the plate ($Area_p$) at which is taken at every height y where the line probes would be located at, and the two-dimensional area of the roughness element $Area_{element}$ calculated via the local diameter (Tab. 3.1). Furthermore at these exact same heights where the plates are located, a surface average of the velocity profile that exist within this two-dimensional plane are taken. More on these planes to be elaborated on the following section.

3.4.2 Effort-Terms

Similarly as before, the extraction of data is needed to solve for the drag and heat transfer DERM resolved terms, f_i^p and f_i^q respectively.

As a brief recap, DERM is comprised of three different conservation equations see by Eqs. (2.1-2.3). The DERM conservation of momentum and energy are provided by Eqs. (2.2-2.3), consisting of the Navier-Stokes equations (solved natively by STAR-CCM+) along with a correction source term. These source terms then are composed of effort terms f_i^p and f_i^q, known as the drag given by Eq. 2.4 and convective heat transfer give by Eq. 2.5. In the context of this study the drag term can then be adapted to Eq. 3.1. Where Δa can be considered the local a at each height of it is being evaluated. A few things must be considered before Eq. 3.1 can be solved for.

For instance, Eq. 3.1 consists of a triple integral which is an approximation by an addition of all the local diameters. Preforming a dimensional analysis of the term we arrive at:

$$Drag_{DERM} = \frac{Kg}{s^2 m^2} \tag{3.29}$$

From the previous section 3.4.1, the data extracted was in terms on total pressure loss which is another way of computing drag. The pressure defined by Eq. 3.27 has the follow dimensions:

$$Drag_{cfd} = \frac{Kg}{s^2 m} \tag{3.30}$$

The reason for this dimension difference is due to the fact that Eq. 3.1 takes into account the drag of the total element with a two-dimensional assumption. In the methodology behind the pressure CFD extraction a one-dimensional line probe approach was taken. Therefore we must add a length

scale parameter to take into consideration this difference in dimensional approach, Δy based of the height(m) in which we are increasing from the base giving:

$$\iiint_V f_i^p \, dV = Drag_{DERM}(\Delta y) = 2u_i \frac{\mu}{\pi \Delta a^2} \beta(y)(1 - \beta(y)) Re_a C_d \Delta y \tag{3.31}$$

From this point we have define two principle parameters for the DERM drag term, local diameter a and the added length scale Δy. The last major component to evaluate the DERM term needed is the velocity streamwise across the domain normal to the inlet and outlet boundaries, u_i. Note that Reynolds number Re_a is a function of said velocity, C_d is a function of Reynolds number, and void fraction β (Eq. 3.32) is a function of local a which is defined by Tab. 3.1.

$$\beta = \frac{Area_P - Area_{element}}{Area_P} \tag{3.32}$$

This velocity u_i is extracted from the CFD via a probe. The domain is probed by a two-dimensional plane that encompass the roughness element at varying heights measured from the bottom of the element (i.e the subsurface) as shown in Fig. 3.10. These surfaces are then able to extract the velocity profiles and convert these velocities to surface averages, which can then be implemented to the correlation (drag term). Note this figure does not represent all the heights at which the CFD is probed, rather it is a representative sample.
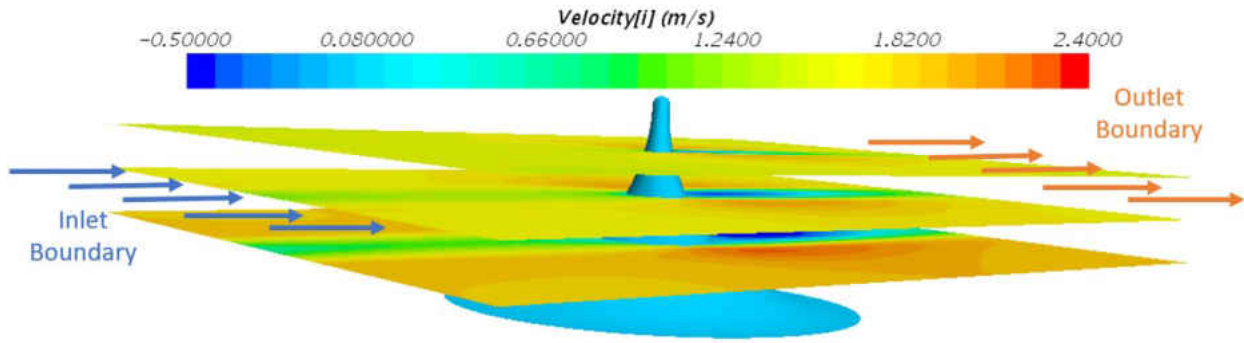
Figure 3.10: Two-Dimensional Plane Probe for Velocity Extraction

As it stands, Eq. 3.31 is not entirely accurate yet. This is due to its variable u_i being incompatible with the velocity extracted from the CFD explained above. The methodology of the extracted velocities have no errors, rather its the inherent problem with what DERM intends to solve for. As shown by Fig. 2.2 DERM extracts the velocity of the domain in order to mimic the effects of real explicit elements. The velocity of a flow within a porous media as if it were to be the only one present, in other words no porosity and in the context of this study no roughness elements. Thus the velocity DERM is attempting to extract and use is u_s, known as the superficial velocity. In contrast, the velocity extracted from the CFD is known as the interstitial velocity or u_i. The relation between the interstitial and superficial velocity is given by Eq. 3.33.

$$u_s = \frac{u_i}{\beta} \tag{3.33}$$

Substituting and implementing in Eq. 3.31, we arrive at the DERM term correlation that may be solved for Eq. 3.34. Note that the Re_a would also utilize superficial velocities instead of the

interstitial.

$$\iiint_V f_i^p \, dV = Drag(\Delta y) = 2u_s\beta \frac{\mu}{\pi\Delta a^2}\beta(y)(1-\beta(y))Re_aC_d\Delta y \qquad (3.34)$$

Similarly to before, the extraction of data needed for the heat transfer term of DERM, f_i^q, is relatively much less complex. The heat transfer term is only comprised of four major components being velocity, local a, fluid temperature and roughness temperature; two of which have already been solved for. In this case, the Re_a used for the drag term would also be used to solve for the Nu_d number. In regards to the Prandtl number, it was solved for using the domains viscous and thermal diffusivity terms, which remain constant but are inherently different from case to case.

The extraction of the last two major components, fluid temperature and roughness temperature, used previous methods described. In the context of the modeling done, a fixed prescribed temperature was set for the roughness element. Therefore, T_r becomes a single constant value throughout an entire case. T_f on the other hand is resolve for and is extracted with the same exact method as shown in Fig. 3.9. As before this extraction would comprise of multiple temperatures changing from cell-to-cell within a single ring-probe. As such, an avegrage of these temperatures were taken for a single value that can be implemented as T_f in Eq. 2.5.

Finally, in order to be able to compare the results obtained as functions of height. It is deemed more practical to view these comparisons as height being normalized, having a range from 0 to 1. In doing so, the geometric inconsistency between elements mentioned in section 3.1.1 is resolved and these problems can then be applicable to other roughness element with different dimensions, given they share similar boundary conditions. For simplicity differentiation, the values obtained from using Eq. 3.34 will be referred to as drag, and the values obtained from the CFD through Eq. 3.27 referred to as pressure loss. While the heat transfer obtained from the CFD and f_i^q will

be referred as, heat transfer and heat loss respectively. Each of these values are then compared to its corresponding counterpart, respective to the model (RANS or LES) and case (pressure drop or free-stream).

3.5 Model Validation

In order to ensure the pressure drop, free-stream velocity, and heat conjugation case studies are valid, Mart's experimental data was used as validation for the models explored [34]. The following is a complete validation study of the mesh, drag, and heat transfer studies.

3.5.1 Mesh Convergence Study

As required by standard CFD practice, a mesh convergence was preformed. The drag aspect of Mart's study was first to be inspected and as such the study used a base size mesh of 1×10^{-3} while refining the inside volumetric mesh until the output results no longer changed. As previously mentioned in section 3.3, a trimmer cell size was used with isotropic cell size distribution. Given the periodic boundary conditions on the side walls, it chosen a surface remesher would also be influenced by the volumetric condition. This volumetric mesh expand through out the domain but would only reach approximately 22% of its total height above its maximum peak. This would first ensure that it would not interfere with the cell quality adjacent to the prism-layers, and second, allow for the free-stream to develop without any compressible wall effects from the symmetry plane due to a coarse mesh being used.
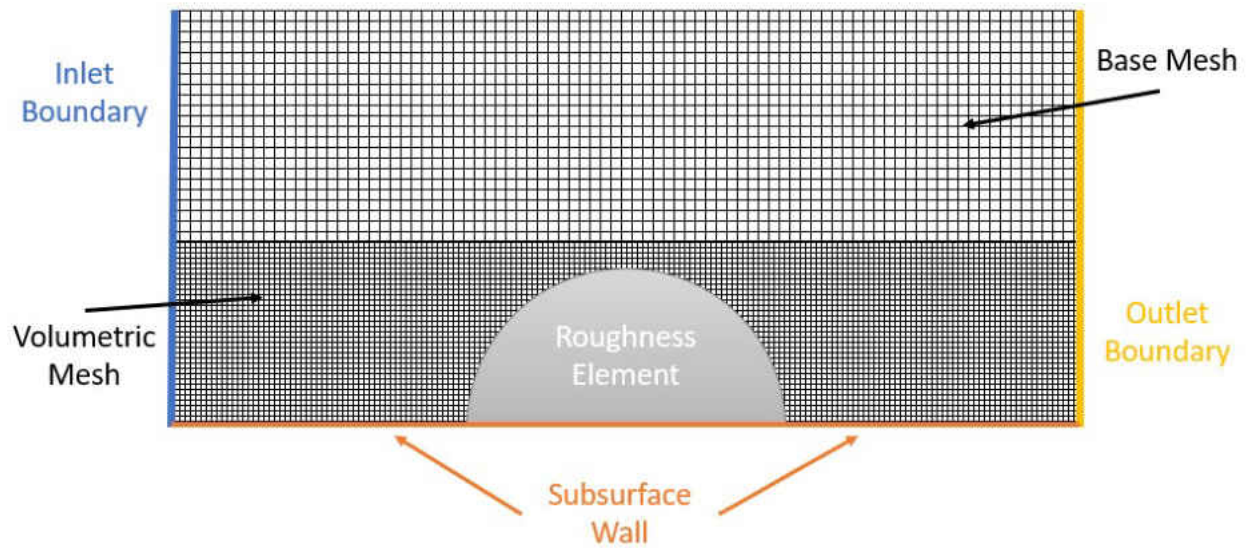
Figure 3.11: 2D Mesh Refinement

Fig. 3.11 shows the mesh refinement technique mentioned earlier. As seen, the volumetric mesh only influences the bottom portion of the domain all up until the top of the roughness element. Implementing the mentioned mesh technique to a volumetric mesh control within a CFD, we arrive at Fig. 3.12. Where for illustration purposes, a slice of the volume was taken within the domain. As seen, after a height above the roughness element, the mesh base size mesh takes control of the sizing scheme. Note the color scheme is kept consistent with Fig 3.3 so as to use as reference.
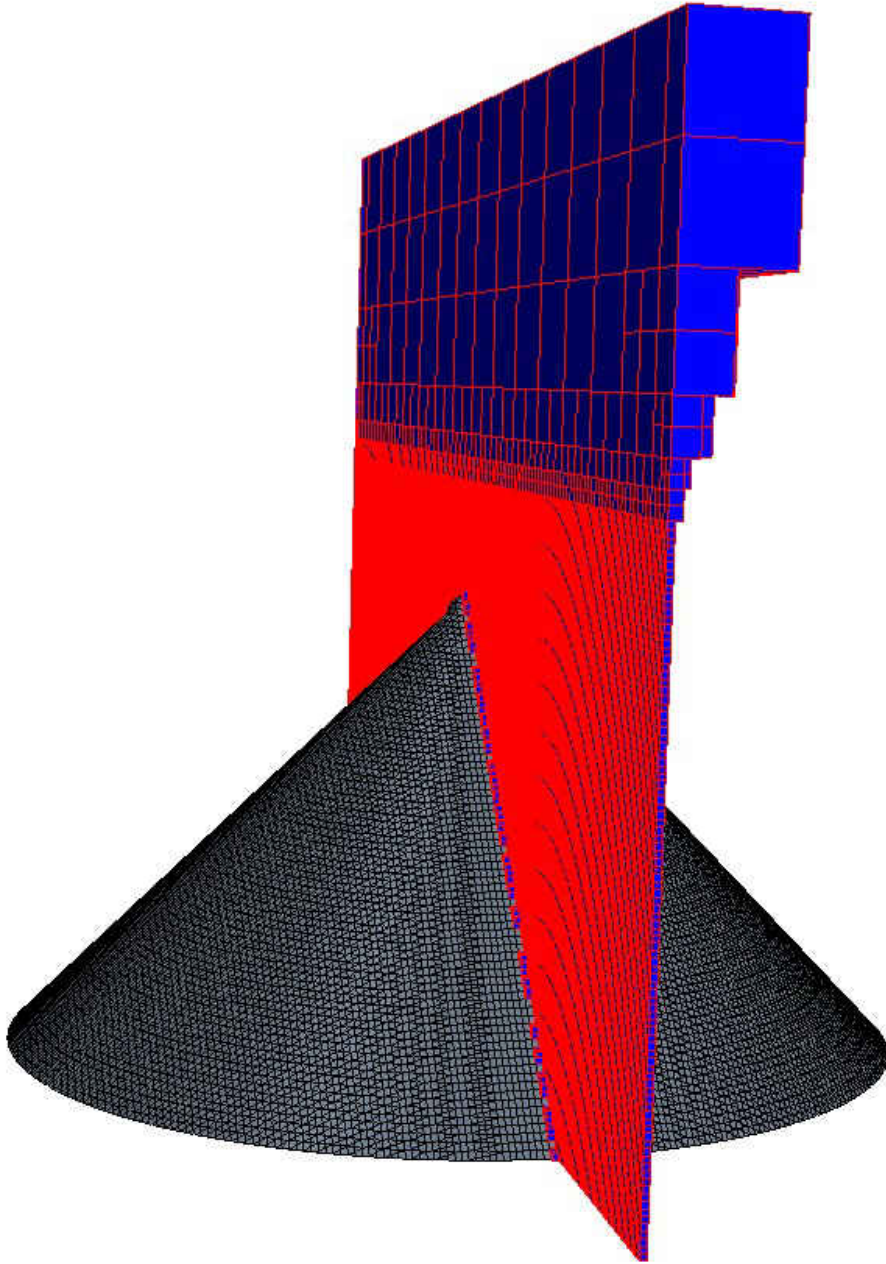
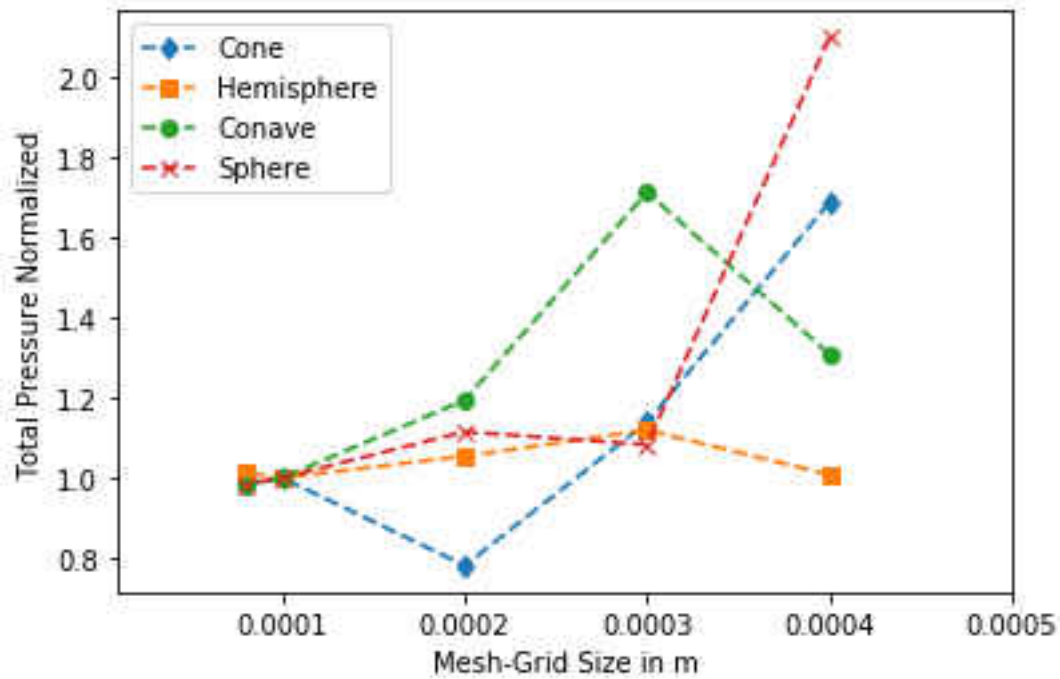Figure 3.12: Volumetric Mesh Refinement

Figure 3.13: Mesh Convergence Study

In order to compute a mesh refinement study, a scalar value was chosen and and inspected at each study with different volumetric sizes. Similarly to the evaluation methods provided in section 3.4.1, a single line probe was immersed within the refined mesh spatial-scheme. This single line probe would extract and resolve for total pressure. These data points extracted from each mesh refinement for every roughness element. Fig. 3.13 shows the convergence meshing metric for each element. The total pressure values were compared to their respective previous mesh values. Upon reaching a value of mesh that would no longer significantly effect the solution, the rest of the values were then normalized to that previous value of significant change. In this study it was found all cases converged at 1×10^{-4} with negligible differences with further refinement. Depending on the element, the number of cells computed would range from 5 to 6 million.

In terms of the heat transfer studies, a secondary mesh refinement had to be done. Some differences

48

were taken into consideration; only two of the four elements were place into the study, a solid domain also had to be refined which would increase cell amount, and a refined $WallY^+$ of at most 0.1 would also increase cell quantity. As the previous studied had converge at a mesh size of 1×10^{-4}, it was also chosen as the starting point for conjugate heat transfer. Similar to the probe method, the local fluid temperature was extracted from a line probe.

The mesh was refined two more times to sizes 8×10^{-5} and 6×10^{-5}. In both refinements negligible differences were extracted from the original base size of 1×10^{-4}. However, due to the change from trimmer to polyhedral mesh cell type and increase of prism-layer functionality, the number cells increased to above 7 million for all elements.

3.5.2 Coefficient of Skin Friction

In Mart's experimental set-up, he first resolved for the coefficient of skin friction for arrays of hemispheres and arrays of cones. He conducted ten different free-stream velocity cases, but ultimately only the first five were chosen for validation.

For both the cone and hemisphere elements a steady-state model and two unsteady-state models were chosen, better illustrated by Tab. 3.2. Given the nature of the study assume to be turbulent with eddies, a steady-state model would never give accurate results but was chosen for comparison. In terms of the Navier-Stokes resolved residuals for the steady-state model, a full convergence was never reached. However, the residuals would keep a consistent range in its progression to convergence. When this range of residual values became constant, an average of the resolved coefficient of skin friction of 1000 more iterations were taken. For the unsteady simulations, they were constructed to align more with the experiment. Given the experiment ran for less than 2 minutes, and a fully-developed condition was reached under 10 seconds within the model, each free-stream case was ran for 10 seconds at 5 *ms* time-step with an additional 10 seconds for time-

49

averaging data gathering.

Distinctive to the extensive methodology needed to extract drag and pressure loss, STAR-CCM+ provides a direct computation of drag coefficients. Given the assumptions of the experiment (assuming drag in $\hat{z}$ direction are negligible), the skin-friction drag coefficient or shear coefficient is straight forward to compute provided a reference velocity, area, and density.

Table 3.3: Shear Coefficient Referenced Values.

Referenced Parameters	Case 1	Case 2	Case 3	Case 4	Case 5
Velocity (m/s)	2.5	5.0	7.5	10	15
Density_C ($\frac{kg}{m^3}$)	1.149	1.166	1.172	1.175	1.16
Density_H ($\frac{kg}{m^3}$)	1.145	1.161	1.167	1.171	1.182
Area (m^2) 1×10^{-5}	7.129	7.129	7.129	7.129	7.129

Tab. 3.3 represents the reference parameters needed to obtain the skin drag coefficient. Note the density is made of two different values at each case for the cone and hemisphere, notated by C and H respectively. This alternating density is due to Mart's experiment running both friction and thermal tests simultaneously influencing the change in fluid-thermal properties.
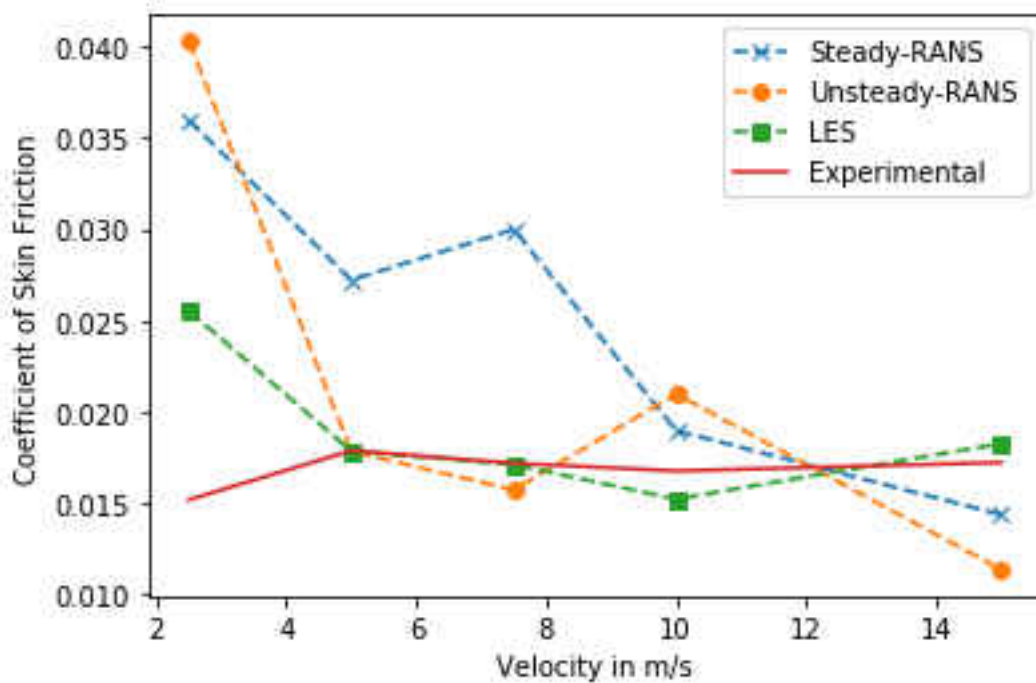
Figure 3.14: Hemisphere Element Drag Model Validation

Upon extracting the values, all three models had similar initial results for the hemisphere. As can be seen by Fig. 3.14, all models deviated from its initial case of 2.5 m/s with the RANS models deviating significantly more so than the LES. However excluding the initial case, the LES follows the experimental values of at most a 9% margin of deviation. While the unsteady-RANS is significantly more accurate than the steady-RANS, when compared to the LES, it is still not as accurate. This could mean when applying correlations to the model, there should be significant difference between the unsteady-RANS and the LES pressure loss and drag.
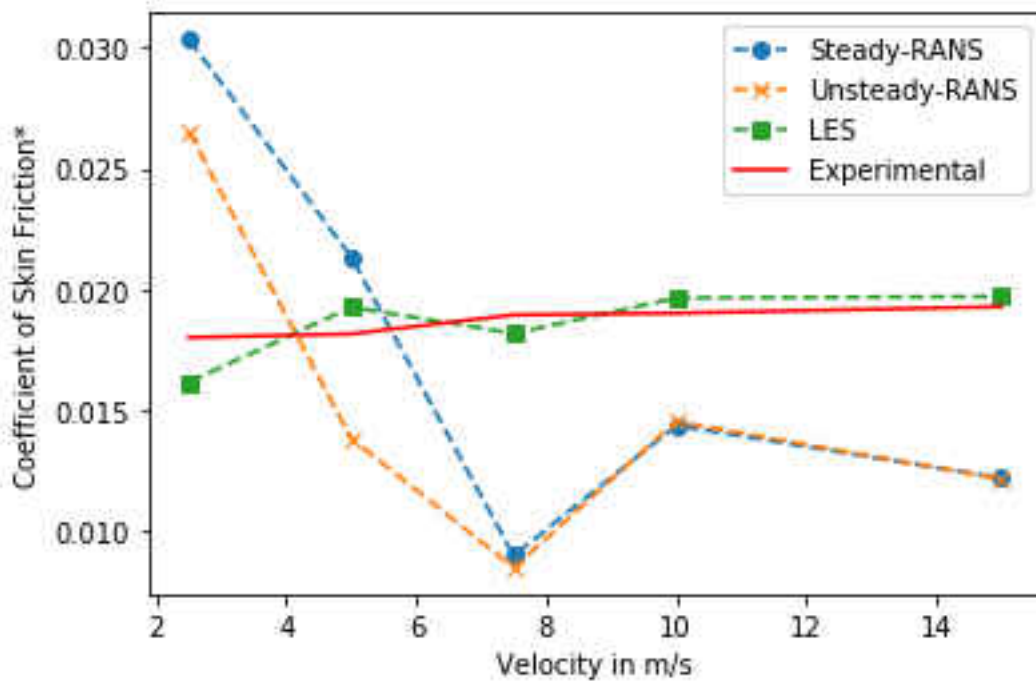
Figure 3.15: Cone Element Drag Model Validation

An exact study was preformed for the cone and Fig. 3.15 shows the results obtained from the validation study. Unlike the hemisphere element, the unsteady-RANS model proved to be ineffective with most errors (with the exception of the second case) above 30%. While CFD standard requires this range to be under 10% to become an accepted model, and for the latter cases it appears to replicate the steady model values. The LES model is then an improvement on the unsteady-RANS, essentially under the 10% margin as required.

An interesting point within this case studies is the modeling and solution of the skin-friction. While the LES is expected to preform better when compared to the DERM predictions, it does not offer much more complex computation in than the RANS model in context of skin-friction. Ideally, skin friction is resolved within the boundary layer and as stated previously, the LES model (or DES) is not the true full LES model. Given the hybrid aspect of the model, the RANS averaging

would replace the LES computation within the boundary layer. Its without question the LES does influence the computation within the boundary layer (through connect cells) but does not directly solve for it. It is possible that a full implementation of LES within the boundary may refine the results and could adjust the initial case within an acceptable value instead of an outlier.

3.5.2 Heat Transfer Coefficient

Unlike the skin friction, the heat transfer experiment was only validated through a steady-state RANS model of the first five free-stream velocities for the hemisphere and the cone. Similarly to the drag steady-state model previously described, the heat conjugation steady-state model was also taken at 1000 more iterations for averaging upon reaching a near-like residual convergence.

Extracting the heat transfer coefficient became trivial compared to previous methods. STAR-CCM+ natively solves for the heat transfer coefficient with the appropriate boundary conditions like the ones used in this thesis. A surface average of the HTC in both the plate and roughness element was taken.
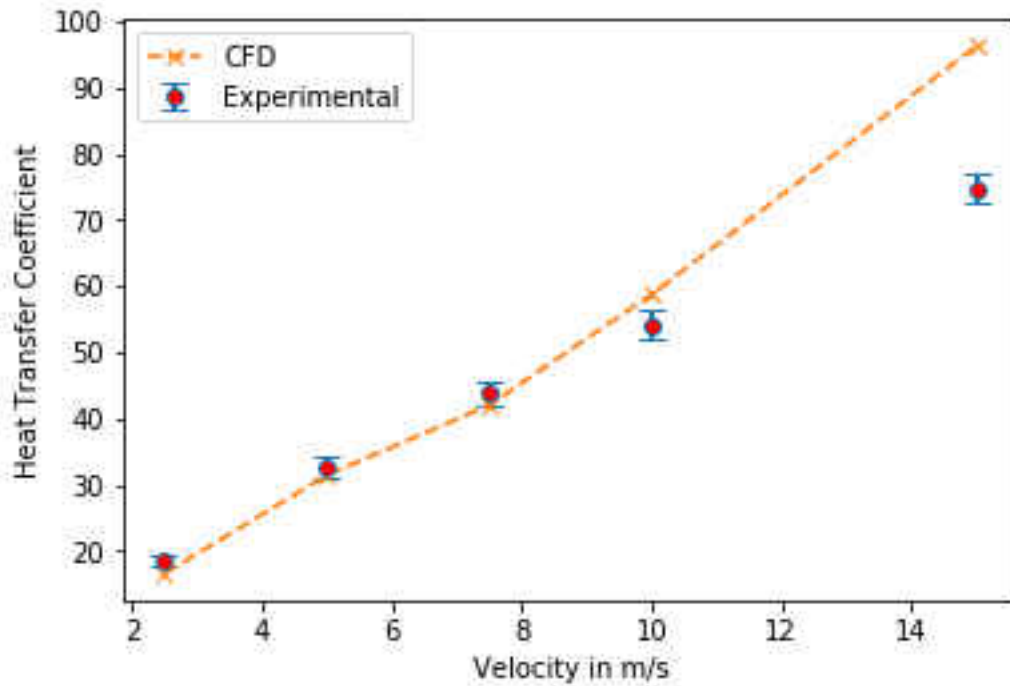
Figure 3.16: Cone Element HTC Model Validation

Contrary to the drag validation where cases would increase in accuracy with increase in velocity, Fig, 3.16 shows an accurate capturing of the HTC initial cases with an eventual divergence with increasing velocity for the cone element.The HTC experimental values had error bars to represent experimental error, and while it may appear the first three cases fit inside these error bars, only the 5 m/s case did. Even still, with the exception of the final case, all other 3 cases were within a 10% margin of error which surpassed the authors expectation of a steady-RANS model.
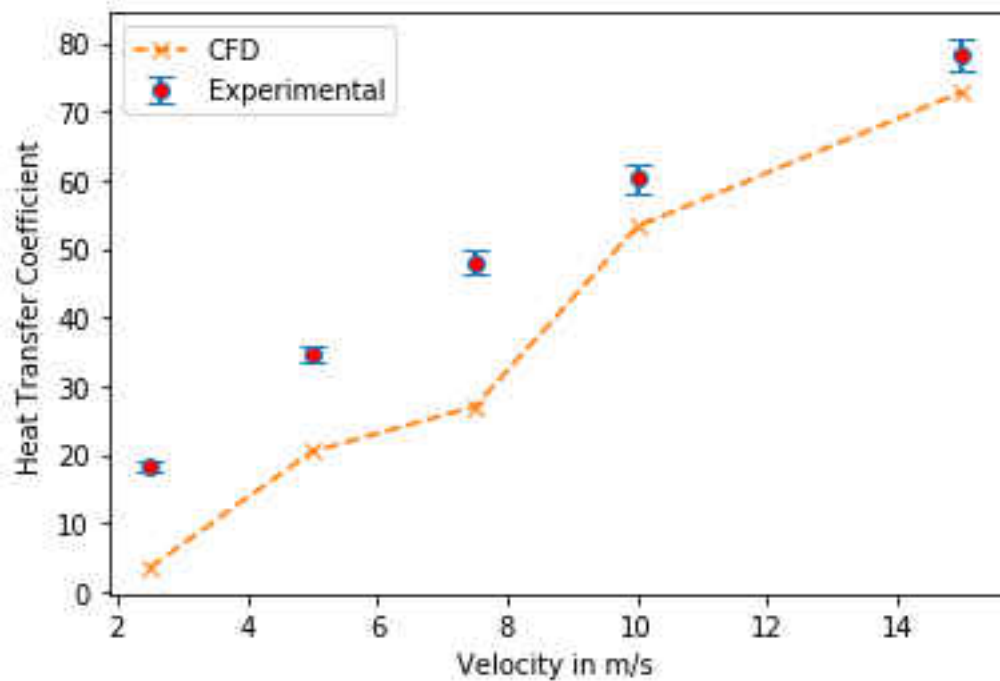
Figure 3.17: Sphere Element HTC Model Validation

The sphere HTC solution had a higher divergence and opposite effect in comparison to the cone. Consider Fig. 3.17, the initial cases had high error but as the free stream increased the values would eventually reach an acceptable margin of error (8%). This phenomenon breaks away from the standard the cone set, being an acceptable model for low velocity profiles. This opposite effect can be a direct influence of the element's geometry to the model and velocity prescribed.

The key to this difference between drag coefficient and HTC models would be the development of eddies and how it directly relates to its coefficient it is solving for. Starting with the drag coefficient, its seen that with increase velocity the predictive accuracy increases to match the experimental with improving the time-scheme model. With an increment of speed, it directly relates to an increase of larger-scale eddy development. As such, with improving model and velocity the capturing of drag as a direct result of these eddies became easier. Where the heat transfer coefficient model differs,

is its sole computation of a single model. The same principle explained before stands, where with an increase of velocity, a development of eddies should occur. Therefore, with a steady state incapable of accurately capturing eddy development as they are inherently unsteady, it follows that with an increase of velocity the ability to solve for the HTC diverges as a direct result from these circulations. This theory breaks upon the consideration of the hemisphere. It is possible the cone element may provide better results at lower velocities, whereas the sphere preforms better at higher velocities

CHAPTER 4: PRESSURE DROP EVALUATION

This chapter presents the results of the twenty-four pressure drop cases utilizing RANS and LES models. The sections below are divided by modeling time-scheme used. For each model, there are three cases which are known as case 1, case 2, and case 3; where each case increment means a higher pressure drop value. Earlier in chapter 3, it was discovered the the modeling is invalid for inlet velocities of 2.5 or lower. As such these cases prescribed pressure drops that condition velocities higher than 2.5. Note the drag and pressure loss calculated are from a single element and not the total drag of an array. Additionally, the pressure loss (CFD calculated values) is taken as the baseline and DERM is measured of its discrepancy from it. This is due to the modeling being validated as seen in sections (3.5.1 - 3.5.2)

4.1 RANS

As a comparison case, the steady-state Reynolds-Averaged Navier-Stokes or RANS model was implemented for all three cases. As previously described, RANS modeling takes an averaging approach towards resolving general physics equations. This averaging is assumed to intake much of the error within the flow field given the eddies that should develop. This averaging would essentially remove a great quantity of eddies as they would be averaged out over a set of mesh cells rather than resolved for at each cell. Due to this, it is expected the RANS method to contain the most error compared to the other models as it directly influences DERM's approximation capabilities via the velocity field averaging.
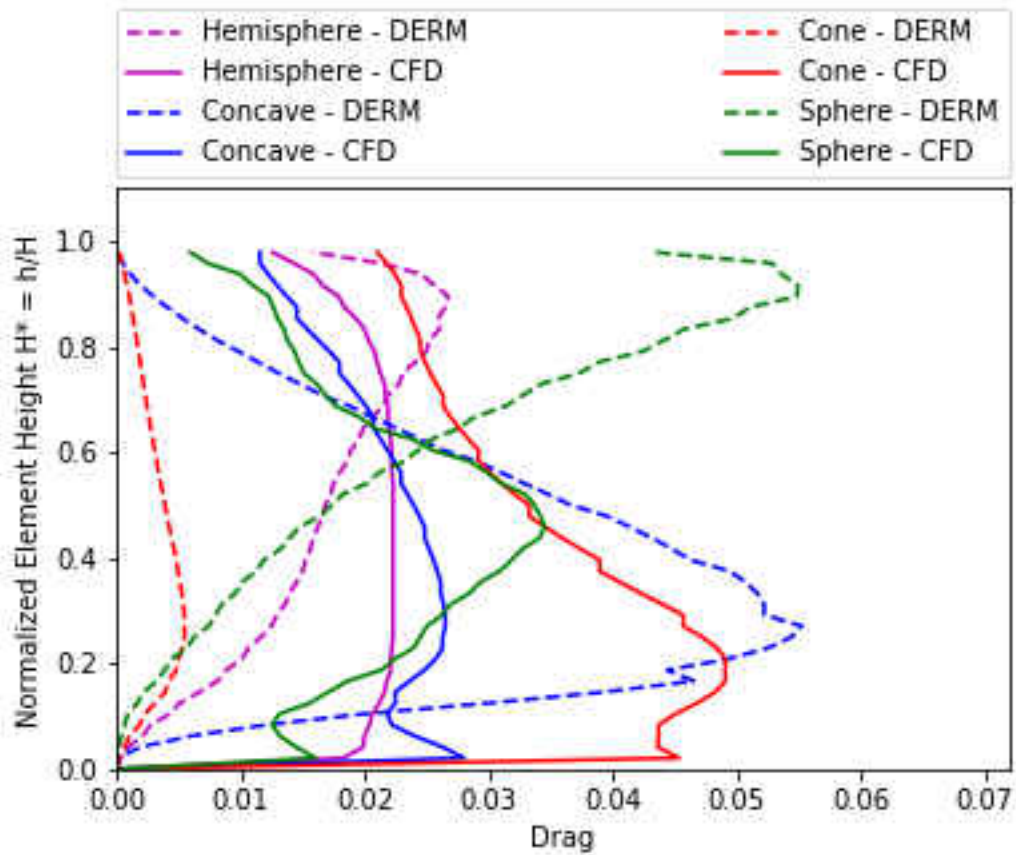
Figure 4.1: Drag & Pressure Loss RANS Modeling: Case 1.

After the extraction of data for each element, they were compared to check for any deviations. Fig. 4.1 compares the drag to predicted pressure loss for each element for only the steady-state RANS model, where the solid line represents pressure loss and the dashed line being drag. Upon inspection there appears to be not be a trend but rather deviations through out the entirety of the domain. However there are some consistent trends within their own predictive category.
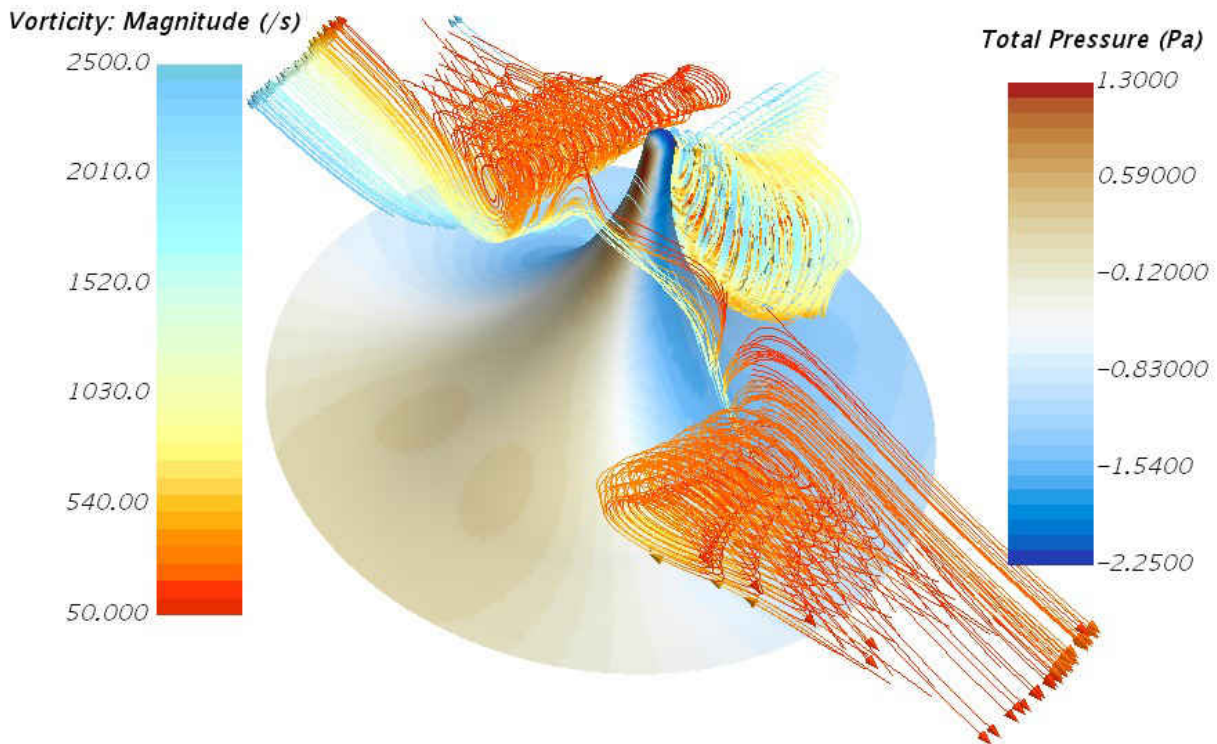
Figure 4.2: Vorticity of Concave Element Case 1.

From pressure loss being measured by the CFD, it tends to peak at earlier heights and have a minimum negative slope as it approaches its maximum height. The drag being DERM predicted has a near opposite effect where, with the exception of the cone element, has a late peak with an immediate drop to reach zero. This end peak can be considered a substandard approximation from DERM, because at this peak a separation of the boundary layer would occur prompting a sudden increase in the shear-strain rate of the fluid followed by an increase of vorticity behind the element at its peak. This idea can be see by Fig. 4.2, where the vorticity streamlines appear directly being the element tip.
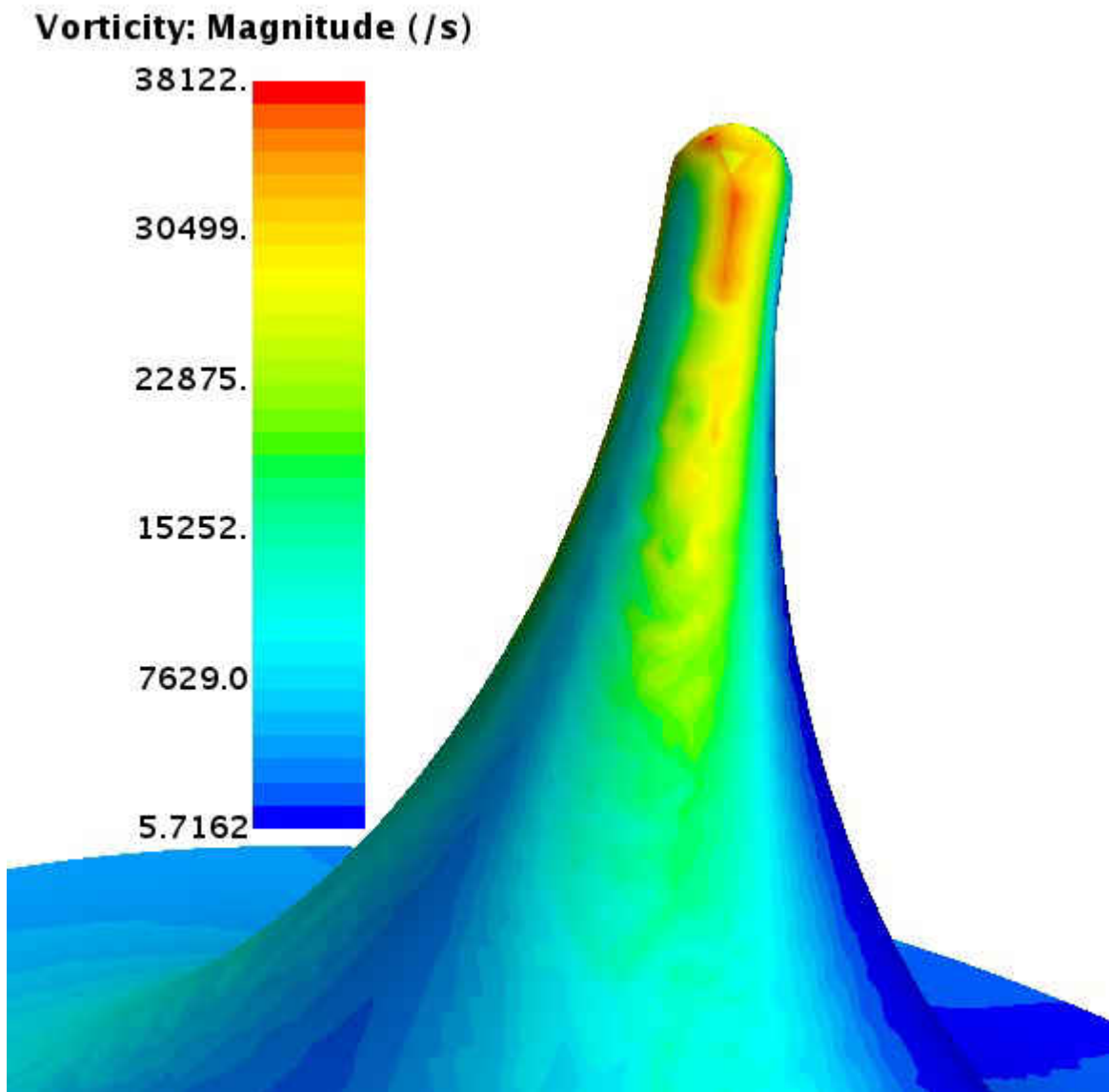
Figure 4.3: Vorticity Resolved Concave Element Case 1.

As further evidence provided by Fig. 4.3, counter part of Fig. 4.2, the CFD does not drop down to zero because there are still tip effects that DERM is unable to predict. The vorticity resolved shows there to be high separation at the tip which would increase drag, not dissipate. We further investigate this observation with case 2.
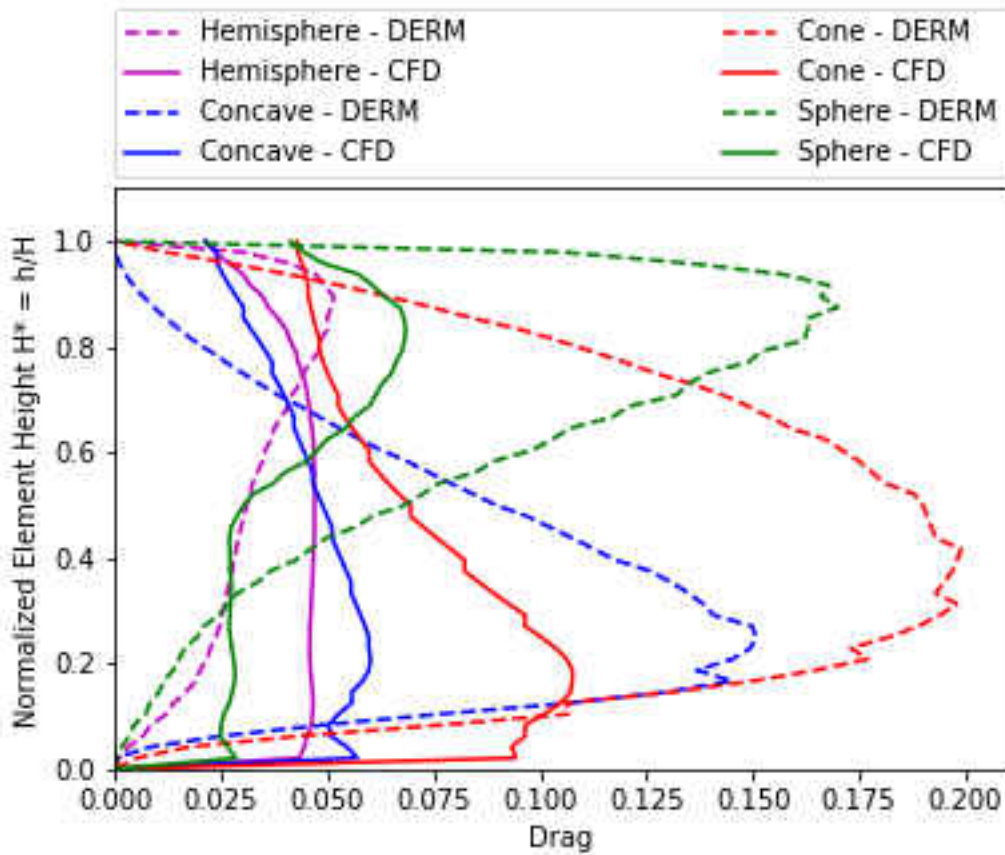
Figure 4.4: Drag & Pressure Loss RANS Modeling: Case 2.

As previously observed, DERM has a tendency to drop to zero with a steep slope relative to the CFD predicted. Fig. 4.4 shows the same trend as previously mentioned with an additional new one. Unlike before, case 2 shows a significant portion of each element DERM predicted drag to be higher than the predicted drag from the CFD (pressure loss). Furthermore, each element appears to reach a maximum at virtually the same height with only followed by a quick deviation. Whats more, the sphere and hemisphere tend be the closes of whos drag and pressure loss nearly follow the same trend and magnitude.

Case 3 is expected to follow the same pattern as such, a parody plot of all three cases was compiled

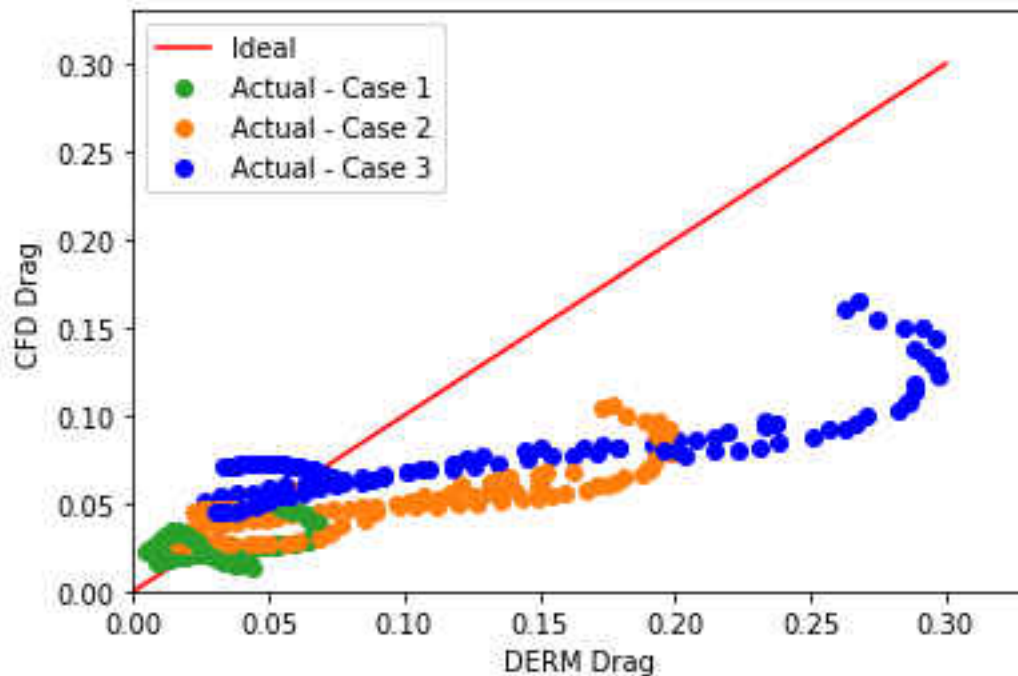without distinction of the four roughness elements.

Figure 4.5: Pressure Loss vs Drag Parody RANS.

This parody plot is shown by Fig. 4.5, where the red straight line indicates the ideal scenario (i.e CFD = DERM). All three cases regardless of elements were compared to eachother in this plot. It can be seen that with increasing case (pressure drop) the predicted drag tends to be over-predicted by the DERM drag prediction. If we refer back to Fig. 4.4, the maximum of each element of the DERM prediction would be towards half of its maximum height for cone and concave elements, and reaching the maximum height for sphere and hemisphere. If compared back to Fig. 4.2, it supports the idea that DERM is essentially over-predicting where vorticity is at its highest. This could be an error passed on from the CFD due to RANS being able to accurately capture the eddies forming affecting the velocity implemented in DERM.

4.2 LES

As method of refinement, an unsteady-state hybrid RANS/LES model was selected. It is expected this model to be more accurate in comparison to the RANS model studied in the previous section. Contrary to the previous model, this Hybrid model or know as the Detached Eddy Simulation (DES) only prescribed an averaging methods at the boundary layer. Depending on the length-scale of the turbulence it would apply either an LES or RANS model within the domain. It is due to this distinction that DES is believed to be the more accurate relative to RANS.
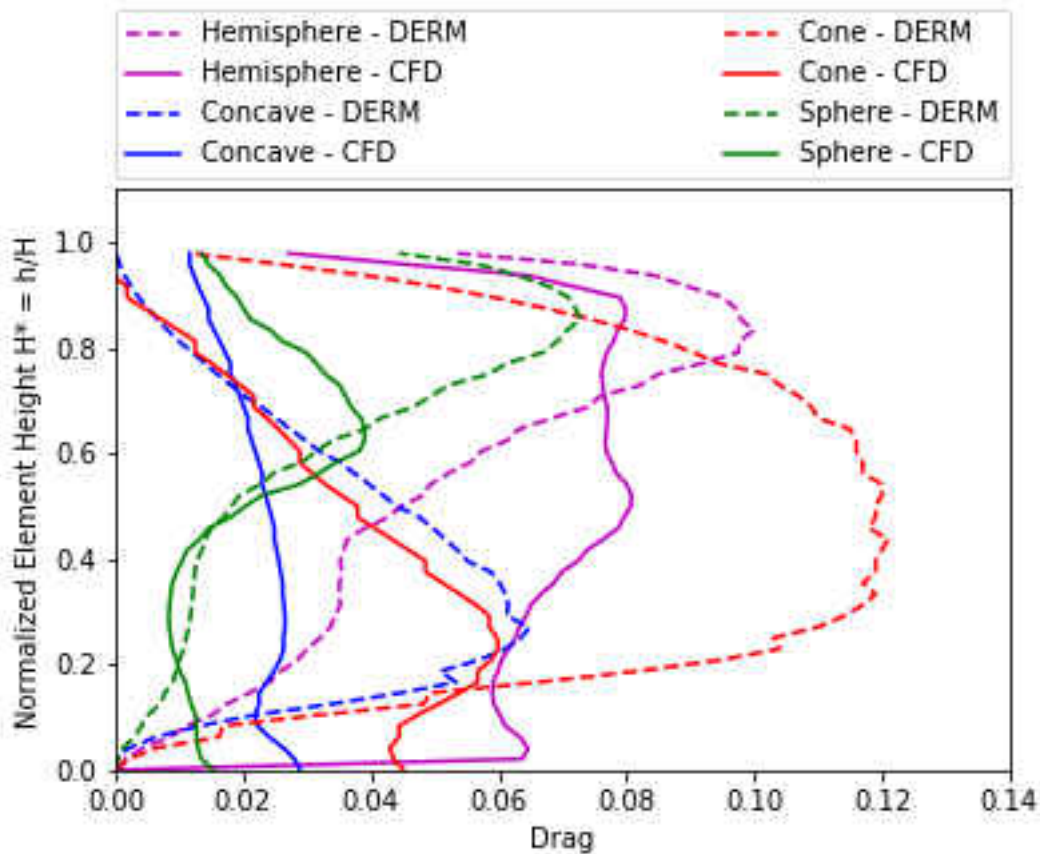

Figure 4.6: Drag & Pressure Loss LES Modeling: Case 1.

Consider Fig. 4.6, where the comparison between drag and pressure loss is shown for case 1. Contrary to the RANS case 1, there are distinct patterns and trends the LES was able to capture. There are clear trends between drag and pressure loss in the hemisphere and especially the sphere element. DERM continues to have a tendency to over predict relative to the CFD. As before, wing tip effects are still in play, were DERM continues to drop to zero as it reaches the maximum height. If we make the assumption that the LES model is able to accurately predict the velocity fields within the domain taking into account the vorticity, then DERM is being affected at the tip more so from its other components.
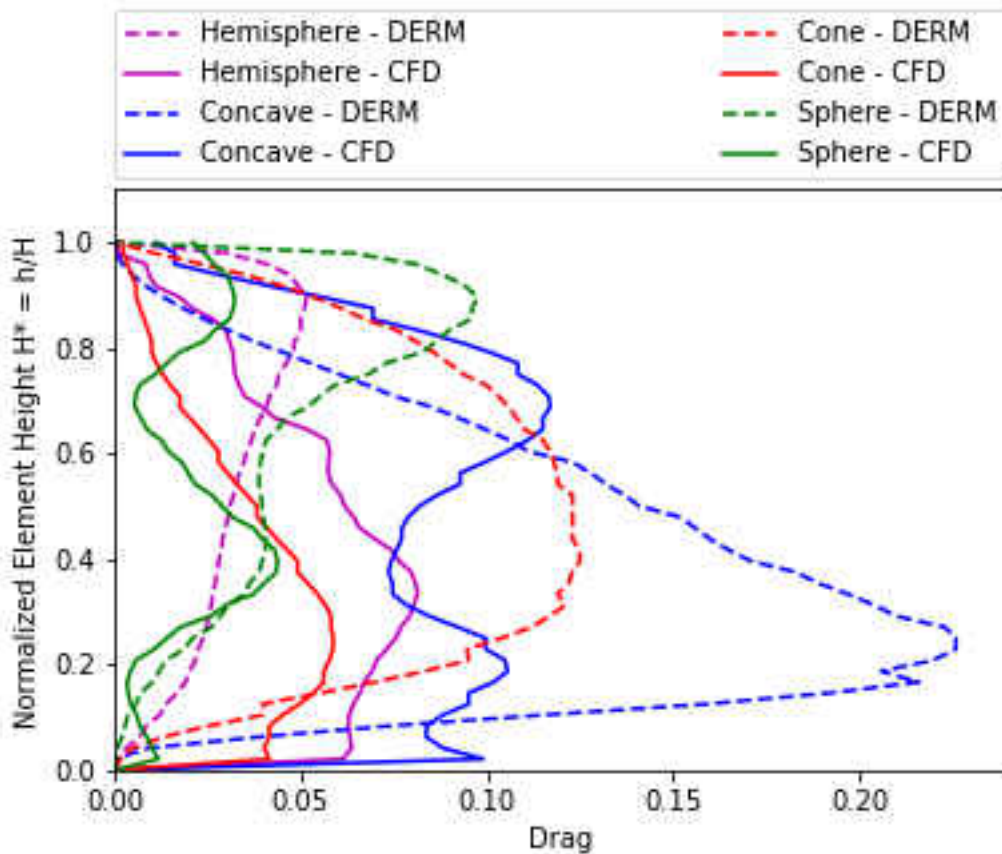

Figure 4.7: Drag & Pressure Loss LES Modeling: Case 2.

Lets consider Fig. 4.7, representing Case 2. Similar to case 1, the hemisphere and sphere follow along with each other with a final deviation. This case sparks an interesting point. At multiple points through out the height, the drag has a sudden loss followed with spike for almost all of the elements. This implies there is a negative pressure or propulsive force at those heights which reduces the induced drag, giving the resulting pressure loss a wave length appearance.
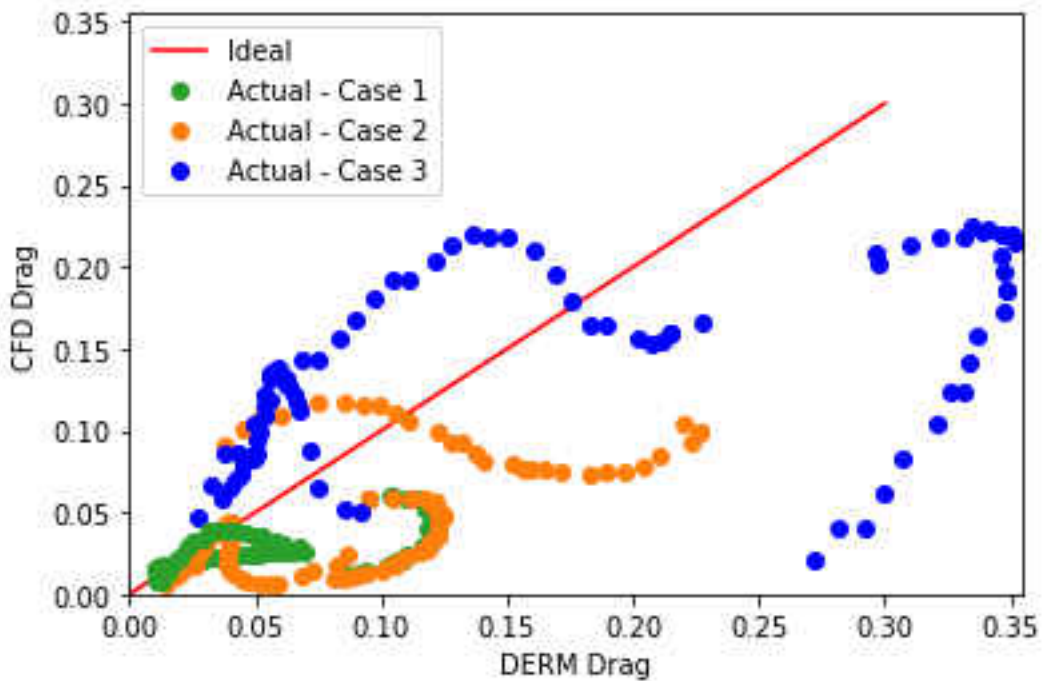

Figure 4.8: Pressure Loss vs Drag Parody LES.

For better comparison of all cases, a parody plot was constructed eliminating the distinction between elements provided by Fig 4.8. As predicted, the LES is capable of attaching closer to the ideal scenario. It case 3, it shows there are some significant deviations as over predictions from DERM. It was suggested that the LES would be capable of reducing the discrepancies at higher pressure drops due to the removal of an averaging method where eddies can then be resolved for. From this figure, we can safely say that when comparing to the RANS parody plot, the discrepan-

cies were significantly reduced.

Lets consider Fig. 4.9, where a comparison of LES resolved vorticity values of the hemisphere element is introduced.
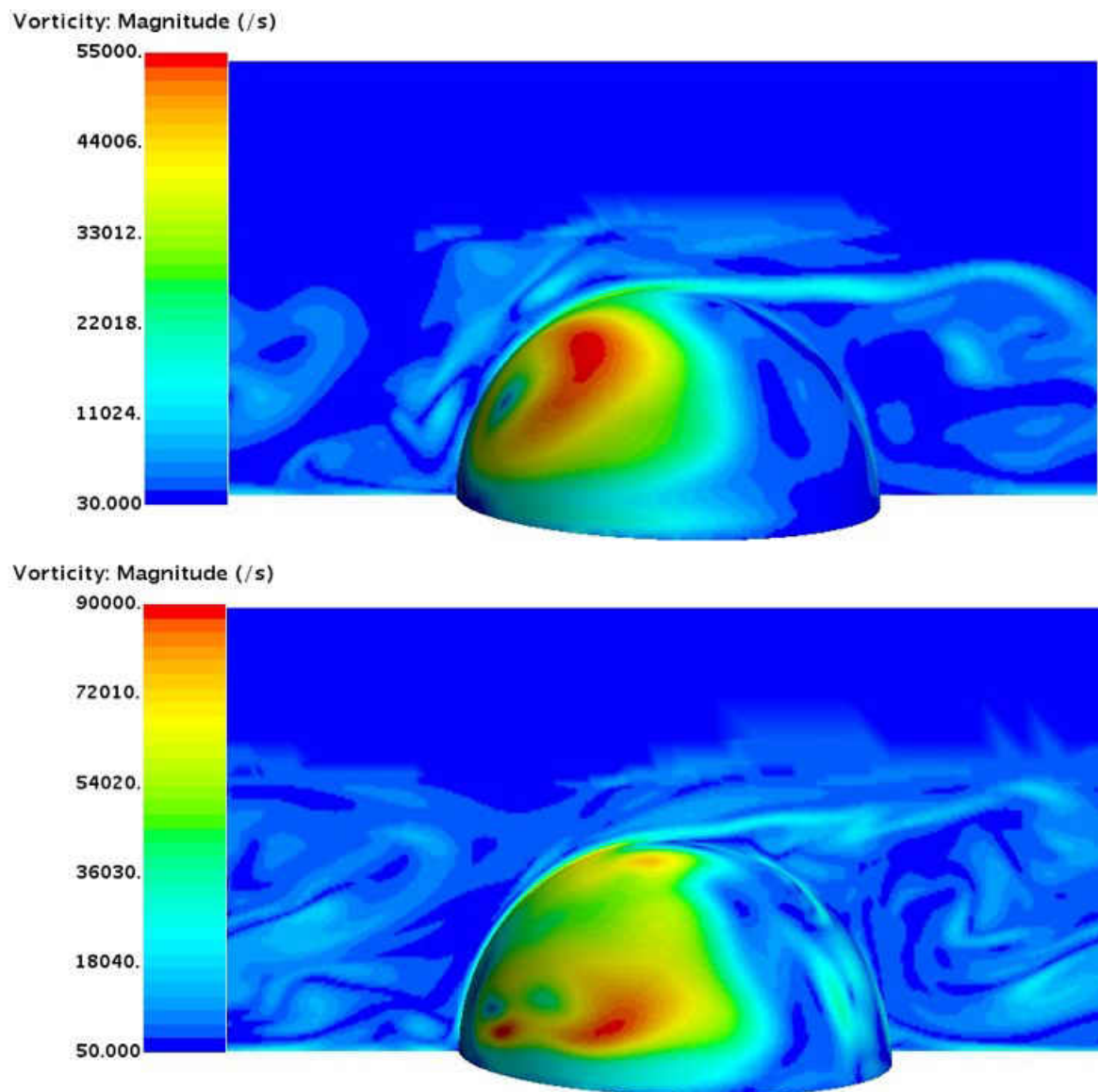

Figure 4.9: Comparison of Case 1 (top) and Case 3 (bottom) Hemisphere Vorticity.

From this figure we can visually see the eddies being resolved at the back of element, with some also being distinguishable at the front of the element for case 3. Even though the LES model is capable of resolving for these features in an improved manner than before, it also adds more error probabilities when applying it to DERM. With higher vortex values, the capability of accurately transferring the correct velocity profiles to DERM decreases. In this figure, case 3 pressure drop essentially caused a doubling in vortex magnitude. Meaning as the pressure drop increases, DERMs effectiveness decreases.

CHAPTER 5: FREE-STREAM CASE

This chapter reviews the results gathered from two elements within five free stream velocities under different models. This case is different due to its condition within the fully-developed condition. The previous cases were designed to control a pressure gradient; with the implementation of a mass flow condition we are able to specify velocity directly. In doing so, the five cases utilized have been validated a degree with the addition of analyzing the heat transfer effort f_i^q along with the drag effort term f_i^p. Two different unsteady models are utilized in this chapter. The two models are ran for 10 seconds with a 5 ms time-step, and an additional 10 seconds for data averaging.

5.1 RANS

The following are the evaluations of the cone and hemisphere under a steady-state RANS modeling.

5.1.1 Drag Resolving

The drag was resolved by both the CFD and DERM provided effort terms. As previously mentioned, the RANS model is unlikely to capture accurate values but it is necessary to set a base line. The skin-friction resolved for in section 3.5.2, showed a significant deviation and so it is expected for said deviation to translate onto the effort term.
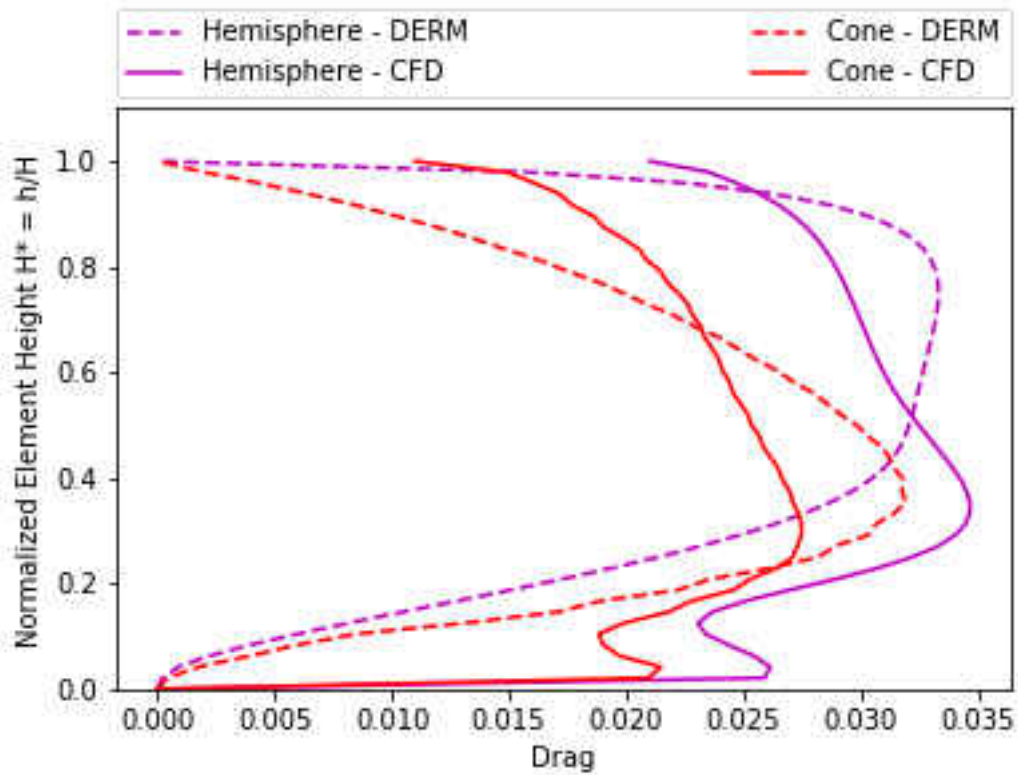
Figure 5.1: Free Stream Case 1 RANS Model.

The deviations provided by a comparison of the drag and pressure loss can be seen in Fig. 5.1. As a stand alone case, neither the cone or hemisphere show signs of major deviation that has not already been record. Rather excluding the tips being the maximum and plate, the drag and pressure loss were within relatively decent proximity. This is a representation of case 1 being the worst preformed when tested for the coefficient of skin-friction.
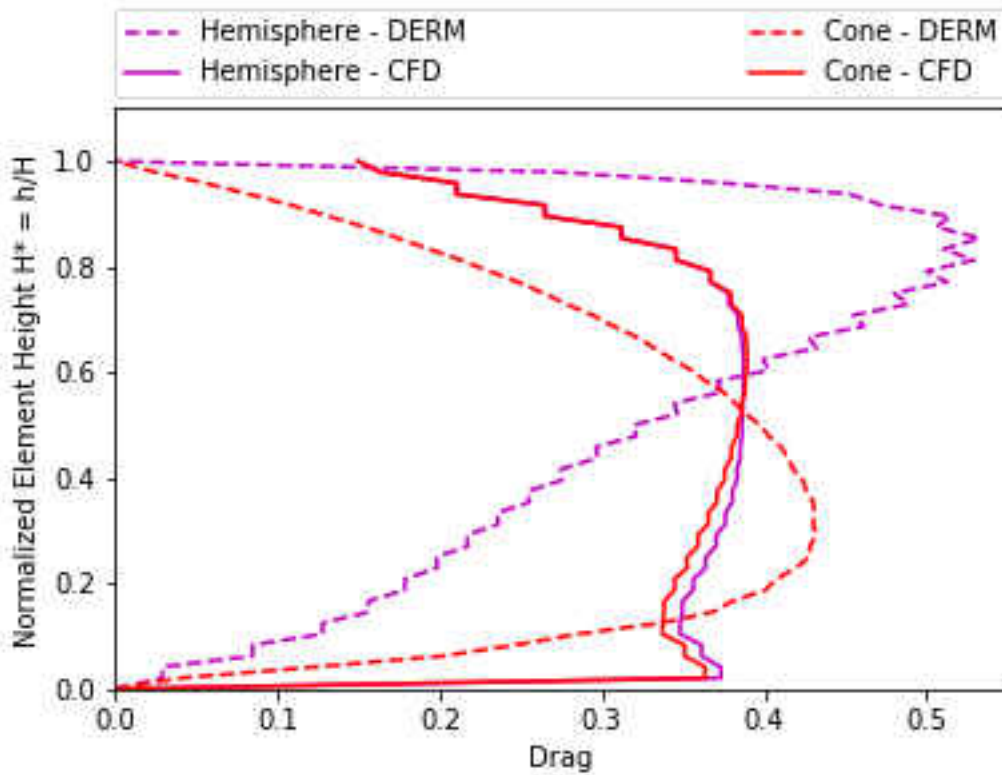
Figure 5.2: Free Stream Case 4 RANS Model.

Thus two cases that preformed best under RANS modeling for the coefficient of friction were case 4 and 5, seen by Fig. 5.2 and Fig. 5.3, respectively.

Case 4 is an interesting scenario as the pressure loss solved by the CFD is practically the same for both the hemisphere and cone. Furthermore, with increasing velocity the peak of the hemisphere DERM prediction moves father up its vertical. It was expected for the results to refine to a degree upon inspecting a higher case but instead the deviations grew.

Figure 5.3: Free Stream Case 5 RANS Model.
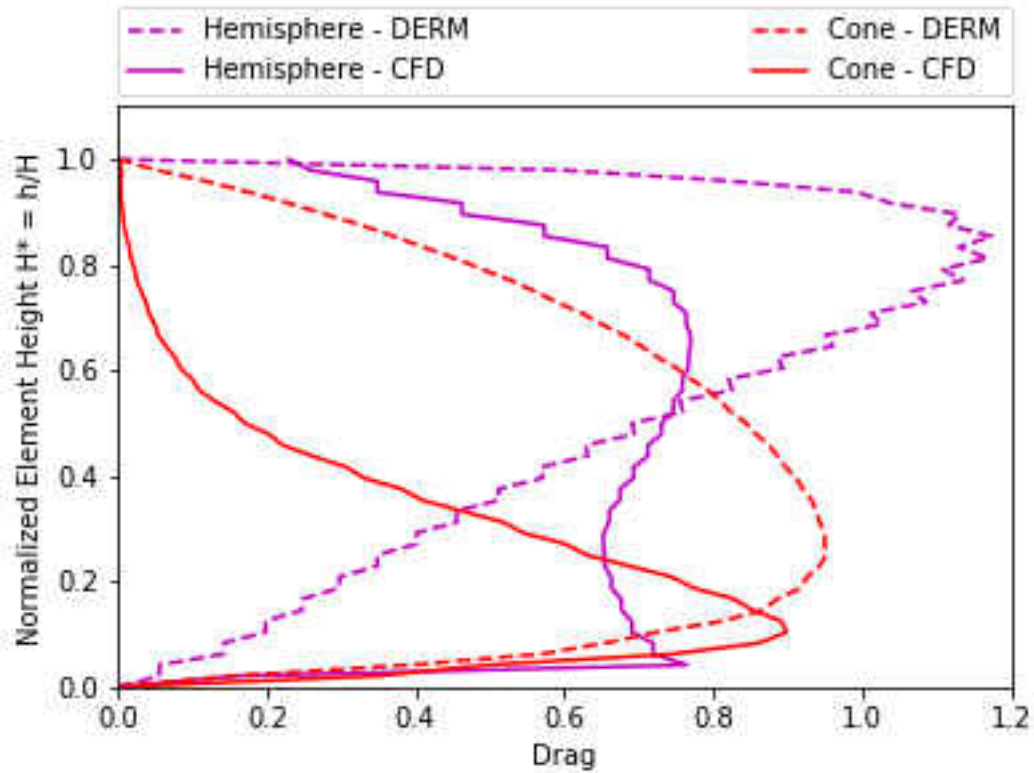
Case 5 is similar in that there is not foreseeable trend within the graph, only an increase of deviation. In particular, the cone began to be skewed towards its base with a dramatic decrease in drag before $\frac{1}{4}$ of the way up. In doing so however, it captures the drag predicted by DERM with great accuracy but it quickly deviates. The hemisphere relatively does not change much visually. In terms of drag itself, the magnitude increased with slight changed in trend.

For a comparison of all five cases, a parody plot was constructed again containing both elements. As seen in Fig. 5.4, it appears the cases that follow the ideal scenario closes would be those cases with lower velocities. Most cases do relatively well at maintaining near the idea case however, case 5 has two huge discrepancies. One leans largely towards CFD drag and the other favors DERM

drag, but both eventually cross the idea line These are better seen by separating it by roughness element.
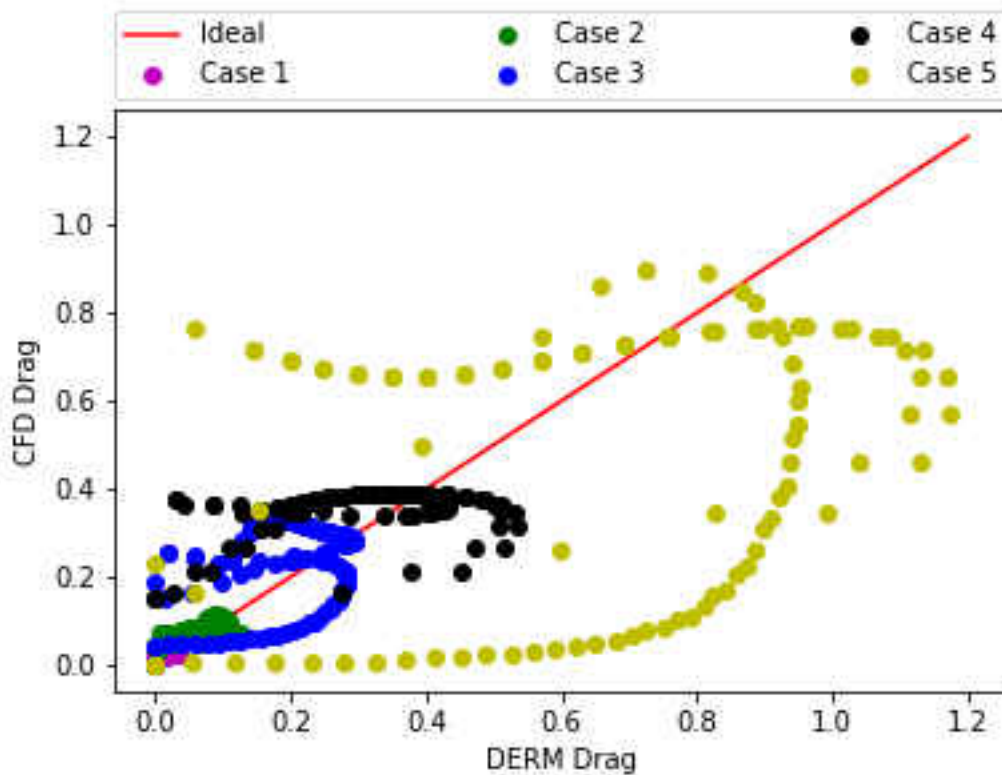
Figure 5.4: Free Stream RANS Parody.

Fig. 5.5 and Fig. 5.5 represent the separated parody plot by element being the cone and hemisphere, respectively. When comparing the two figures to the original, it appears the it is the cone element which favors DERM drag for cases 3 and 5. However for the sphere, cases 3, 4, and 5 leaned towards the CFD Drag but did end up crossing the ideal line with higher velocities. As proven from the pressure drop cases, these scenarios are meant to improve with model refinement.

Figure 5.5: Free Stream RANS Parody Cone Element.

Figure 5.6: Free Stream RANS Parody Hemisphere Element.

The main contribution of DERM is its ability to enhance convective heat transfer via its energy and momentum source term. While momentu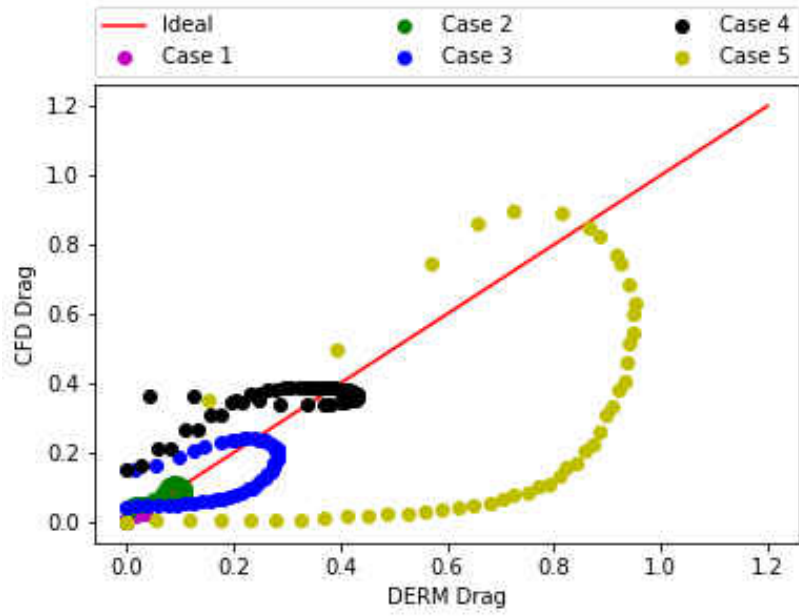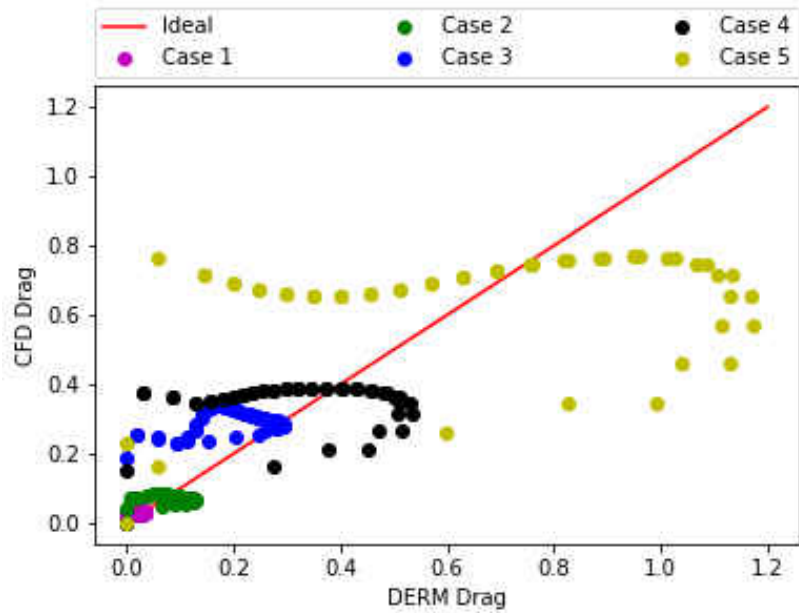m source term is a function of f_i^p, the energy source term contains both effort terms f_i^p and f_i^q. Given the inclusion of the drag effort term within both source equations, gives reason for the emphasis at reviewing the drag effort term. Even so, the heat transfer effort term is just as important. This section dedicates an analysis at utilizing steady-state RANS and comparing the results other RANS model applied to the drag effort term.

From the validation section, it was noticed the hemisphere model worked well under high velocities but not accurate under low velocities. The opposite can be said about the cone element. Due to this only the first and fifth cases will be evaluated for the cone and hemisphere, respectively, followed by a parody plot of all cases.
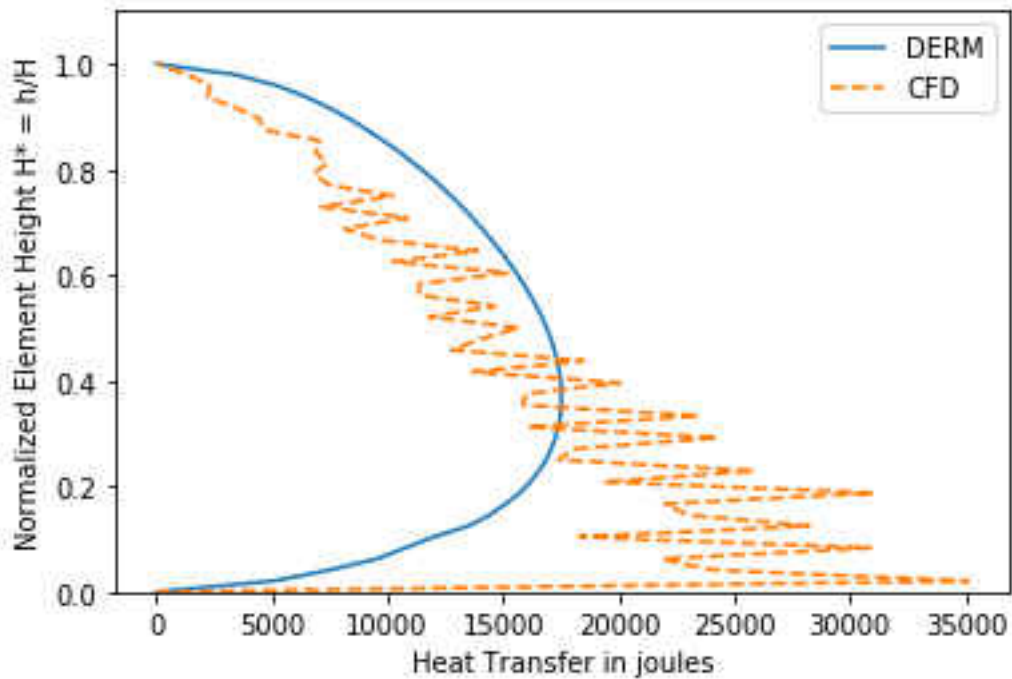

Figure 5.7: Cone Evaluation of CFD and DERM Heat Transfer: Case 1.

Consider Fig. 5.7, where the DERM predicted values are compared to the CFD extracted values. As noted before, DERM has an inability to preform well on the tip ends of the element. Where in drag the highest probability of error would be located at the tip where separation would occur. In heat transfer it becomes the bottom of the near the subsurface. Given the point nearest the surface to have highest temperature, it would be logical to assume its where the highest point of heat transfer would be located. The CFD is able to predict this point however DERM cannot. This plot further suggest RANS inability to capture domains with unsteady flows. The unevenness of the heat transfer predicted by CFD is a consequence of using RANS as a full convergence (even with averaging) cannot be reached.
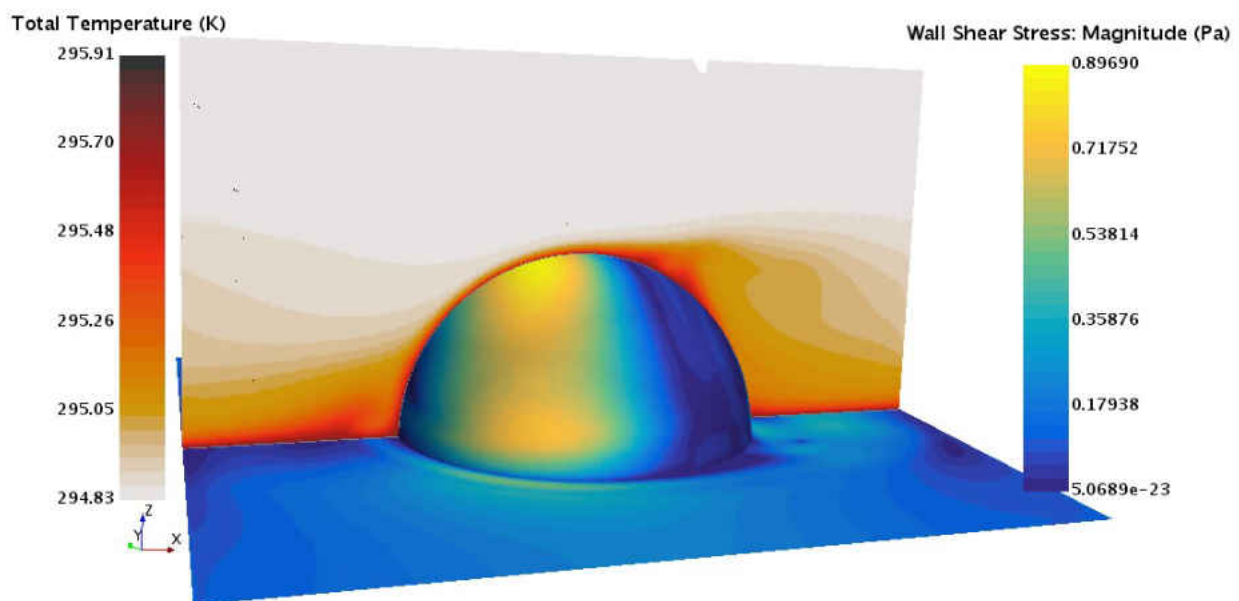
Figure 5.8: Heat Dissipation from Hemisphere: Case 5.

Case 5 data is then extracted, evaluated and plotted in Fig. 5.9 for analysis of the hemisphere element. Similar to the cone element, the bottom half is where a majority of errors are contained with an unsteady evaluation of the heat transfer values.
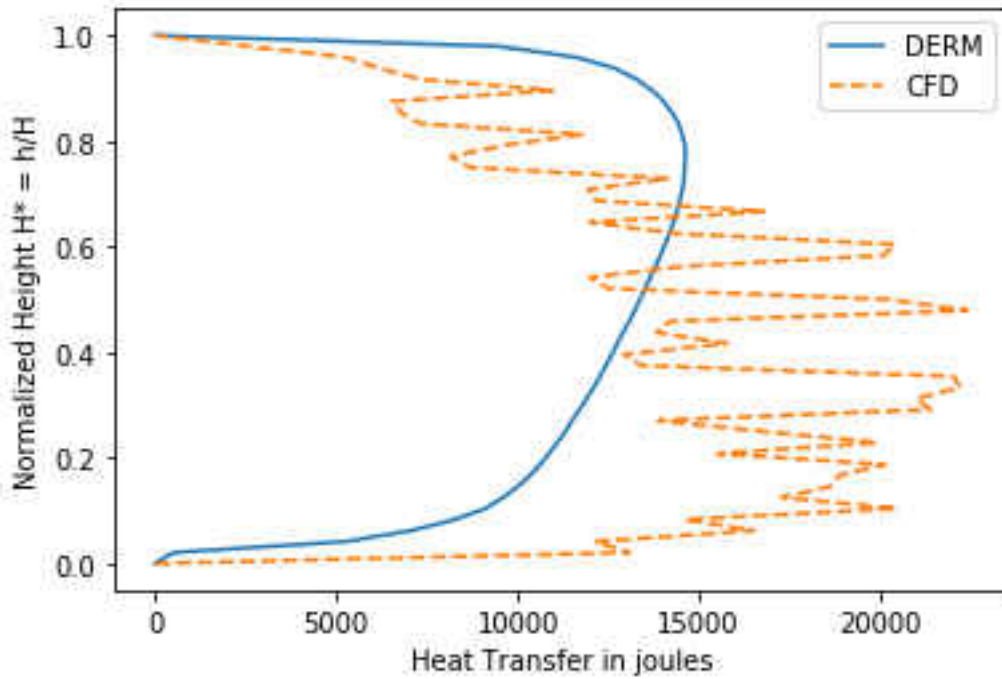
Figure 5.9: Hemisphere Evaluation of CFD and DERM Heat Transfer: Case 5.

With both of these elements, DERM is unable to capture the correct physics regardless of the the modeling use and opting for best case. Take into account the Nusselt Number, a dimensionless number that quantifies the ratio between convective and conductive heat transfer at a fluid/solid boundary.
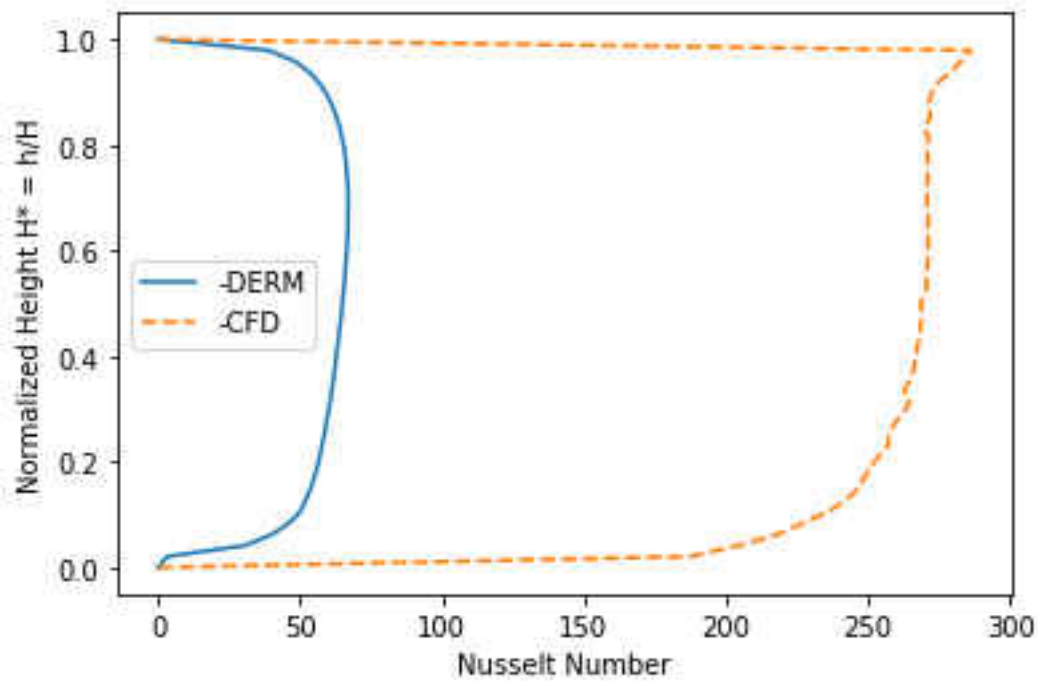
Figure 5.10: Hemisphere Nusslet Number Comparison: Case 5.

Generally, a Nusselt Number between 100-100 signifies a turbulent flow driven convection and laminar if below said range. Fig. 5.10 shows the comparison between the Nusselt Numbers. DERM in this case, is essentially simplifying the flow as laminar when it fact it turbulent. The a value given from the CFD are reasonable and suggest a turbulent flow. Even with a steady RANS model, the temperature boundary layer better seen in Fig. 5.8, suggest a separation of flow with circulation. Thus, even if the model is producing the correct physics, DERM is unable to compute it as it should.

5.2 URANS

In standard CFD, an unsteady-RANS model is deem inappropriate to model flow fields with large turbulence and developing eddies. Due to its averaging methods, a bulk of eddies that should be resolved are averaged away. During the validation portion of this thesis, URANS has proven to have decent accuracy for both cone and hemisphere when resolving for skin-drag. As such what follows is an analysis of the of its capabilities in comparison to DERM.

Five cases were developed but instead of reviewing each one individually, only the second case will be inspected followed by a compilation of all the other elements.
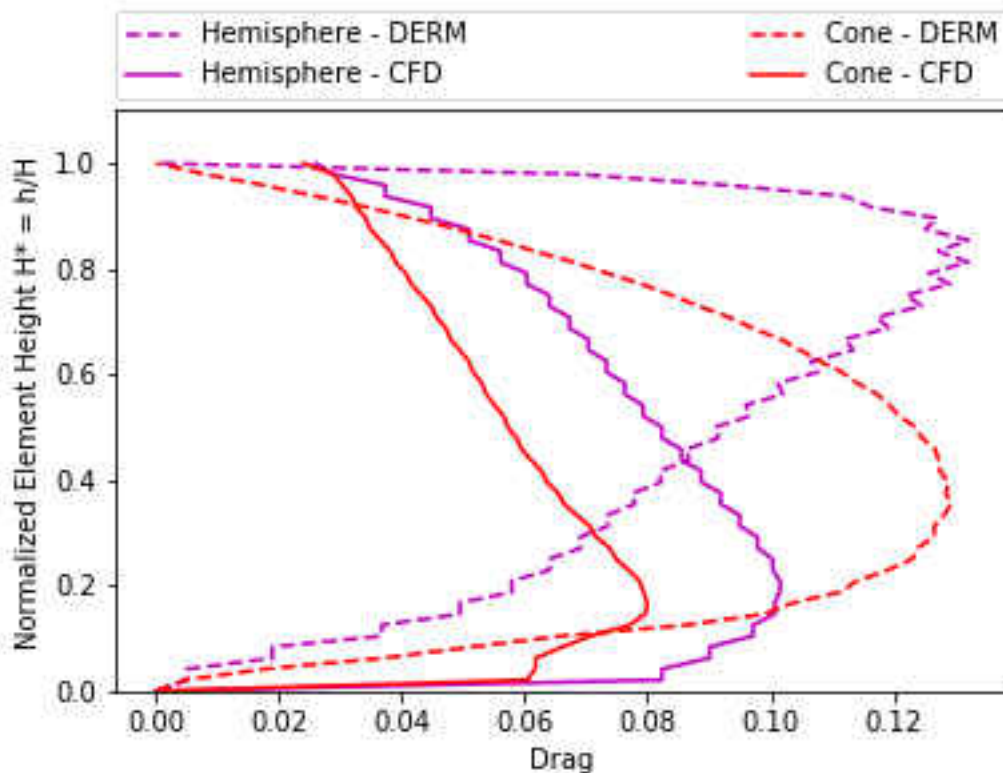
Figure 5.11: DERM and CFD Comparison: URANS Model Case 2.

Fig. 5.11 shows case 2 being the comparison of only the cone and hemisphere measuring the CFD drag and DERM drag. Interestingly just as before, the cone and hemisphere are following a very similar trend with the only difference being magnitude. In terms of significant changes from previous comparisons, no real significant changes has occur. There are however, some consistent trends. Such as no matter the case, the hemisphere DERM prediction is skewed towards its maximum height. At the same height also marks near one of the lowest points of the CFD drag. Meaning at that area, significant drag losses were estimated by the CFD but DERM was not capable, and rather estimated its maximum to be at that spot.
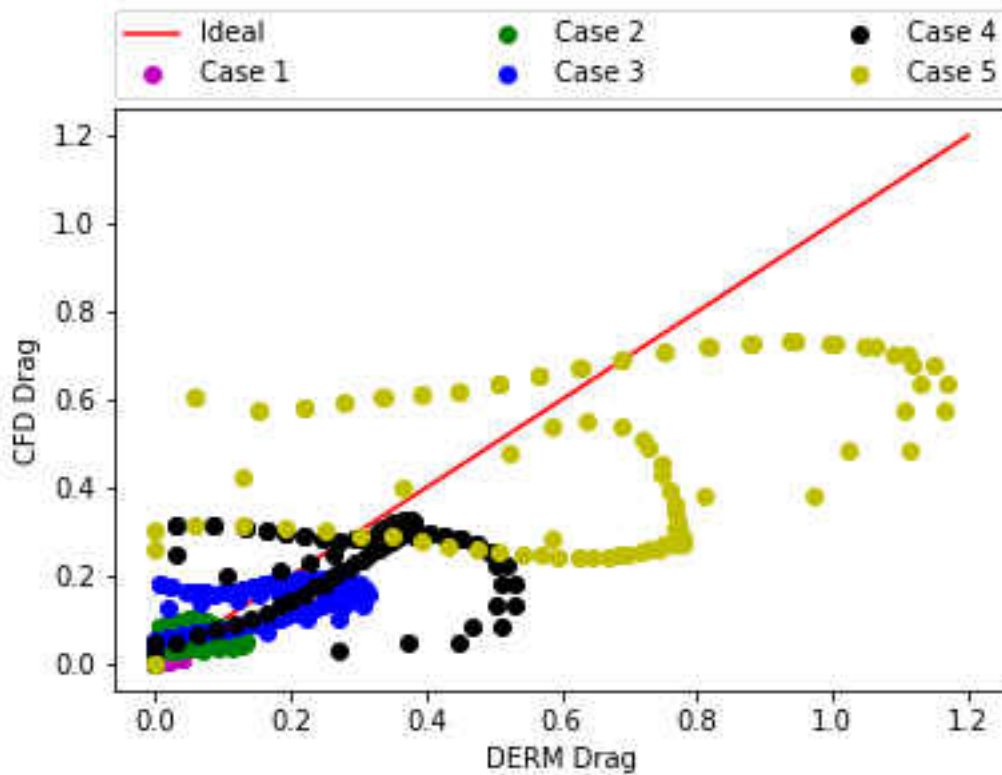
Figure 5.12: Parody Plot of Drag: URANS Model.

Inspecting Fig. 5.11 we are able to see all five cases with no distinction between elements. As

before all other cases in the RANS model, the URANS similarly predicts ideal scenarios for cases 1-3, with case 4 being the moment it diverges and case 5 finally swinging back and forth between DERM drag and CFD drag.

5.2 LES

The hybrid modeling is expected to be better in comparison to the previous modeling used. From the deviations seen from the past models, it appears these discrepancies stem from more than the type of model used. In this case we will be able to credit our theory more closely if the results suggest that DERM is more a function of geometry than viscous factors.

In this section we will be analyzing cases 3 and 4 for both the cone and hemisphere. The use of a parody plot will be omitted as previous cases have followed a pattern that may be extrapolated from the midway of high and low velocity cases, hence case 3 and 4.

Consider the plots below, Fig. 5.13 and Fig. 5.14, where they represent cases 3 and 4, respectively. Similar to previous cases, the cone element has the more accurate DERM prediction to its CFD counterpart. Interestingly, case 3 is opposite of its URANS model, where the CFD predicts higher than DERM. However, when comparing cases 3 and 4, other than the cone the hemisphere has no real indication of a trend between DERM and CFD. While the peaks may be near equivalent, they are suggested at opposite ends of the height. Rather the DERM appears to maintain shape but merely grow in magnitude as previous models and cases have indicated as well.
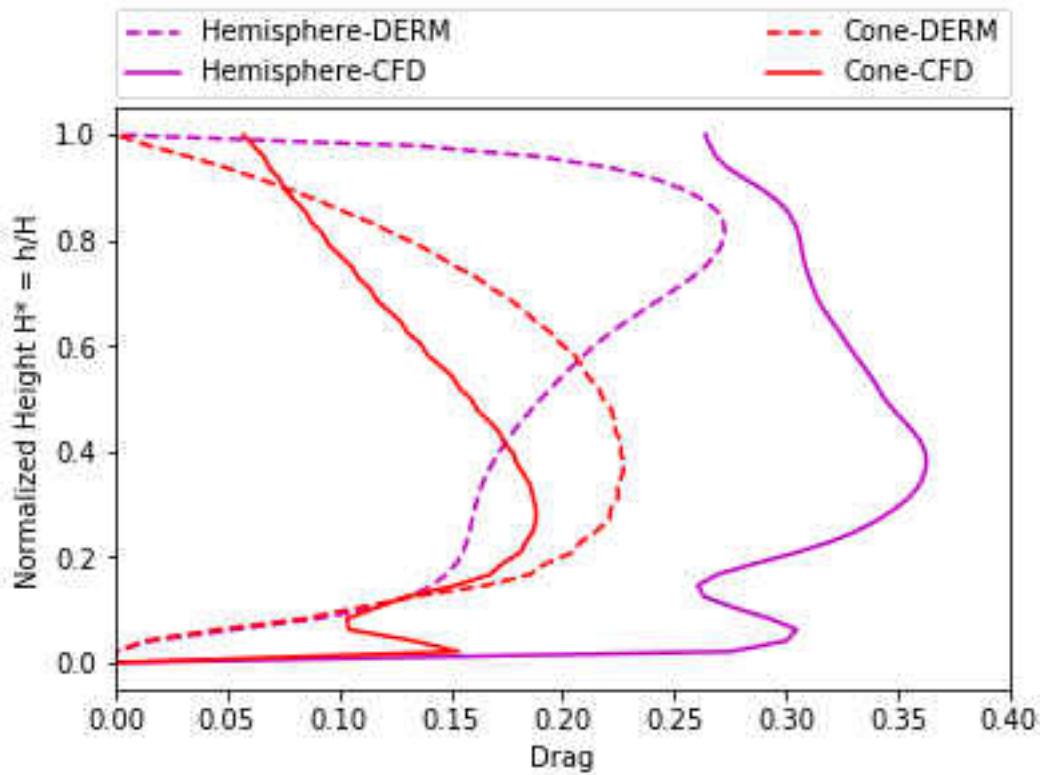
Figure 5.13: DERM and CFD Comparison: LES Model Case 3.

The cone element appears to be more precise at these cases and model than at any other. Other than its magnitude value, the cone appears to maintain symmetry and trend between cases without much of a difference and relatively cross paths at the exact same heights. More so, they tend to deviate at about the same heights as well proving they are producing near equivalent separation, drag, and other viscous-related parameters. Other than sphere element from the LES pressure-drop cases, this cone element appears to produce the most closely aligned comparison between DERM and CFD results.
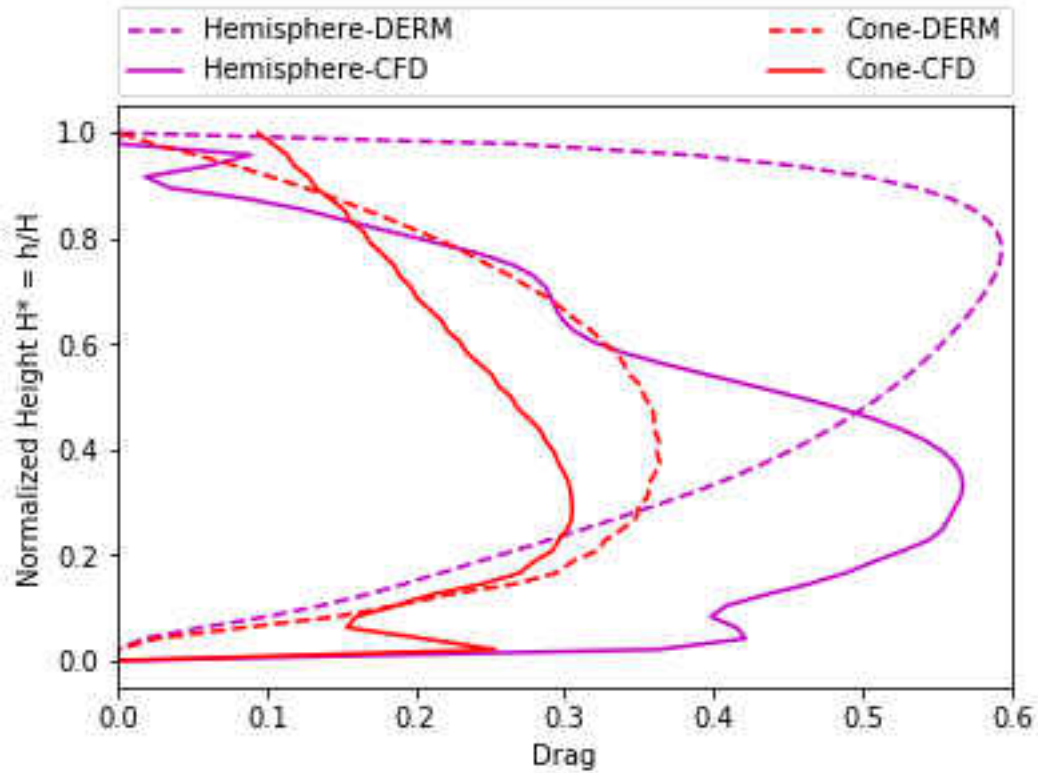
Figure 5.14: DERM and CFD Comparison: LES Model Case 4.

The hemisphere case adds credit to the idea of DERM being more geometric-eccentric than viscous flow determined. The CFD completely reconfigure its shape with near zero drag at the top of the element in case 4. However, the complete distinction of the hemisphere between cases show that the velocity profiles which affect the drag computed did not translate to the DERM. Rather, DERM as done so before, merely increased drag but relatively maintained shape. This indicates velocity can merely be interpreted as a scale factor for DERM. The cone on the other hand, suggests there are comparable parameters between the CFD and DERM and rather need only to be adjusted in order to better fit the CFD.

5.3 Model Enhancement

Suppose we develop a new drag model taking into account geometric approximation for ease (just like the DERM) and equivalently raise its viscous parameters through constants. A model such as this is known as the Wen-Yu drag model [54].

The drag force model offered by Wen-Yu is similar to that of drag effort term provided within DERM source terms. Wen-Yu takes a particle approach toward approximating drag by replacing the the object with mono-size spherical particles, similar to DERM's cylindrical approach. Additionally, Wen-Yu implements a void fraction method to solve for drag which opens the possibility of being coupled with DERM. Wen-Yu drag can then be described as the following:

$$F_{WY}^D = (1 + 0.15Re^{*0.687})\alpha_f^{-3.65} \tag{5.1}$$

Where α is the void fraction equivalent to β in context to DERM, and Re^* is the DERM's Reynolds number multiplied by the void fraction (α or β). In order to enhance its modeling capabilities we replace the coefficients with variables C_1, C_2, and C_3, replacing Eq. 5.1 with Eq. 5.2.

$$F_{WYE}^D = (1 + C_1 Re^{*C_2})\alpha_f^{C_3}\Delta y \tag{5.2}$$

Where Δy is the length scale parameter described in section (3.4.2). In this case we will taking the cone element measured in the LES modeling cases 3 and 4, to adjust if possible, a best fit to the CFD in comparison to DERM. Two approaches are taken; in scenario one we will be taking into account coefficients independent of case (velocity profiles) so as to best fit both cases and, in scenario two, the coefficients will be of best fit for each individual case.

Table 5.1: Cone Coefficients for Eq. 5.2

Scenario	C_1	C_2	C_3
1	0.4172	0.5360	-0.9971
2 (Case 3)	0.0361	0.8355	1.7789
2 (Case 4)	0.3060	0.5766	-0.3876

Tab. 5.1 shows the coefficients resolved for through an Excel non-linear solution. These coefficients are derived based on the assumptions built from this thesis. Such as being the end tips, subsurface and near the maximum height, being unable to adapt to the CFD. As such the top and bottom 10% of the height are omitted from the calculations of this study.
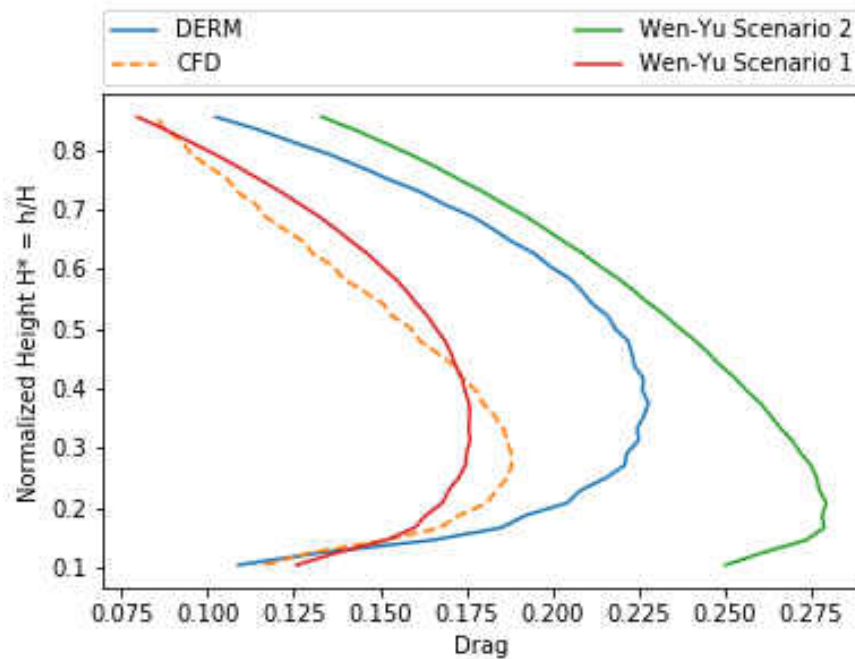
Figure 5.15: Comparison to Wen-Yu Enhancement: Case 3.

Fig. 5.15 illustrates the comparison of an enhanced Wen-Yu via the two methods. With the individualization per case method of scenario 2, the updated coefficients allow for the close approximation of the CFD. From this close inspection we see DERM is off and clearly has room for improvement in comparison to the Wen-Yu model. Scenario 2, which is an ideal scenario encapsulating all cases (3 and 4) does worst than DERM. This disagreement can further be explained by Fig. 5.16 showing the values for case 4.
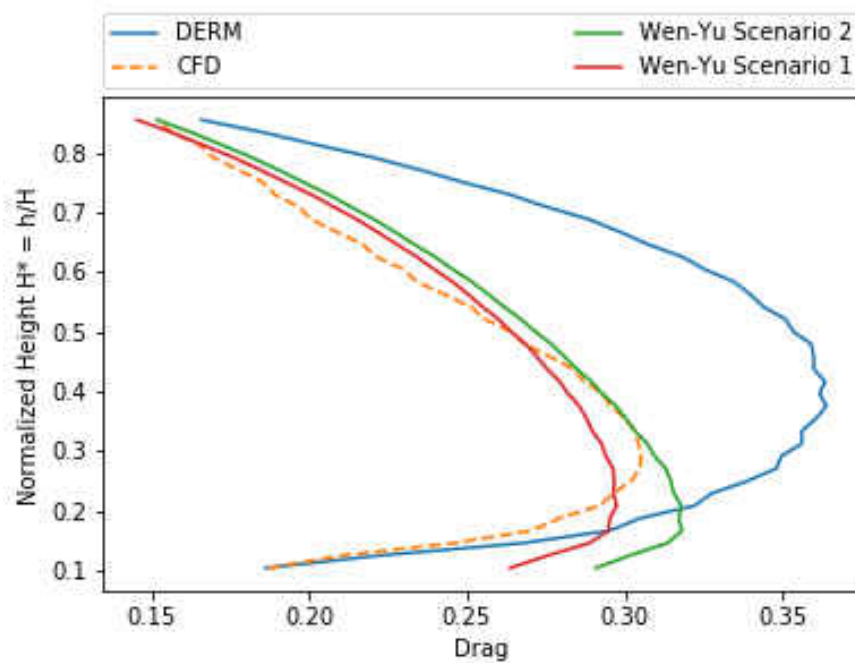
Figure 5.16: Comparison to Wen-Yu Enhancement: Case 4.

Similarly to case 3, scenario 1 nearly captures the CFD and does a better approximation than DERM. In this case however, scenario 1 is able to capture the CFD just as well as scenario 2. However, it is not applicable towards case 3 as previously shown meaning that in this enhancement, will favor one case(s) over others. This could be due to the methodology chosen and other methods may refine these results even further. Nevertheless, DERM is open to considerable improvement.

CHAPTER 6: CASE DIFFERENTIAL & MODELING COMPARISON

6.1 LES vs RANS

This section is dedicated towards inspecting the difference in modeling schemes. This thesis is comprised of two different types of cases. In order to maintain consistency, only the free-stream cases will be studied as it contains more modeling cases than the pressure drop. Of the free-stream cases only case 4 will be inspected. There are considerable differences that can be seen in previous sections between the CFD and DERM modeling scenarios. This section is meant to explore the differences in CFD modeling which influence DERM evaluation. We will explore the major differences in modeling being the velocity in the x-direction (streamwise), total pressure, Q-criterion and its effects to Reynolds number and coefficient of drag.

Fig. 6.1 is constructed to show the comparison in profiles and values of pressure and velocity between the RANS model (top) and the URANS model (bottom) for the hemisphere. Both capture the profiles qualitatively with the formation of eddies behind the element. The circulation at the front of the element is the key distinction between the two. The URANS model appears to have completely averaged out the eddy forming in the front that the RANS model has predicted. When comparing to the drag measured in earlier section, it is now clear why there was a sudden shift in drag prediction between the two models. Furthermore the magnitude of the velocity is also worth point out that the eddie in the RANS model is circulating at slower rates than then URANS model. An interesting aspect of these profiles is the total pressure in terms of value. While both models presented contain case 4, the total pressure are completely different. The magnitude of the URANS measure total pressure is over predicting by a factor of 10. It is possible the RANS could be wrong, and URANS is merely fixing the the valuation with more precise values. This can be further evaluated an explained with the LES comparison.
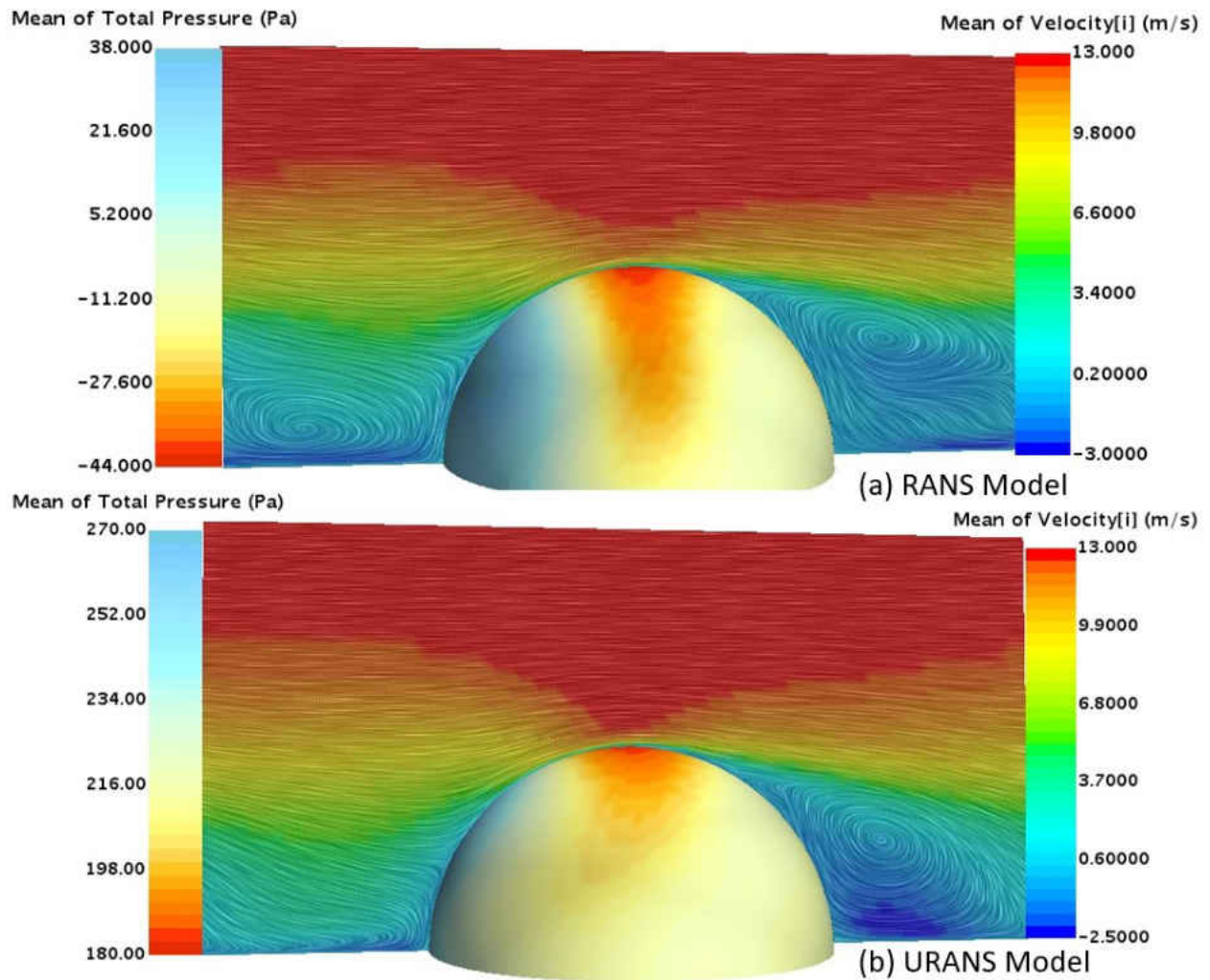
Figure 6.1: Hemisphere Model Comparison

Thus, in order to justify which model was more accurate Fig. 6.2 was developed. In terms of velocity we see multiple eddies forming in the front of the element with overall values closer to RANS than to URANS. It can be assumed that due to URANS inability to solve for circulation in large turbulence, it averaged-out what was suppose to resolve for due to the unsteady scheme. The RANS model however, because it was steady state it allowed for the continuation of circulation in order to reach a convergence point. In terms of total pressure, it indicates the RANS model was

more accurate than the URANS model in terms of profile and scalar value. It is now with reason
we can assume that the URANS would not be a valid modeling method to couple with DERM.
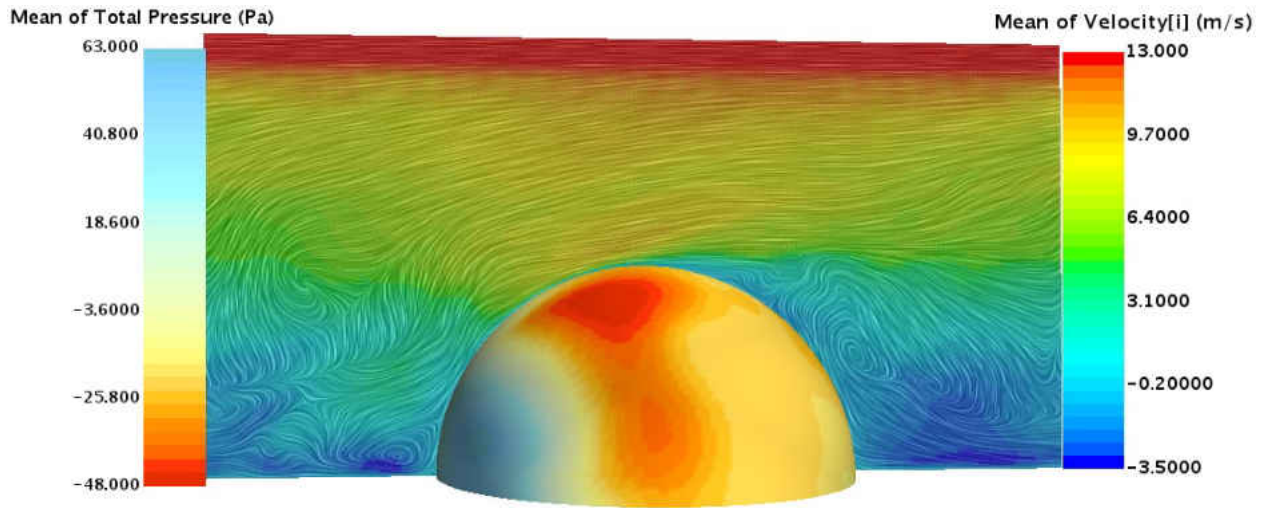
Figure 6.2: Hemisphere LES Model

In order to see its effects to DERMs evaluation method we further compare the Reynolds number
and drag coefficient resolved by DERM through Fig. 6.3. The Reynolds number and coefficient
of drag are both normalized based on the subsurface evaluated values(i.e Re = C_d = 1 bottom of
element). Here we compare only the RANS values to the LES. At first we see an equivalent trend
with both predicting equal values. Upon closer inspection the magnitude of the LES predicted
Reynolds number its much higher than of the RANS. This can be related back to Fig. 6.2 where
there were predicted eddies not shown in Fig. 6.1. Nevertheless, Fig. 6.3 shows DERM is unable
to capture any real changes in velocity profiles and rather relies on an average which only increases
the magnitude of value.
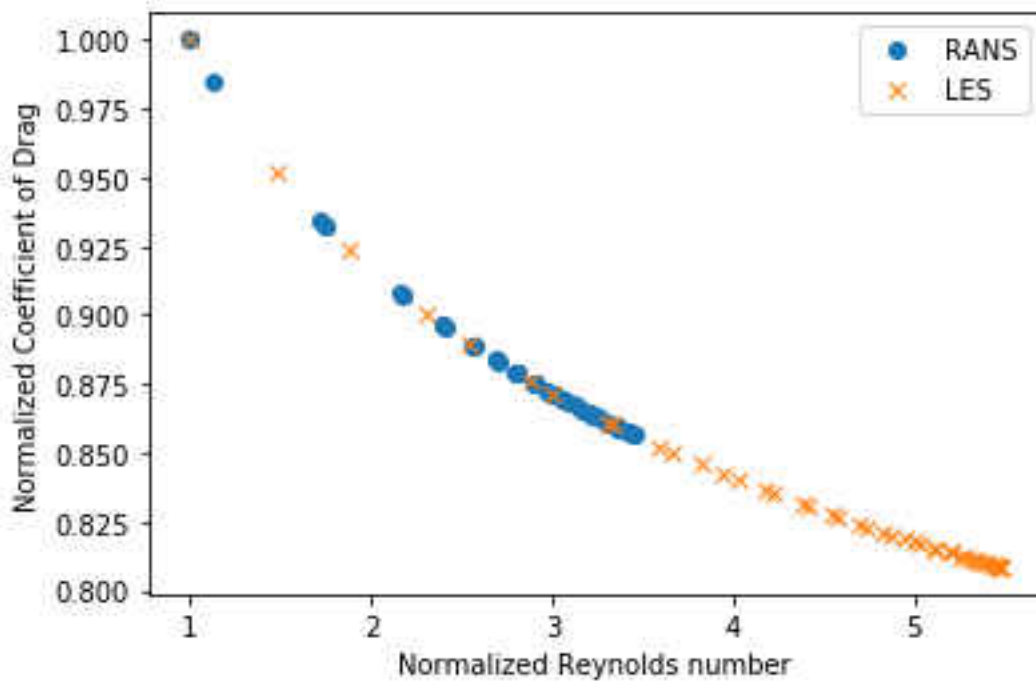
Figure 6.3: Hemisphere Comparison of Model DERM Evaluated Reynolds Number to *Cd*

For further comparison of model we rely on the cone element where only the RANS and LES models are compared. Through the measure of Q-criterion we are truly able to witness the difference in modeling capability. As a direct correlation of the shear-strain rate and vorticity, Q-criterion is able to quantify the magnitude of vorticity over the shear-strain rate. In Fig. 6.4, the RANS model predicts Q-criterion as large sets and clusters almost always connected. In comparison, the LES model measures each cluster individually while at much larger magnitudes. Through this we see the classic difference between the models, RANS averages the vorticity values that should be instead measured in each cell just as the LES has accomplished. Not taking into account the vast different velocity profiles, a product from the eddies due to turbulent flow inhibits DERMs ability to predict the drag accurately.
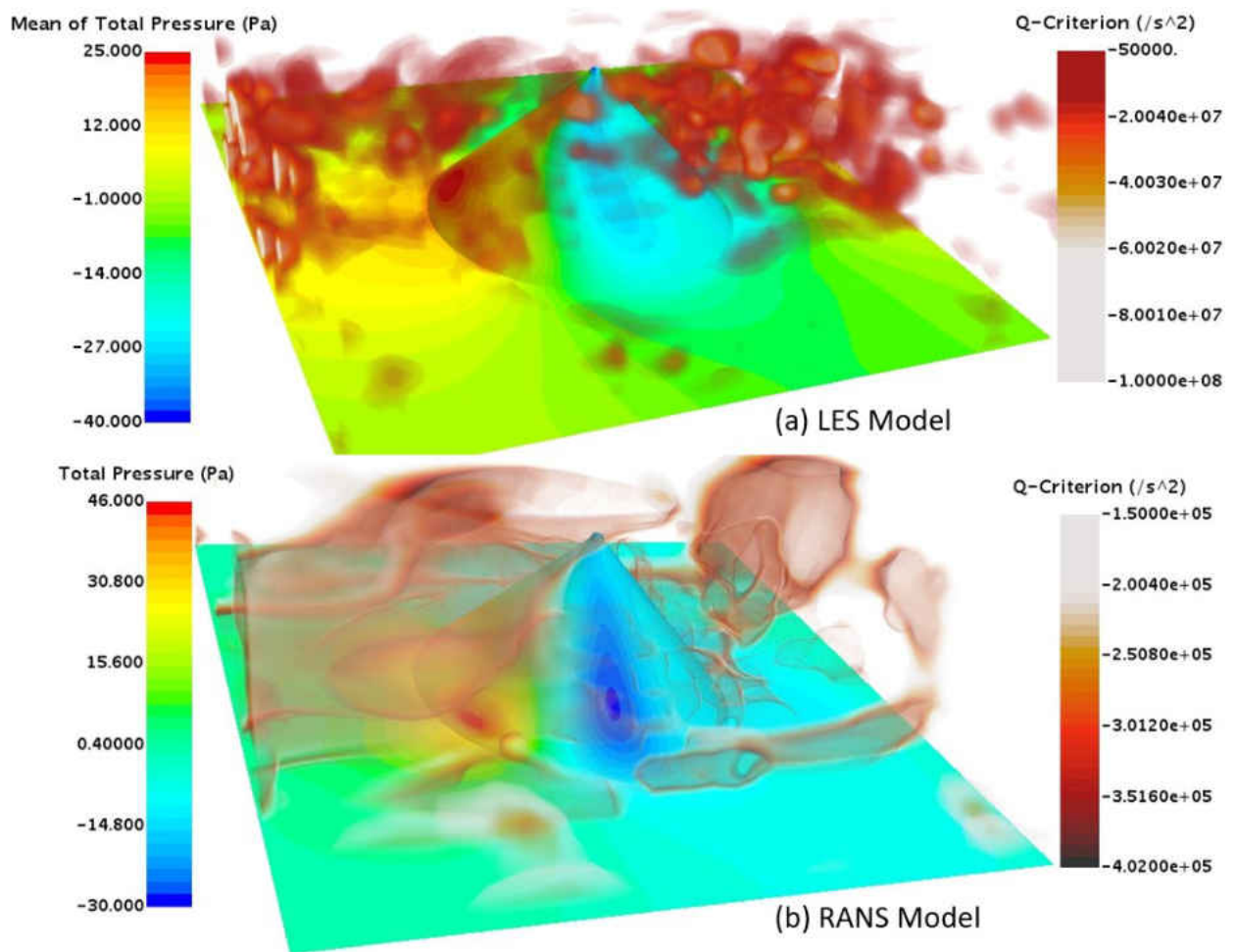
Figure 6.4: Cone Model Comparison

We then further rely on the similar comparison of Reynolds number and drag coefficient as previous done. Fig. 6.5 shows this comparison between models. As before the LES model predicts higher magnitudes of Reynolds number with corresponding higher coefficient of drag. Take into account the highest coefficient of drag does not exist at the base, rather LES and RANS both predict near the tip. This can be influenced from the tip creating large separation which increases drag. However as noted before, the development of velocity at those heights are vastly different from model to model and Fig. 6.5 shows near equal comparison. Suggesting DERM is merely taking into account the

90

shape, scaling the drag and velocity.
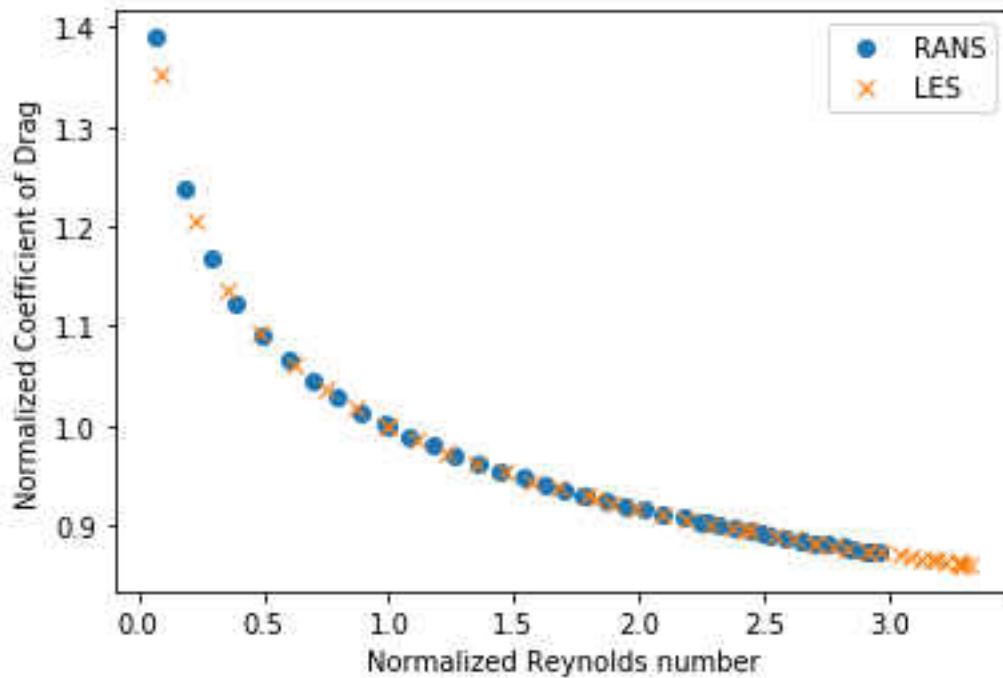
Figure 6.5: Cone Comparison of Model DERM Evaluated Reynolds Number to *Cd*

As such, we consider Fig. 6.6 as a last comparison of modeling technique. Here we clearly differentiate the models performance. The model prediction look nearly symmetrical opposites of one another splitting at the cones half-way height. This plot shows the difference in velocity relation to its corresponding height. Even though LES was more accurate in terms of eddy development, RANS did show ability to capture some eddy development. This insight begs the question, as to why DERM appears to resolve for Reynolds number and complete opposite values.
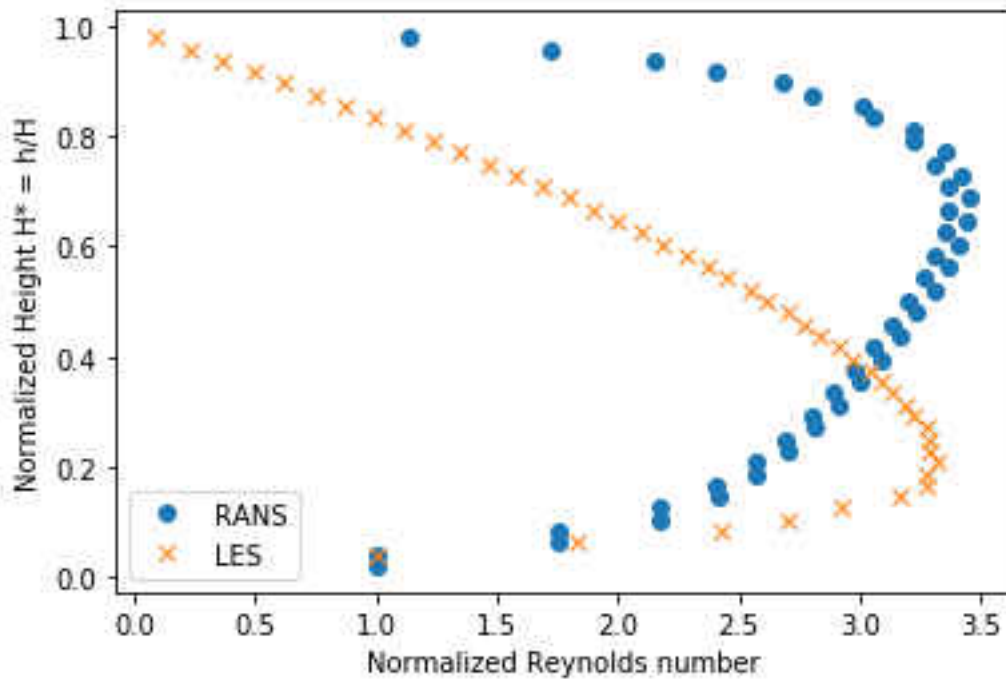
Figure 6.6: Cone Comparison of Model Reynolds Number to Height

6.2 Free Stream vs Pressure Drop

As a brief analysis, the free stream conditioned by a mass flow will be compared to the pressure drop. For simplicity and brevity, only the cone element will be analyzed. In this analysis the case 4 of the mass flow will compared to case 3 of the pressure drop as they both intend to maintain a free stream velocity of approximately 10 m/s. In order to maintain consistency the RANS models will be compared to one another, and then LES will compared separately.
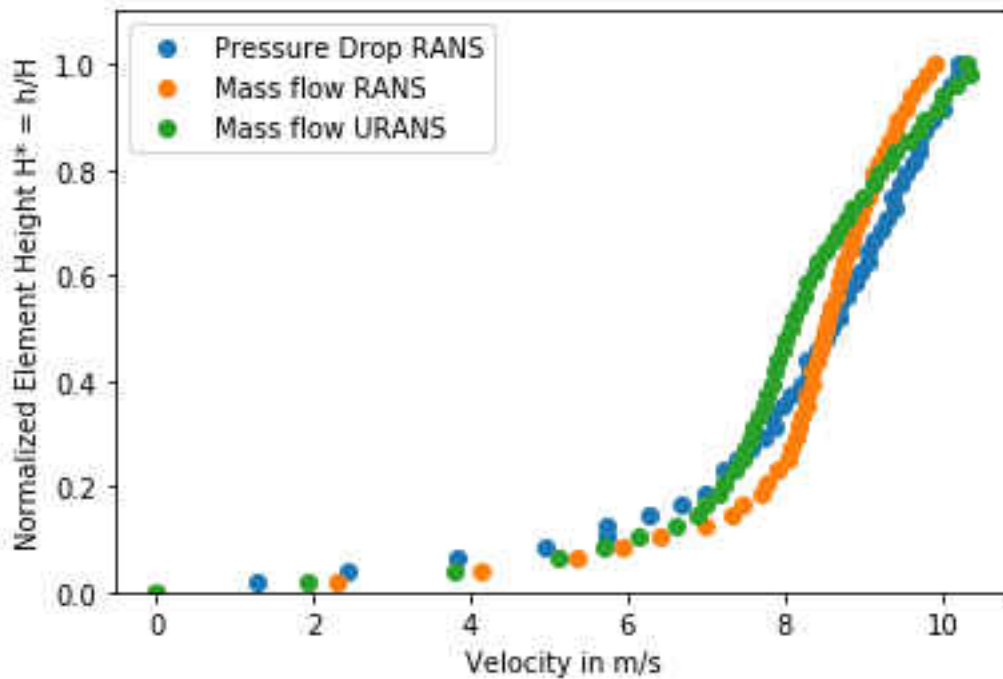
Figure 6.7: Comparison of CFD Measured Velocities for Cone Element.

If we first inspect velocity as provided by Fig. 6.7 we are able to see there are some slight differences between all of them. The mass flow conditioned had higher velocities from the bottom but eventually the pressure drop over takes both. From this we should expect for higher predicted drag from the mass flow CFD and DERM for the first quarter of the way up with eventually the pressure drop model to reach higher drag predicted values.
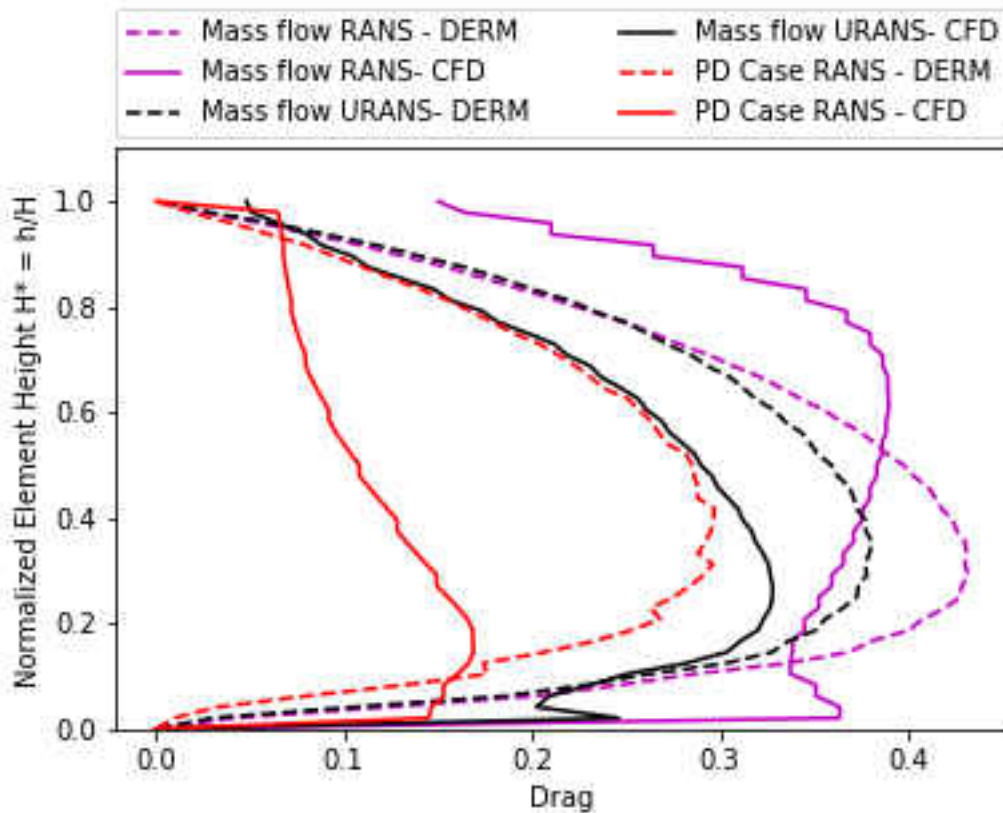
Figure 6.8: Comparison of Drag Between Models for Cone Element.

Fig. 6.8 allows to see if our theory is proven correct. This theory is based on the assumption that the velocity profiles are the main driver towards predicting drag accurately for DERM. Upon inspecting the plot we appear to be correct on the first quarter theory, however, the pressure drop case in both DERM and CFD predicts a lower drag at all heights. This could suggest that while the velocities were relatively similar, it was not the main driver for DERM as it should have eventually predicted higher drag values.

94

CHAPTER 7: CONCLUSION AND FUTURE WORK

Additive manufacturing has revolutionize the engineering industry, capable of handling complex jobs with ease. Industries such as the aerospace industry has taken advantage of additive manufacturing efficiency to produce parts such as fuel injectors and turbine blades. The surface roughness often produced from this type of manufacturing does not always lead to favorable results, as it can disturb heat transfer and fluid dynamic computations that assume for a flat surface. Thus being capable of correctly identifying these roughness features and solving for its corresponding physics becomes crucial towards the advancement of this technology.

In this work, a means of resolving for surface roughness drag and heat transfer is identified. The DERM model has previosly been used and validated as an accurate method of approximating roughness and its enhanced heat transfer. The correlations provided by DERM as a means of evaluating convective heat transfer by simplifying complex surface roughness rely on other underlying correlations of which are then studied. These underlying correlations are then what allow a real complex roughness approximation to simplified array of known geometrical elements. While the main DERM equations have been validated, its use of the underlying assumptions in form of effort terms are in need of inspection for discrepancies. The use of the CFD is implemented at resolving for these effort terms. These effort terms are then subjected to various cases for evaluation. Four different roughness elements are taken to be resolved with a RANS and LES (DES) model. These four elements were place under three different pressure drops allowing for the creation of cases. In total twenty-four cases were created from the pressure drop condition. Further more thirty more cases, known as free stream cases, were created utilizing Mart's data for validation with a RANS, URANS, and LES model. The CFD directly resolves for drag and heat transfer in each element and compared to the drag and heat transfer predicted by the effort terms provided by DERM. The momentum term shown by Eq. 2.2 was this papers primary focus at realizing a discrepancy be-

tween the term and the CFD reported values. Due to DERMs assumption of discrete cylindrical cells used as a replacement of the real surface roughness, it was hypothesize the correlations would become less accurate with high errors as you travel from the bottom of the roughness element to the top. Determining and understanding these discrepancies and how they came to be, allows for the improvement of DERM and a broader application. From this study we conclusively learned a number of issues with the DERM model and they are as follows:

In each case and model, DERM had difficulty being able to predict a drag around the maximum height. At the tip of each element, a wing tip effect is created where drag may increase depending on induced drag from vorticity development. DERM was unable to predict such a development due to the need for a "blockage" or non-unity void fraction in order to solve for drag.

While with model refinement the the CFD predicted drag was more accurate, however it does not necessarily translate well for DERM. Regardless of the accuracy in the velocity field, the only relation from CFD to DERM, the effort term still kept diverging at at higher velocities. The study preformed in section 6.2 further suggests velocity is not as a significant factor within DERM as others. This essentially signifies that as you approach the tip of any element, DERM can no longer accurately approximate the element through its cylindrical stacking. Regardless of the element tip, the other cases studied suggest geometric factors have a higher influence than the velocity fields. Thus if we make the assumption that a complex model, such as the LES model, is able to provide correct velocity profiles and as a result DERM still diverges indiscriminately, then we can assume that the other components of DERM such as its geometric factors, has a higher influence than that of the velocity. Therefore, because of the crude cylindrical geometric approximation it diverges by regardless of viscous factors involved and is purely geometric dependent.

DERM was applied to a refinement by comparing it to a spherical-approximation model, Wen-Yu. Through the use of coefficients we were able to improve the Wen-Yu capability of capturing CFD

showing room for improvement in DERM. We must, however, consider DERM holds the advantage of its ease in CFD application through its source term relation. This source term could then be adapted by some modification of DERM with a Wen-Yu like-model. Both consider relations in terms of void fraction which is one the reasons DERM is able to be implemented to a CFD without added steps. It would then be ideal to create the coefficients that would be geometric and non-dimensional viscous measurement related (Re, C_d, Nusselt number, etc.).

In the context of future work, it is possible that by providing a full implementation of LES (including the boundary-layer) in the domain, the results may be refined. As such, a study conducting these case studies at a true LES model might return better results.

Additionally, this study only provided a steady state model for the heat transfer effort term. It was found the heat transfer effort term did not capture an accurate depiction of the flow. This effort term would deviate not only because of its geometric evaluation, but also its approximation of Reynolds's number to Nusselt number which severely affected its ability to match the CFD prediction. However, this was only a steady case and errors such these were expected. A full case study as one conducted of drag through this thesis would give more insight to the discrepancies caused by the heat transfer effort term and narrow downs its defectiveness.

In terms of improving the model, Wen-Yu is an initial approach but is far from perfect. More importantly, all models regardless of case and time-scheme showed an inability to capture the end tip effects. Therefore, a focus on modeling such scenarios separately then coupling it with DERM would improved the model capabilities by far that thus far has not achieved..

APPENDIX A: DERIVATION OF DERM

A flow moving through a static control volume Ω that contains a porous medium defined by β. Generically written mass conservation porous medium is written as:

$$\iiint_\Omega \frac{\partial}{\partial t}(\rho\beta)dV + \iint_{\partial\Omega} \rho u \cdot n\beta dS = 0 \tag{A.1}$$

Conservation equations may be simplified by defining as a function of ϕ as:

$$\iiint_\Omega \phi dC = \iiint_\Omega \beta\phi dV \tag{A.2}$$

$$\iint_{\partial\Omega} \phi dS = \iint_{\partial\Omega} \beta\phi dS \tag{A.3}$$

For a Newtonian fluid the conservation of momentum is generally written as:

$$\iiint_\Omega \frac{\partial}{\partial t}(\rho u)dV + \iint_{\partial\Omega} (\rho(u \otimes u) + P\iota - \tau) \cdot ndS = 0 \tag{A.4}$$

and energy is written as:

$$\iiint_\Omega \frac{\partial}{\partial t}(\rho(e + \frac{1}{2}(u \cdot u)))dV + \iint_{\partial\Omega} (\rho(e + \frac{1}{2}(u \cdot u))u - \tau u + Pu + q) \cdot ndS = 0 \tag{A.5}$$

Applying the divergence theorem for simplification all three conservation equations become:

$$\frac{\partial\rho}{\partial t} + \nabla \cdot (\rho u) = 0 \tag{A.6}$$

$$\frac{\partial}{\partial t}(\rho u) + \nabla \cdot (\rho (u \otimes u) + P\iota - \tau) = 0 \tag{A.7}$$

$$\frac{\partial}{\partial t}(\rho (e + \frac{1}{2}(u \cdot u))) + \nabla \cdot (\rho (e + \frac{1}{2}(u \cdot u))u - \tau u + Pu + q) = 0 \tag{A.8}$$

Each representing the mass, momentum, and energy equations respectively.

By assuming a cartesian coordinate system along with a Spatial Favre-averaging the equations are modified even further turning into:

Mass:

$$\frac{\partial \beta(\rho)^f}{\partial f} + \nabla \cdot (\beta \rho^f \hat{u}) = 0 \tag{A.9}$$

Momentum:

$$\frac{\partial}{\partial t}(\beta \rho^f \hat{u}_i) + \frac{\partial}{\partial x_j}(\beta \rho^f \hat{u}_i \hat{u}_j + \beta(\overline{\rho u_i'' u_j''})^f + \beta \overline{P}^f \delta_{ij} - 2\hat{v}(\beta \overline{\rho}^f \frac{\partial \hat{u}_i}{\partial x_j} +$$
$$\beta \overline{\rho}^f \frac{\partial \hat{u}_j}{\partial x_i}) + \frac{2}{3}\hat{v}\beta \overline{\rho}^f \frac{\partial \hat{u}_k}{\partial x_k}\delta_{ij}) + \frac{\partial}{\partial x_j}(\beta(\overline{\rho}\hat{u}_i^* \hat{u}_j^*)^f - \hat{\tau}_{ij}) + \tag{A.10}$$
$$\frac{\beta}{vol(\Omega_f)} \iint_{\partial \Omega} (\hat{P}\delta_{ij} + \frac{2}{3}\delta_{ij}\frac{\partial \hat{u}_k}{\partial x_k} - 2\hat{\mu}\hat{S}_{ij})n_j dA = 0$$

Energy:

$$\frac{\partial}{\partial t}(\beta\overline{\rho}^f\hat{e}_o) + \frac{\partial}{\partial x_j}(\beta\overline{\rho}^f\hat{h}\hat{u}_j + \frac{1}{2}\beta(\overline{\rho u_i'' u_j''})^f + \beta(\overline{\rho h'' u_j''})^f + \beta(\overline{\rho u_i'' u_j''})^f\hat{u}_i -$$

$$2\hat{v}(\beta\overline{\rho}^f(\hat{u}_i)\frac{\partial\hat{u}_i}{\partial x_j} + \beta\overline{\rho}^f(\hat{u}_i)\frac{\partial\hat{u}_j}{\partial x_i}) + \frac{2}{3}\hat{v}\beta\overline{\rho}^f(\hat{u}_j)\frac{\partial\hat{u}_k}{\partial x_k} - \beta(\overline{\tau_{ij}u_i''})^f + \beta(\hat{P}\overline{u}_j'')^f -$$

$$\frac{C_p\mu}{Pr}\beta(\frac{\partial T}{\partial x_j})^f - \frac{C_p\mu}{Pr}\beta(\frac{\partial T''}{\partial x_j})^f) + \frac{\partial}{\partial x_j}(\beta(\overline{\rho}\hat{u}_j^*\hat{e}^*)^f + \frac{1}{2}\beta(\overline{\rho}\hat{u}_i^*\hat{u}_i^*\hat{u}_j^*)^f + \beta\hat{u}_i(\hat{u}_j^*\hat{u}_i^*)^f + \quad \text{(A.11)}$$

$$\frac{1}{2}\beta(\overline{\rho}\hat{u}_i''\hat{u}_i''\hat{u}_j^*)^f + \beta(\overline{\rho}\hat{u}_i''\hat{u}_j''\hat{u}_i^*)^f + \hat{v}(\beta(\overline{\rho}\hat{u}_i^*\frac{\partial\hat{u}_i}{\partial x_j})^f + \beta(\overline{\rho}\hat{u}_i^*\frac{\partial\hat{u}_j}{\partial x_i})^f) + \frac{2}{3}\delta_{ij}\hat{v}\beta(\overline{\rho}\hat{u}_i^*\frac{\partial\hat{u}_k}{\partial x_k})^f +$$

$$\beta(\overline{P}\hat{u}_j^*)^f - \beta(\tau_{ij}\hat{u}_i^*)^f + \frac{\beta}{vol(\Omega_f)}\iint_{\partial\Omega}(k_f\frac{\partial T}{\partial x_j}))n_j dA = 0$$

Within Eqs. (A.11-A.12) exist spatial average terms that at present exists no way to account for them. Developing a turbulence capable of doing so is beyond the work of this paper. Therefore these terms are lumped in with the boundary terms in order to replace them with added drag and heat terms, f^p and f^q, respectively.

At this point the hats and stars signifying temporal and spatial averages will be suppressed along with being combined with the surface integrals to a single momentum and energy source terms each.

Conservation of Mass:

$$\beta\frac{\rho}{t}\frac{\partial\beta\rho u_i}{\partial x_i} = 0 \tag{A.12}$$

Conservation of Momentum:

$$\frac{1}{\beta}f_i^p - \frac{1}{\beta}(\rho u_i u_j + P\delta_{ij} + \frac{2}{3}\rho k\delta_{ij} - 2(\mu+\mu_t)\delta_{ij} + \frac{2}{3}(\mu+\mu_t)\frac{\partial u_k}{\partial x_k}\delta_{ij})\frac{\partial\beta}{\partial x_j} = 0 \tag{A.13}$$

Conservation of Energy:

$$\frac{1}{\beta}f_i^p u_i + \frac{1}{\beta}f_i^q - \frac{1}{\beta}(\rho u_j h + (\mu + \frac{\mu}{\sigma_k})\frac{\partial k}{\partial x_j} - (\frac{c_p \mu}{Pr} + \frac{\mu_t c_p}{Pr_t})\frac{\partial T}{\partial x_j}$$
$$-2u_i(\mu + \mu_t)S_{ij} + \frac{2}{3}(\mu + \mu_t)u_j\frac{\partial u_k}{\partial x_k} + \frac{2}{3}u_j \rho k)\frac{\partial \beta}{\partial x_j} = 0 \tag{A.14}$$

Adding Eqs.(A.12-A.14) to the traditional mass, momentum, and energy conservation equations you arrived at Eqs.(2.1-2.3).

LIST OF REFERENCES

[1] N. Abuaf, R. S. Bunker, and C. P. Lee. "Effects of surface roughness on heat transfer and aerodynamic performance of turbine airfoils". In: *Proceedings of the ASME Turbo Expo* 3.July 1998 (1997). DOI: 10.1115/97-GT-010.

[2] Thomas Adams and Christopher Grant. "A Simple Algorithm to Relate Measured Surface Roughness to Equivalent Sand-grain Roughness". In: *International Journal of Mechanical Engineering and Mechatronics Volume* 1.1 (2012). DOI: 10.11159/ijmem.2012.008.

[3] Rezvan Adelnia et al. "Evaluation of Surface Finish Affect on Aerodynamic Coefficients Of Wind Tunnel Testing Models". In: 2006.

[4] A. Ahmadi Nadooshan, Saeed Daneshmand, and C. Aghanajafi. "Evaluation of Surface Finish Affect on Aerodynamic Coefficients of Wind Tunnel RP Models Production with ABSi Material". In: *Advanced Manufacture*. Vol. 594. Materials Science Forum. Trans Tech Publications Ltd, Nov. 2008, pp. 255–260. DOI: 10.4028/www.scientific.net/MSF.594.255.

[5] B Aupoix. "Modeling of Boundary Layer Flows Over Rough Surfaces". In: *Adv. Turbul. V, Springer* V (1995), pp. 16–20. DOI: 10.1007/978-94-011-0457-9_4.

[6] B Aupoix. "Revisiting the Discrete Element Method for Predictions of Flows Over Rough Surfaces". In: *Journal of Fluids Engineering ASME* 138.March (2016), pp. 1–9. DOI: 10.1115/1.4031558.

[7] Kevin Ayers. "https://www.sme.org/technologies/articles/2017/may/first-plastics-then-metals-and-now-composites/".

[8] Evelien van Bokhorst et al. "Feather roughness reduces flow separation during low Reynolds number glides of swifts". In: *Journal of Experimental Biology* 218.20 (2015), pp. 3179–

3191. ISSN: 0022-0949. DOI: 10.1242/jeb.121426. eprint: https://jeb.biologists.org/content/218/20/3179.full.pdf. URL: https://jeb.biologists.org/content/218/20/3179.

[9] S. Daneshmand, A. R. Dehghani, and C. Aghanajafi. "Investigation of Surface Roughness on Aerodynamics Properties". In: *Journal of Aircraft* 44.5 (2007), pp. 1630–1634. DOI: 10.2514/1.28030. eprint: https://doi.org/10.2514/1.28030. URL: https://doi.org/10.2514/1.28030.

[10] Brian Dean and Bharat Bhushan. "Shark-skin surfaces for fluid-drag reduction in turbulent flow: a review". In: *Philosophical Transactions of the Royal Society A: Mathematical, Physical and Engineering Sciences* 368.1929 (2010), pp. 4775–4806. DOI: 10.1098/rsta.2010.0201. eprint: https://royalsocietypublishing.org/doi/pdf/10.1098/rsta.2010.0201. URL: https://royalsocietypublishing.org/doi/abs/10.1098/rsta.2010.0201.

[11] Brian Dean and Bharat Bhushan. "Shark-skin surfaces for fluid-drag reduction in turbulent flow: a review". In: *Philosophical Transactions of the Royal Society A: Mathematical, Physical and Engineering Sciences* 368.1929 (2010), pp. 4775–4806. DOI: 10.1098/rsta.2010.0201.

[12] Jason C. Fox, Shawn P. Moylan, and Brandon M. Lane. "Effect of Process Parameters on the Surface Roughness of Overhanging Structures in Laser Powder Bed Fusion Additive Manufacturing". In: *Procedia CIRP* 45 (2016), pp. 131–134. ISSN: 22128271. DOI: 10.1016/j.procir.2016.02.347.

[13] C. R. Garcia et al. "Effects of extreme surface roughness on 3D printed horn antenna". In: *Electronics Letters* 49.12 (2013), pp. 734–736. ISSN: 00135194. DOI: 10.1049/el.2013.1528.

[14] User Guide. *STAR-CCM+*. Version 8.06. 2013.

[15] Jiang Guo et al. "Surface quality improvement of selective laser sintered polyamide 12 by precision grinding and magnetic field-assisted finishing". In: *Materials & Design* 138 (Oct. 2017). DOI: 10.1016/j.matdes.2017.10.048.

[16] David R. Hanson. "Computational Investigation of Convective Heat Transfer on Ice-Roughened Aerodynamic Surfaces". PhD thesis. Pennsylvania State University, 2017, p. 444.

[17] David R. Hanson and Michael P. Kinzel. "Evaluation of a subgrid-scale computational fluid dynamics model for ice roughness". In: *Journal of Aircraft* 56.2 (2019), pp. 787–799. ISSN: 00218669. DOI: 10.2514/1.C035060.

[18] David R. Hanson, Michael P. Kinzel, and Stephen T. McClain. "Validation of the discrete element roughness method for predicting heat transfer on rough surfaces". In: *International Journal of Heat and Mass Transfer* 136 (2019), pp. 1217–1232. ISSN: 00179310. DOI: 10.1016/j.ijheatmasstransfer.2019.03.062.

[19] David R. Hanson et al. "Computational heat transfer modeling of ice roughened airfoils". In: *46th AIAA Fluid Dynamics Conference* (2016), pp. 1–26. DOI: 10.2514/6.2016-4110.

[20] David R Hanson et al. "Flow in a Scaled Turbine Coolant Channel With Roughness Due To Additive Manufacturing". In: *Proceedings of ASME Turbo Expo 2019: Turbomachinery Technical Conference and Exposition* (2019), pp. 1–12. DOI: 10.1115/GT2019-90931.

[21] David Hanson and Michael Kinzel. "An Improved CFD Approach for Ice-Accretion Prediction Using The Discrete Element Roughness Method". In: *Proceedings of the ASME 2017 Fluids Engineering Division* (2017), pp. 1–10. DOI: 10.1115/FEDSM2017-69365.

[22] Linda Hernandez et al. "The Effect of Surface Roughness on LCH4 Boiling Heat Transfer Performance of Conventionally and Additively Manufactured Rocket Engine Regenerative Cooling Channels". In: Aug. 2019. DOI: 10.2514/6.2019-4363.

[23]   J. Jia et al. "Effect of wall roughness on performance of microchannel applied in microfluidic device". In: *Microsyst Technol* 25 (May 2019), pp. 2385–2397. DOI: doi.org/10.1007/s00542-018-4124-7.

[24]   Satish G. Kandlikar et al. "Characterization of surface roughness effects on pressure drop in single-phase flow in minichannels". In: *Physics of Fluids* 17.10 (2005). ISSN: 10706631. DOI: 10.1063/1.1896985.

[25]   Hakki Karakas, Emre Koyuncu, and Gokhan Inalhan. "ITU tailless UAV design". In: *Journal of Intelligent & Robotic Systems* 69 (Jan. 2013). DOI: 10.1007/s10846-012-9695-4.

[26]   Holger Krueger. "Standardization for Additive Manufacturing in Aerospace". In: *Engineering* 3 (Oct. 2017), p. 585. DOI: 10.1016/J.ENG.2017.05.010.

[27]   Nikhil Kumbhar and Arati Mulay. "Post Processing Methods used to Improve Surface Finish of Products which are Manufactured by Additive Manufacturing Technologies: A Review". In: *Journal of The Institution of Engineers (India): Series C* 99 (Aug. 2016). DOI: 10.1007/s40032-016-0340-z.

[28]   Amy Lang, Maria Laura Habegger, and Philip Motta. "Shark Skin Drag Reduction". In: *Encyclopedia of Nanotechnology*. Ed. by Bharat Bhushan. Dordrecht: Springer Netherlands, 2012, pp. 2394–2400. ISBN: 978-90-481-9751-4. DOI: 10.1007/978-90-481-9751-4_266. URL: https://doi.org/10.1007/978-90-481-9751-4_266.

[29]   M J Lewis. "An Elementary Analysis for Predicting the Momentum- and Heat Transfer Characteristics of a". In: *Journal of Heat Transfer ASME* (1975), pp. 249–254. DOI: 10.1115/1.3450349.

[30]   Zhuowei Li et al. "RANS AND LES SIMULATION OF A SWIRLING FLOW IN A COMBUSTION CHAMBER WITH DIFFERENT SWIRL INTENSITIES". In: *International*

Symposium on Advances in Computational Heat Transfer (July 2012), pp. 1–16. DOI: 10. 1615/ICHMT.2012.CHT-12.1030.

[31]   Michael MacDonald et al. "Heat transfer in rough-wall turbulent thermal convection in the ultimate regime". In: *Phys. Rev. Fluids* 4 (7 July 2019), p. 071501. DOI: 10.1103/ PhysRevFluids.4.071501. URL: https://link.aps.org/doi/10.1103/PhysRevFluids. 4.071501.

[32]   Arfan Majeed et al. "Surface quality improvement by parameters analysis, optimization and heat treatment of AlSi10Mg parts manufactured by SLM additive manufacturing". In: *International Journal of Lightweight Materials and Manufacture* 2.4 (2019). Research progress on subtractive and additive manufacturing, pp. 288–295. ISSN: 2588-8404. DOI: https: //doi.org/10.1016/j.ijlmm.2019.08.001. URL: http://www.sciencedirect. com/science/article/pii/S2588840419300708.

[33]   C Mangrulkar, J Abraham, and A. Dhoble. "Numerical studies on the near wall y + effect on heat and flow characteristics of the cross flow tube bank". In: *Journal of Physics: Conference Series* 1240 (July 2019), p. 012110. DOI: 10.1088/1742-6596/1240/1/012110.

[34]   Steven R. Mart. "The Effect of Roughness Element Thermal Conductivity on Turbulent Convection". PhD thesis. Baylor University, 2011, p. 128.

[35]   Stephen T Mcclain, B Keith Hodge, and Jeffrey P Bons. "Predicting Skin Friction and Heat Real Gas Turbine Surface". In: *Journal of Turbomachinery ASME* 126.April 2004 (2017), pp. 259–267. DOI: 10.1115/1.1740779.

[36]   Stephen Taylor Mcclain. "A DISCRETE-ELEMENT MODEL FOR TURBULENT FLOW OVER RANDOMLY-ROUGH SURFACES". PhD thesis. Mississippi State University, 2002, p. 193.

[37]   Elia Merzari and Hisashi Ninokata. "DEVELOPMENT OF AN LES METHODOLOGY FOR COMPLEX GEOMETRIES". In: *Nuclear Engineering and Technology* 41.7 (2009), pp. 893–906. DOI: 10.5516/NET.2009.41.7.893.

[38]   Alejandro Sebastián Ortiz-Pérez and Ildebrando Pérez-Reyes. "The linear hydrodynamic stability of a fluid in a cavity with finite thermal conductivity". In: *International Journal of Heat and Mass Transfer* 145 (2019), p. 118768. ISSN: 0017-9310. DOI: https://doi.org/10.1016/j.ijheatmasstransfer.2019.118768. URL: http://www.sciencedirect.com/science/article/pii/S001793101933621X.

[39]   Tanisha Pereira, John Kennedy, and J. Potgieter. "A comparison of traditional manufacturing vs additive manufacturing, the best method for the job". In: *Procedia Manufacturing* 30 (Jan. 2019), pp. 11–18. DOI: 10.1016/j.promfg.2019.02.003.

[40]   Sajjad Raeisi, Joel Najmon, and Andres Tovar. "Aerospace requirements and opportunities for additive manufacturing". In: Feb. 2019, pp. 7–33. ISBN: 0128140631.

[41]   Jing Ren. "Micro/nano scale surface roughness tailoring and its effect on microfluidic flow". PhD thesis. Iowa State University, 2013, p. 173.

[42]   Von H Schlichting and Friedrichshafen a. B. "Experimentelle untersuchungen zum rauhigkeitsproblem". In: *Arch. Appl. Mech* 7.I (1936), pp. 1–34. DOI: 10.1007/BF02084166.

[43]   M. Nicholas Schneider. "Exploration of the Effect of Surface Roughness on Heat Transfer in Microscale Liquid Flow". PhD thesis. Rochester Institute of Technology, 2010, p. 107.

[44]   A Schulz and S Wittig. "Surface Roughness Effects on External Heat Transfer of a HP". In: *Journal of Turbomachinery ASME* 127.January 2005 (2016). DOI: 10.1115/1.1811101.

[45]   P. SPALART and S. ALLMARAS. "A one-equation turbulence model for aerodynamic flows". In: *30th Aerospace Sciences Meeting and Exhibit* 1 (1992), pp. 5–21. DOI: 10.2514/6.1992-439.

[46]   Philippe R. Spalart. "Detached-Eddy Simulation". In: *Annual Review of Fluid Mechanics* 41.1 (2009), pp. 181–202. DOI: 10.1146/annurev.fluid.010908.165130. eprint: https://doi.org/10.1146/annurev.fluid.010908.165130. URL: https://doi.org/10.1146/annurev.fluid.010908.165130.

[47]   Jan-Eric Staahl, Fredrik Schultheiss, and Soren Hagglund. "Tolerance Cost in Relation to Surface Finish during Longitudinal Turning Operations". English. In: *Proceedings of the 6th Swedish Production Symposium*. The Swedish Production Academy, 2014.

[48]   Curtis Stimpson et al. "Roughness Effects on Flow and Heat Transfer for Additively Manufactured Channels". In: *Journal of Turbomachinery* 138 (Dec. 2015). DOI: 10.1115/1.4032167.

[49]   R P Taylor and H W Coleman. "Prediction of Turbulent Rough-Wall Skin Friction Using a Discrete Element Approach". In: *Journal of Fluids Engineering ASME* 107 (1985), p. 7. DOI: 10.1115/1.1524587.

[50]   R. P. Taylor. "A discrete element prediction approach for turbulent flow over rough surfaces". PhD thesis. Mississippi State Univ., State College, Jan. 1983.

[51]   Mark J. Tummers and Martin Steunebrink. "Effect of surface roughness on heat transfer in Rayleigh-Bénard convection". In: *International Journal of Heat and Mass Transfer* 139 (2019), pp. 1056–1064. ISSN: 0017-9310. DOI: https://doi.org/10.1016/j.ijheatmasstransfer.2019.05.066. URL: http://www.sciencedirect.com/science/article/pii/S0017931019300201.

[52]   Razvan Udroiu, Ion Cristian Braga, and Anisor Nedlcu. "Evaluating the Quality Surface Performance of Additive Manufacturing Systems: Methodology and a Material Jetting Case Study". In: *Materials* 12 (Feb. 2019), p. 995. DOI: 10.3390/ma12060995.

[53]   Jose Urcia and Michael Kinzel. "A Study of Numerical Methods of Convective Heat Trans-
       fer on Rough, Additively Manufactured Surfaces". In: *AIAA Scitech 2020 Forum* (2020).
       DOI: 10.2514/6.2020-0548. URL: https://arc.aiaa.org/doi/abs/10.2514/6.
       2020-0548.

[54]   C. Y. Wen and Y. H. Yu. ""Mechanics of fluidization". In: vol. 62. 1966, pp. 100–111.